Inaugural dissertation

for

obtaining the doctoral degree

of the

Combined Faculty of Mathematics, Engineering and Natural Sciences

of the

Ruprecht - Karls - University

Heidelberg

Presented by

MSc. MRes. Paula Argos Vélez

born in: Santander, Spain

Oral examination: 19. 06. 2024

Angiocrine factors in hepatocellular carcinoma: Modelling hepatocarcinogenesis to investigate Wnt signaling

Referees:

PD. Dr. Karin Müller-Decker

Prof. Dr. Hellmut G. Augustin

The presented research was carried out in the department of Vascular Oncology and Metastasis at the German Cancer Research Center (DKFZ), Heidelberg, Germany, between May 2018 and January 2024.

ACKNOWLEDGMENTS

It is not about the destination but the journey. This was certainly not an easy journey but I have been extremely lucky to be accompanied by amazing people who have supported me and helped me to grow along the way.

First, I would like to thank **Prof. Dr. Hellmut Augustin** for giving me the great opportunity to be part of your laboratory. It has been an honor to work in this incredible group, and this period has helped me to grow both professionally and personally.

I would like to express my gratitude to my TAC committee members **PD Dr. Karin Müller-Decker**, **Prof. Dr. Trevor Dale** and **Prof. Dr. Mathias Heikenwälder** for their feedback and lively discussions during our meetings. Furthermore, I would like to thank **PD Dr. Karin Müller-Decker**, **Prof. Dr. Sergio Acebrón** and **Dr. Daniela Duarte Campos** for taking part of my thesis defense committee.

I would like to thank the **SFB-TR209** and the **SFB1324** for financial support, all the scientific meetings and the collaborative research environment. Furthermore, I would like to appreciate **Helmholtz International Graduate School for Cancer Research** for creating a welcoming and supportive environment for international PhD students.

I would also like to express my gratitude to the DKFZ core facilities: **FACS**, **Light Microscopy** and **Small Animal Imaging** Facility in their technical support and their expertise required for this project. I would like to give a special appreciation to the **Central Animal Laboratory Core Facility**.

My sincere gratitude to **Dr. Anja Runge**, **Dr. Ki-Hong Lee**, **Dr. Ashik Abdul Pari** and **Dr. Moritz Jakab** for their feedback and scientific input throughout these years to guide this project. In addition, I would like to thank Dr. Ashik Abdul Pari and Dr. Ki-Hong Lee for their time and contributions correcting this thesis. Thank you all for challenge this project and me, while helping me growing scientifically.

Special mention to (soon to be Dr.) **Guanxiong Wang**. I would like to thank you for your honesty and support throughout these years, and for accompanying me in every “gigantic disaster” I have encountered during this PhD journey. It hasn´t always been a simple journey but your ability to make everything as funny and random as it could get, have made it much easier.

Furthermore, I would like to thank all the **A190 crew**, present and past members: Alina, Anja G., Anja R., Ashik, Barbara, Ben, Benni, Biplab, Bratati, Carleen, Cata, Claudine, Clara, Corinne, Christoph, Denise,

Acknowledgments

Dimi, Divya, Donato, Eva B., Eva G., Guanxiong, Jingjing, Joseph, Katha, Ki, Laura, Leon, Luisa, Mahak, Maria, Melina, Michi, Miki, Moritz, Monika, Nico, Niklas, Petra, Robert, Robin, Sandra, Shubhada, Silvia, Stephanie G., Stephanie P., Till, Xiaowen and Yiwen. Thanks to all of you for your scientific input and for all the lunch and coffee breaks, fun activities and parties. During these six years, I learnt something from each and every one of you. You also made it possible to laugh and overcome the difficult moments.

I would like to express my gratitude to all the friends that I have met in Heidelberg: Alessa, André, Catarina, Cristina, Domi, Jeyan, Karo, Juliane, Joshua, Johannes, Laura, Marta, Sandra, Sonja. Thanks for sharing and understanding the difficult moments, bringing joy into them and getting the most of this experience.

I would like to sincerely thank my "family far away from home". A **Pablo** e **Isa**, no creo que sea capaz de encontrar las palabras adecuadas. Muchas gracias por encontrar siempre la forma de reírnos ante cualquier problema (una aparentemente aburrida tarde de domingo sin ganas de "ir al cole", un inesperado confinamiento, unos Nebenkosten de escándalo,…). Pero sobre todo, quiero agradeceros que siempre he podido contar con vosotros, aun habiendo visto la peor versión de mí. Muchas gracias a **Alberto**, **Alicia**, **Damián**, **Dani**, **Maria**, **Mirian** y **Nuria**. Gracias a todos por crear un grupo tan autentico, donde sentirse aceptado independiente de lo "personaje" que uno sea. Muchas gracias por estar ahí en todo momento: para cada tarde de gym, fiesta, mudanza, visita a comisaria o cualquier cosa que hiciera falta. A todos gracias por cuidar de mí y haber aguantado todas mis locuras y platos rotos (literal y metafóricamente). Me siento muy afortunada de que hayáis formado parte de mi camino y ha sido un honor haber formado parte de los vuestros. MUCHISIMAS GRACIAS!!!

Muchas gracias **Alba**, **Ali**, **Bea**, **Leire**, **Sandra** por vuestro constante apoyo durante estos años, incluso a pesar de la distancia. Gracias por todos los viajes, las videollamas, por escuchar mis podcast… por hacerme sentir que estamos juntas y que ante todo "Podemos Bonitas". A **Bea**, **Cristina**, **Esther**, **Lucía**, **María**, **Nuria**, muchas gracias por creer en mí, incluso cuando yo no lo hacía; y porque a pesar de los años y de ser tan diferentes, seguimos creciendo juntas.

Por último, pero no menos importante, quiero agradecer a mi familia por apoyarme en todo este proceso, aunque eso significara irme lejos. A mi **abuela "Nandi"** por recodarme siempre a mantener la integridad y el trabajo como forma de afrontar cualquier dificultad. A mi **abuela "Toñi"** por enseñarme a buscarle siempre una sonrisa a la vida y que está en la gente que queremos. A **mi abuelo José**, por ser mi gran ejemplo de fortaleza, y por tantísimas otras cosas que has hecho y sigues haciendo por mí; algunas que ni siquiera comprendo y otras que no encuentro palabras siquiera para agradecerte. A mis padres, **Pedro y**

Marisa, muchísimas gracias por todo. No habría llegado hasta aquí, ni siquiera me hubiera acercado, si no llega a ser por vosotros. Todo lo bueno que soy y he conseguido, ha sido, sin duda, gracias a vosotros. A mi hermano **Pedro**, mi pequeño-gran ejemplo a seguir. Muchas gracias por tu eterna paciencia y calma, por creer en mí, a veces más que yo misma. Verte crecer ha sido y es un orgullo y mi motor.

MUCHAS GRACIAS

THANK YOU VERY MUCH

DANKE SCHÖN

TABLE OF CONTENTS

LIST OF FIGURES

List of figures

LIST OF TABLES

ZUSAMMENFASSUNG

Leberkrebs ist die viert häufigste krebsbedingte Todesursache, wobei das Hepatozelluläre Karzinom (HCC) der häufigste Subtyp ist, dessen Inzidenz stetig zunimmt. Er entsteht durch eine chronische Leberschädigung. Im physiologischen Kontext regulieren die Endothelzellen, insbesondere durch ihre angiokrine Wnt-Sekretion, die metabolische Zonierung der Leber. Im pathologischen Kontext tragen Endothelzellen wesentlich zum Fortschreiten der Krankheit bei. Interessanterweise wurde für andere Tumorarten berichtet, dass Wnt-Signale aus der Tumormikroumgebung (TME) sowohl fördernd als auch hemmend auf den Tumor wirken können. Obwohl die Rolle des angiokrinen Wnt-Signalwegs in der Leber im physiologischen Kontext ausgiebig untersucht wurde, ist seine Rolle im pathologischen Kontext des HCC nach wie vor unklar.

Daher habe ich in diesem Projekt die Rolle des angiokrinen Wnt-Signalwegs bei der Entstehung von HCC untersucht. Um diese Frage zu klären, war es von grundlegender Bedeutung, zunächst *in vivo* Modelle zu etablieren, die es ermöglichten, die Hepatokarzinogenese in einer zonenunabhängigen Weise zu rekapitulieren, wobei der TME erhalten bleibt. Zu diesem Zweck entwickelte ich ein fokales Elektroporationsmodell, welches auf der Einführung von genetischem Material in Form von Plasmiden in Zellen der Leber basiert. Das eingeführte Genmaterial kodiert einige der häufigsten mutierten Gene in HCC. Dieses Modell wurde durch ein multifokales (gentechnisch veränderte Maus) GEM-Modell ergänzt, das auf der Expression des SV40 TAg basiert. Darüber hinaus wurden aus beiden *in vivo* Modellen tumorabgeleitete Organoide hergestellt. Aufgrund ihrer wichtigen Rolle in der physiologischen Leberzonierung wurden der Wnt-Enhancer Rspo3 und der Wnt-Ligandensecretion faktor Evi/Wls als Kandidatengene für diese Studie ausgewählt. Beide Gene waren in (Tumor-Endothelzellen) TEC im Vergleich zu gesunden Leber-ECs in den ausgewählten *in vivo* Modellen herunterreguliert. Diese unterschiedliche Expression war im Fall von Rspo3 statistisch signifikant und wurde auch beim Menschen bestätigt. In Übereinstimmung damit führte die endotheliale Deletion von Rspo3 allein oder in Kombination mit Evi/Wls zu einer früheren Tumorbildung. Die Deletion der endothelialen Evi/Wls Sekretion resultierte hingegen in beiden Tumormodellen zu keinen Veränderungen oder zu einer Verzögerung der Tumorentwicklung. Dies deutet darauf hin, dass Rspo3 und in geringerem Maße auch die Evi/Wls-vermittelte Sekretion als Wächter des gesunden Leberendothels fungieren und die Deletion ein pro-tumorale TME schafft. Interessanterweise führte die Deletion von Rspo3 und/oder Evi/Wls auf

autokriner Ebene zu einer Regression und Reifung der Gefäße in HCC. Wenn man sich auf die direkte Interaktion zwischen Tumorzellen und (Tumor-)ECs konzentriert, so induzieren vom Tumor stammende Faktoren die verringerte Expression von Rspo3 und Evi/Wls, wie sie zwischen gesunden und Tumor-ECs festgestellt wurde. Dies deutet auf eine positive Rückkopplungsschleife zwischen dem Tumor und den Tumor-ECs hin, die darauf abzielt, die Expression von Wnt-Signalen in der TME zu verringern, um die Tumorentstehung zu fördern. Insbesondere die *in vitro* Deletion von Rspo3 in Leber-ECs förderte die Proliferation von Tumorzellen. Folglich reduzierte die Zugabe von Rspo3 in das Medium der Hepa1.6 murinen HCC-Zelllinie und der aus dem Tumor stammenden Organoiden die Proliferation der Tumorzellen, was darauf hindeutet, dass Rspo3 ein potenzieller Kandidat für eine antitumorale Wirkung bei HCC ist.

ABSTRACT

Liver cancer is a global health problem. Hepatocellular carcinoma (HCC) is the most common subtype, and its incidence is increasing. It arises from chronic liver damage. Endothelial cells (ECs) regulate liver metabolic zonation in physiological conditions. Endothelial secretion, so called angiocrine effect, in particular Wnt signaling, mediates this phenomenon. ECs also play a major role in liver disease, including cancer. Interestingly, in other tumor entities, Wnt signaling derived from the tumor microenvironment (TME) has been reported to have both, pro- and anti-tumorigenic effects. In the liver, despite being extensively investigated in the physiological context, the role of angiocrine Wnt signaling in HCC remains elusive.

This thesis aimed to study the role of angiocrine Wnt signaling in HCC initiation. To answer this question, it was crucial to first establish *in vivo* models that would accurately recapitulate hepatocarcinogenesis. Therefore, I established a focal electroporation model based on the introduction of plasmids to target hepatocytes. The introduced genetic material encoded some of the most commonly mutated genes found in HCC. This model was complemented by a multifocal (genetically engineered mouse) GEM model based on SV40 TAg expression. In addition, tumor-derived organoids were generated from both *in vivo* models. Thereafter, the Wnt enhancer *Rspo3* and the Wnt secretion factor *Evi/Wls* were the candidate genes selected for this study, based on their role in the physiological liver. Expression of both was decreased in tumor endothelial cells (TEC) in comparison to the healthy liver ECs in both *in vivo* models. This differential expression was statistically significant in the case of *Rspo3*, and also validated in humans. Consistent with this finding, endothelial deletion of *Rspo3*, either alone or in combination with *Evi/Wls*, resulted in earlier tumor formation. Deletion of *Evi/Wls* endothelial secretion induced no changes, or the opposite, in either model. These data indicated that Rspo3, and to a lesser extent, Evi/Wls secretion, acted as gatekeepers of the healthy liver endothelium and deletion of both created a protumorigenic TME. Interestingly, at the autocrine level, deletion of *Rspo3* and/or *Evi/Wls* induced vessel regression and maturation in HCC tumors. Focusing on the direct interactions between tumor cells and (tumor) ECs, tumor-derived factors induced the decreased expression of *Rspo3* and *Evi/Wls* as described in tumor ECs compared to healthy liver ECs. This indicated the existence of a positive feedback loop between tumor and tumor ECs aiming to reduce Wnt signaling expression in the TME to support tumorigenesis. In particular, deletion of *Rspo3 in vitro* from liver ECs enhanced proliferation of tumor cells. Consequently, supplementation of Rspo3 in

the medium of murine HCC cell line and tumor derived organoids reduced tumor cell proliferation. In conclusion, these data suggested Rspo3 as a potential antitumorigenic candidate in HCC.

CONTRIBUTIONS

The overall study was designed and conceptualized under the guidance of my PhD supervisor Prof. Dr. Hellmut G. Augustin. All experiments were designed, performed and analyzed by me. Also, all figures were generated by me.

I received technical assistance for some extensive *in vivo* experiments from Guanxiong Wang and other members of the laboratory. I received technical support in the histological evaluation from Prof. Dr. Carolin Mogler and Dr. Tanka Poth. Furthermore, I received technical support for MRI data acquisition from the small animal imaging facility at the DKFZ.

I received technical assistance from the FACS, light microscopy, small animal imaging facility and the laboratory animal core facilities from DKFZ.

1. INTRODUCTION

1.1. The unique features of the liver

1.1.1. Liver anatomy and physiology

The liver is a distinctive organ involved in multiple biological functions in health and disease. It serves as a reservoir of nutrients and regulates nutrient release into the bloodstream as required. The liver further contributes to maintain the overall homeostasis of the body by: synthesing of bile for digestion, the maintenance of glucose levels in the blood by storing and metabolizing glycogen, the regulation of lipid and cholesterol homeostasis, the metabolism of proteins and xenobiotics (1, 2), iron homeostasis, several endocrine functions (3) and defense against certain pathogens (4).

Hepatocytes, representing 60% of the liver cell count and 80% of the liver mass (5), execute most of the liver functions. The rest of the non-parenchymal cells (NPCs) including liver sinusoidal endothelial cells (LSECs), biliary epithelial cells called cholangiocytes, hepatic stellate cells (HSCs), liver-resident macrophages designated as Kupffer cells and other immune cells (1, 2, 4, 5) further contribute to liver homeostasis.

The functional unit of the liver is the lobule (**Fig. 1**) (1, 2). It is hexagonal in shape, and hepatocytes are organized in concentric circles from the central vein. The portal triad is located at the corners of the lobule. It consists of the hepatic artery, the portal vein and the bile duct. The lobule axis is delineated by the sinusoids, formed by LSECs, and the bile duct, formed by cholangiocytes. HSCs are located in the space of Disse, which is the perisinusoidal space between hepatocytes and LSECs. This space allows free nutrient exchange (1, 6). The remaining non-parenchymal cells are embedded along the porto-central axes (7).

1.1.1.1. Liver vascular system

The liver has a unique blood supply system. It contains a dual and interconnected vascular bed: the hepatic artery provides oxygen rich blood (30%) and nutrient rich blood (70%) is derived from the portal vein. The blood converges in the portal triad and flows towards the central vein, which defines the hepatic blood flow. This blood eventually drains into the hepatic veins (left, middle and right) that lead to the inferior vena cava (**Fig. 1**) (8, 9). Establishing blood flow in the liver is crucial, since the initial blood perfusion and mechanotransduction regulate organ growth and maintenance (10).

The bile canaliculi collect the bile acids secreted by the hepatocytes and direct them into the bile duct to the portal triad, in the opposite direction of the blood flow. Bile acids are transported to the intestine (1).

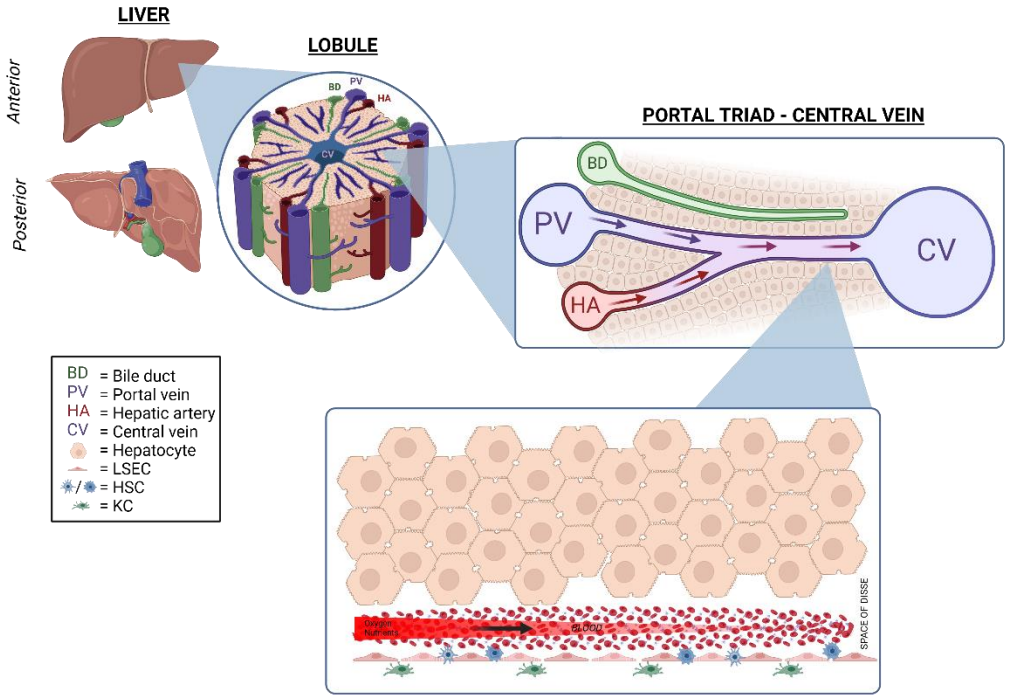

Figure 1. Liver architecture
The liver is a unique organ that regulates metabolic homeostasis of the body. It is organized in functional units designated as lobule. Hepatocytes are the predominant cell type, accompanied by non-parenchymal cells (NPCs). The central vein (CV) is located in the center of the lobule and the portal triad on the corners. The portal triad is formed by the bile duct (BD), portal vein (PV) and hepatic artery (HA). The longitudinal liver axis is delineated by LSECs (forming the sinusoid) cholangiocytes (forming the bile duct). The interface between the hepatocytes and LSECs is termed the space of Disse. This is where hepatic stellate cells (HSCs) are located, while the Kupffer cells (KC) are located within the sinusoids. An oxygen gradient is established due to the hepatic architecture.

1.1.2. The liver organotypic vasculature

1.1.2.1. Organotypicity of endothelial cells

Blood flows from the liver into the vena cava and enters the systemic circulation, eventually reaching the heart. Blood vessels transport blood throughout the body and are considered as the largest interface in animals. They facilitate the transport of oxygen, nutrients, waste products, hormones and particles between different tissues. The inner layer consists of endothelial cells (ECs). Traditionally, ECs have been described to exert a passive functions acting as the building blocks of blood vessels. However, recently, ECs have been identified as a dynamic gatekeeper of the microenvironment, secreting the so-called angiocrine factors. Both active and passive functions of ECs are involved in physiological and pathological

conditions such as development, tissue and metabolic homeostasis, inflammation, regeneration or cancer (6).

Endothelial cells and, hence, the vasculature are functionally and molecularly distinct in different organs, a phenomenon known as organotypic vasculature. Other cell types such as pericytes exert important functions in establishing and maintaining the organotypic vasculature during physiological and pathological conditions (6).

Capillaries are formed by a single layer of ECs, and can be further classified into three main types based on the organotypicity: continuous, fenestrated and sinusoidal. The brain and retina are prototypes of a continuous vasculature, in which ECs are firmly connected by tight junctions. This forms a barrier that selectively allows the diffusion of water and small solutes, but prevents the transport of larger molecules. Fenestrated ECs, which contain intracellular pores and are covered with a diaphragm, are characteristic of endocrine glands, as well as some parts of the intestine, kidneys, and nervous system. They are capable of trafficking small solutes as well as larger molecules such as peptides. The liver, spleen, bone marrow and several endocrine organs exhibit a sinusoidal capillary. These ECs are flattened, separated by gaps, and embedded in a thinner and discontinuous basal lamina allowing the transport of bigger molecules by endocytosis or transcytosis (6).

1.1.2.2. Liver sinusoidal endothelial cells

Liver sinusoidal endothelial cells (LSECs) are a highly specialized endothelial cell type delineating the liver sinusoids. Overall, they account for 15-20% of the total liver cells and 3% of the liver mass (8, 9). Similar to other organotypic sinusoidal ECs, they are discontinuous, and lack a complete basement membrane (**Fig. 2**). Unlike other sinusoidal ECs, LSECs have fenestrations. LSECs fenestrae, ranging 50-150nm in diameter, are organized into clusters named sieve plates (6, 8, 9).

LSECs are involved in several functions that contribute to liver homeostasis (9). For instance, LSECs regulate hepatic blood flow by maintaining the vascular tone, despite fluctuations of pressure due to circadian rhythms and food intake. LSECs express KLF2 and secrete in an autocrine manner NO, CO, thromboxane A2, prostacyclin to regulate shear stress. They are also able to respond to mechanical stretch and trigger HSCs to mediate their vasoconstriction and vasodilation (8, 9). Other liver cell types such as Kupffer cells or smooth muscle cells can further regulate hepatic blood flow (9). In addition, LSECs regulate coagulation and prevent thrombosis locally and systemically, by expressing Factor VIII, ERG, KLF2, TLR-2 or vWF (9, 11).

LSECs form a selective barrier due to their location within the sinusoid, morphology, fenestrae and scavenger functions. They face the space of Disse on the abluminal side, where HSCs and hepatocytes are located. On the other side, they face the interior of the sinusoid, where mixed oxygenated blood flows (9). This creates a bidirectional transport facilitated by their lack of basement membrane, the discontinuity between them and the abundance of fenestrae. In fact, LSECs are the most permeable cells in the mammalian body. Passive diffusion is possible for gases, small and large molecules (e.g. metabolites, plasma proteins, lipoproteins and small chylomicrons, drugs and viruses). These solutes can diffuse into the space of Disse and be metabolized by hepatocytes and HSCs. Larger solutes can also be transported through bidirectional transcytosis between the sinusoid and the space of Disse which is mediated by the high endocytic activity of LSECs. In addition, LSECs have high endocytic potential and vigorous lysosomal activity, allowing them to actively clear the blood of soluble macromolecules, small particles, immune complexes and lipopolysaccharides (8, 9).

LSECs actively regulate both, the innate and the adaptive immune systems. They remove pathogens that may enter via the portal vein to prevent their spread into the systemic circulation. Their scavenger potential allows them to clear antigens and viral particles detected in the blood. Additionally, LSECs can also present antigens that induce the differentiation of certain T cell subtypes. Besides, LSECs enhance liver immune functions including lymphocyte recruitment through low blood pressure and shear stress (4). They may induce cytotoxic T cell arrest within the liver sinusoid triggering hepatocyte death in an antigen-dependent manner (12).

Overall, LSECs are involved in a wide range of functions. The specific repertoire of receptors expressed by LSECs, and their subsequent activation, mediate all of these functions (8).

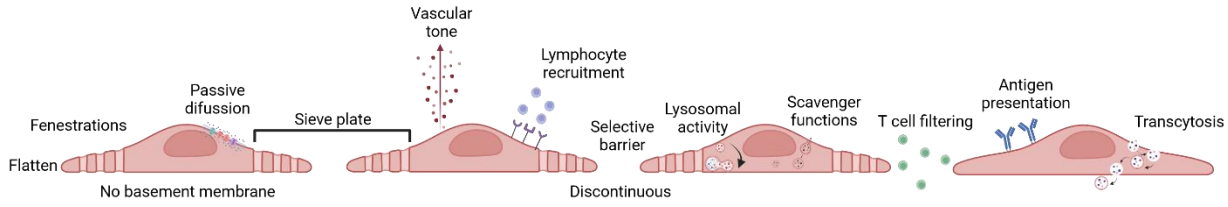

Figure 2. Morphological characteristics of LSECs determine their functions
Liver sinusoidal endothelial cells (LSECs) are a particular type of sinusoidal capillary ECs that reside in the liver. They are discontinuous, lack a complete basement membrane and have fenestrations. LSECs maintain the vascular tone and respond to shear stress by interacting with HSCs. They form a selective barrier allowing the transport of molecules of different sizes due to passive diffusion, their high endocytic activity and transcytosis. LSECs can also act in the immune system due to their scavenger capability and their functions, presenting antigens and filtering T cells.

LSECs undergo molecular and morphological changes during pathological conditions. Transdifferentiation via capillarization is a common occurrence during chronic liver injury, such as liver fibrosis or HCC. LSECs also undergo capillarization and other molecular changes during aging (9). During liver regeneration, LSECs acts as a dynamic rheostat, mediating both hepatocyte and LSEC proliferation (13).

1.1.3. Liver metabolic zonation

The liver has a unique vascular system, with the hepatic artery located at one end of the liver sinusoid, and the central vein at the other. This results in an oxygen gradient. Interestingly, this also induces a gradient of metabolites and other substances present in the liver. Indeed, this gradually changes the molecular signatures and hence specific functions of hepatocytes, LSECs and other NPCs along the sinusoid. This phenomenon has been extensively investigated and is known as liver metabolic zonation (**Fig. 3**). It was first described at the beginning of the 20th century (14) and has recently been further characterized using single-cell sequencing techniques (1, 15-17).

Liver endothelial cells are susceptible to this oxygen gradient. LSECs exhibit a zonation pattern in both the morphological and molecular level. Morphologically, the degree of fenestrations varies between the portal and the central regions. Periportal LSECs show larger but fewer fenestrations in compared to pericentral LSECs (18). Molecularly, the initial characterization of LSEC zonation was challenging due to the relatively small number of cells (8, 9) and low mRNA content. Halpern and colleagues took an intriguing approach and performed partial liver digestion, which leads to doublets of hepatocytes and LSECs. This allows hepatocyte-LSEC paired-cell sequencing, and then, reconstitution of their spatial information based on hepatocyte zonation signatures (19). LSEC zonation is characterized by high Wnt signaling in the pericentral region (19-21). In fact, deletion of Rspo3 completely disrupted this molecular organization, indicating that Rspo3 expression mediates liver metabolic zonation (22). Additionally, LSECs orchestrate the zonation of resident immune cells to sustain optimal host defense. Immune cells are more abundant towards the portal node, where the liver receives the intestinal circulation. The microbiome interacts with the LSECs to establish a chemokine gradient that induces this more efficient immune zonation (23).

However, hepatocytes are the most extensively studied cell type regarding liver zonation due to their high abundance and functionality. It is described that around 50% of hepatocyte genes are zonated (16). Energetically demanding tasks (e.g. protein secretion and gluconeogenesis) show a zonation pattern towards the portal side, where high oxygen concentrations facilitate the high demand for ATP production.

On the other hand, xenobiotic metabolism and glycolysis, which are indepednent of oxygen concentration, are enriched in the pericentral region. Major endocrine liver functions (e.g. iron regulation, insulin growth factors secretion) are presented in the midlobular zone (1). In addition, certain liver tasks are not limited to certain zones but rather compartmentalized hierarchically along the lobule. For instance, enzymes for the neutral bile acid pathway are located sequentially in subsequent lobule layers from the central vein towards the portal side, where the bile acid is secreted (16). The liver can carry out opposing metabolic functions. In these cases, the main enzymes are located in such a way that the waste product from one pathway can be used as a metabolite for the opposite pathway. For example, periportal hepatocytes use glutamine and ammonia to produce glutamate and urea, while pericentral hepatocytes metabolized glutamate back to glutamine. The gradient of different metabolites and substances induces a zonation of the transporters. The transporters vary in affinity and turnover based on the ligand concentration. For instance, the periportal side, which has high ligand concentrations, is enriched in low affinity and high turnover transporters. On the contrary, the pericentral zone, which has relatively low ligand concentrations, shows receptors with high affinity and low turnover (1).

The unique capacity of the liver for self-renewal was also investigated in terms of hepatocyte zonation. A diploid population, expressing liver progenitor markers and located near the central vein, was initially described to control hepatocyte homeostatic renewal (24). However, two recent back-to-back papers have shown that the midlobular zone mediates hepatocyte repopulation in liver homeostasis and repair after injury (25, 26). It was also described that hepatocyte repopulation was carried by midlobular and periportal hepatocytes. How NPCs contribute to liver regeneration was also further studied using single cell RNA sequencing techniques. However, this investigation was performed in a liver regeneration model following APAP intoxication that damages specifically pericentral hepatocytes (27).

Liver metabolic zonation has been described for other NPCs. HSC zonation has been uncovered using single-cell RNA sequencing. HSCs were classified into two subpopulations: portal vein-associated HSCs (PaHSCs) and central vein-associated HSCs (CaHSCs), which differ in their location and function. CaHSCs were found to be the main source of collagen during fibrosis, when HSCs become activated. (28). The changes that HSCs undergo during fibrosis were characterized at the transcriptomic level. Transdifferentiation of HSC or portal fibroblast into myofibroblast depends on the etiology. In general, HSCs are more prone to adapt to fibrosis, but in the case of early cholestasis portal fibroblasts would be the ones undergoing transdifferentiation. (29).

Liver metabolic zonation has been mostly studied in rodents. There are limited reports in humans due to the restricted access to healthy human tissues and the high variability between samples, even in physiological conditions (e.g., genetics, sex, adiposity, metabolic states) (1). The available evidence indicates both similarities and differences between mice and humans (30).

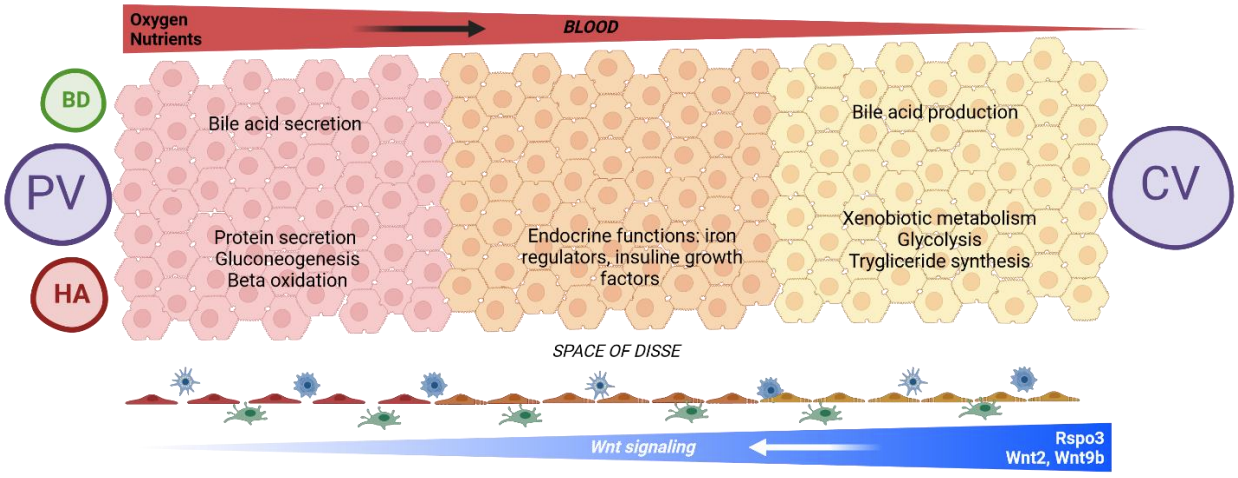

Figure 3. Liver metabolic zonation
Liver metabolic zonation is originated by the presence of the hepatic artery (HA), on the portal triad, and the central vein (CV) in the opposite side leading to a gradient of oxygen. This creates, subsequently, a gradient and compartmentalization of metabolites and functions along the liver axis. Liver zonation is described for almost all liver cell types. LSECs vary morphologically (i.e. number and extent of fenestrations) and also functionally. High levels of Wnt expression are expressed in central LSECs. Actually, Rspo3 secretion from the CV maintains hepatocyte liver zonation. Hepatocytes located in the periportal area are specialized in protein secretion, gluconeogenesis and beta oxidation, where the oxygen concentration is high. On the contrary, central hepatocytes perform functions related to xenobiotic metabolism, glycolysis and triglyceride synthesis. The midlobular zone plays a crucial endocrine role. Certain functions are compartmentalized, such as bile acid production occur towards the central vein which is eventually secreted in the bile duct (BD) at the portal side. This creates a gradient of metabolites that induce a zonation patter in the transporters.

The liver metabolic zonation is altered during pathological conditions. This alterations occur preferentially in certain regions within the central-portal axis, depending on the pathology. For instance, certain drugs and compounds are metabolized around the central region where the cytochrome is expressed. In this way, APAP or ethanol induce damage preferentially in this region. Similarly, fatty liver disease is predominantly located around the central area. On the contrary, the preferential metabolization of other xenobiotics and compounds such as doxorubicin, can lead to cellular damage around the portal area. This

is the case of autoimmune hepatitis or primary biliary cirrhosis. However, it is still unknown whether and which zonation is initially altered in the case of liver cancer and HCC (1).

1.2. Hepatocellular carcinoma

1.2.1. Hallmarks of hepatocellular carcinoma

Liver cancer is a major health issue worldwide, ranking as the sixth most common type of cancer. Its incidence has been increasing over the last decades, and current estimations suggest this trend will continue (31-33). Primary liver cancer (PLV) has several subtypes including hepatocellular carcinoma (HCC), intrahepatic cholangiocarcinoma (ICC), hepatoblastoma and combined HCC and ICC (34). Hepatocellular carcinoma (HCC) is the most common subtype of liver cancer, accounting for almost 90% of all cases. It is caused by chronic liver damage (31-33).

The major risk factors for HCC are virus infections such as Hepatitis B and C virus (HBV and HCV), excessive alcohol consumption, and non-alcoholic steatohepatitis (NASH) or non-alcoholic fatty liver diseases (NAFLD) associated with diabetes or obesity. Other less common risk factors include primary biliary cholangitis, hemochromatosis and α1- antitrypsin deficiency (31, 32). These risk factors have different distributions based on age, gender and geography. For instance, HBV is more common in Asia and Africa, while HCV is more prevalent in North America, Europe and Japan. Excessive alcohol consumption accounts for up to one third of all cases of HCC; with Europe, East Asia and South America being the most affected regions. The risk increases when coexisting with other etiologies. NASH incidence, along with obesity, is increasing, particularly in Western countries (31, 32).

Aging is a major risk factor, like in other cancers. Its incidence increases drastically after the age of 70. Additionally, it is more prevalent in men due to the involvement of sex hormones in tumorigenesis and a biased distribution of the risk factors described above (31, 32).

1.2.1.1. Pathophysiology

Continuous exposure to one or several of these risk factors can lead to chronic liver inflammation, and, subsequently, cirrhosis. These risk factors induce cirrhosis by different mechanisms. HBV is a DNA virus that integrates into the genome and induces mutagenesis. In contrast, HCV is a RNA virus, hence, it does not incorporate into the genome, and only becomes oncogenic when coexisting with preexisting cirrhosis or chronic liver disease bridging fibrosis. Excessive alcohol consumption can induce the formation of a

pre-cirrhotic state designated as alcoholic liver disease (31, 32). NAFLD is a spectrum of liver diseases, characterized by metabolic syndrome, ranging from simple steatosis to NASH. Tumor transformation can eventually be induced by multiple genetic and environmental factors that create a microenvironment that predominates an impaired immune system and enhanced inflammatory response, DNA damage, oxidative stress and autophagy (35).

Environmental factors can interact synergistically or with genetic alterations, to create a damaged environment that mediates the transition from cirrhosis to HCC, and enhances tumor progression. This process is complex and multistep (31, 32). For instance, autophagy mediates the transition from fibrosis to cirrhosis via ductular reaction through YAP/TAZ signaling (36). Wnt signaling has also been implicated in multiple steps. Overexpression of β-catenin leads to tumors harboring GS activation, and sustained mTORC1 activation (37). β-catenin activation was also reported to enhance cancer stem cell (CSC) characteristics through PTK2 activation (38).

In the cirrhotic state, some pre-tumorigenic lesions can be designated as low-grade dysplastic nodules (LGDNs). These nodules can progress to high-grade dysplastic nodules (HGDNs), which can eventually develop into HCC. It has also been described that HCC can originate from adenoma rather than cirrhosis. In such case, tumor transformation occurs through the sequential accumulation of mutations (32). The progression from early to more advanced stages involves the accumulation of more alterations. Later, tumor transformation leads to invasion and, eventually, metastasis (31, 32). The more common sites of HCC metastasis, in descending order of probability, are the lungs, regional lymph nodes, bones, adrenal glands, brain, and peritoneum/omentum (39).

Although hepatocarcinogenesis is a relatively well understood process, the cell of origin is still controversial. It is considered to be similar to other solid tumors, either liver progenitor cells or hepatocytes that undergo transformation due to this chronic damage (31, 32). This damage arises and evolves in different ways depending on their etiology. For instance, during NASH, lipid accumulation in hepatocytes induces inflammation leading to HCC (40). Also, glycogen accumulation could lead to hepatocarcinogenesis (41).

Another well-established explanation for the initiation of tumorigenesis is the existence of a particular population of tumor cells called cancer stem cells (CSC). This population possesses stem cell features and a hierarchical organization that induces tumor transformation. CSCs can not only control tumor growth, but also mediate tumor dormancy, recurrence and resistance to therapy. Liver CSCs are characterized by

the expression of: CD13, CD24, CD44, CD47, CD90, CD133, ICAM1, EpCAM, LGR5, OV6, $\alpha 2\delta 1$, aldehyde dehydrogenases, CK19. CSCs are located in a specific niche, allowing interactions with the TME. These interactions include stromal cells (e.g. adipocytes, CAFs, ECs), hepatitis viruses, the ECM and a reduced nutrient supply. The aim is to maintain the tumorigenic properties of CSCs. Additionally, CSCs and the immune system engage in a reciprocal interaction, where CSCs induce immune evasion and the immune system sustains CSCs´ stemness capabilities (42).

Hepatocarcinogenesis is a complex process involving numerous mutations. Therefore, Llovet et al. (31) classified HCC into two subgroups based on the main drivers triggering tumorigenesis, the etiologies of origin, the immune status, genomic alterations, histological features and clinical outcomes. The subgroups are designated as proliferation and non-proliferation, each accounting for approximately half of the cases. The proliferation subclass is characterized by mutations in TP53 and FGF19 or CCND1. It is associated with HBV etiology and has a worse prognosis. It can be subdivided into two subtypes: the progenitor cell marker (25-30%) and the Wnt-TGFβ (20%). The non-proliferation subtype which originates from alcohol and HCV chronic livers, and is associated with better prognosis. It is characterized by *CTNNB1* and IFNα mutations. It is worth mentioning that certain mutations, such as TERT mutations, are shared. **Table 1** summarizes both the proliferation and non-proliferation classes, including other factors such as genetic features, pathological subclass, immunological status, vascular invasion, and serum AFP levels.

Table 1. Classification of HCC main subtypes.

	Proliferation class		Non-proliferation class	
Molecular subclass	Progenitor cell marker	Wnt-TGFβ	IFNα	*CTNNB1*
Main etiology	HBV		Alcohol, HCV, NASH	
Pathological subclass	Progenitor, mixed FLC/HCC	Macrotrabecular massive	Steatohepatic HCC	Cholestatic HCC
Cell differentiation	Poor		Well to moderate (hepatocyte-like)	
Genetic features	Chromosomal instability		Chromosomal stability	
Main signaling pathways	*TP53, FGF19/CCND1* mTOR, RAS-MAPK		IL6-JAK-STAT	*CTNNB1* (Wnt-β-catenin)
IHC marker	p-RPS6+		CRP+	GS+/ nuclear β- catenin
Immunological features	Immune-active	Immune-exhausted	Immune-active	Immune-excluded
Vascular invasion	High frequency		Low frequency	
Serum AFP	High		Low	
Prognosis	More aggressive		Less aggressive	

Information was extracted from (31) and summarized to highlight the main features of interest for this project.

1.2.1.2. Angiogenesis

Angiogenesis is considered one of the hallmarks of HCC. It is defined as the formation of new blood vessels from the expansion and remodeling of preexisting ones. This process occurs in both physiological and pathological conditions, including the development and various cancers.

EC proliferation and migration, as well as anastomosis and lumen formation, induce the development of new sprouts during angiogenesis. The recruitment of smooth muscle and pericytes, the strengthening of cell-cell junctions and vessel regression are required for the vessel maturation. The sprouts contain two types of cells: tip cells (i.e. migratory cells that initiate the extension of the sprout and formation of vascular connections) and stalk cells (i.e. proliferative cells during sprout elongation and involved in lumen formation) (43).

The newly formed vessels during tumor angiogenesis are structurally and functionally abnormal. Morphologically, they are irregular (i.e. ranging from wide and tortuous to thin and compressed), poorly interconnected or multilayered, and have odd vascular branching. Additionally, the basement membrane is altered in terms of thickness and composition. The new vessel network is dysfunctional and

incompletely covered by pericytes, making it leaky and facilitating tumor cell intravasation. Additionally, it is aberrant and inefficient, hindering functional drug delivery and leading to a hypoxic environment. This microenvironment induces an angiogenic switch due to an imbalance between anti- and pro-angiogenic signals, which further sustains angiogenesis (44, 45).

The new vessels structure also has the potential to secrete angiocrine factors, which affect tumor progression. The secretome includes cytokines that recruit inflammatory cells and endothelial progenitor cells (EPCs). This, along with ECM deposition, creates a vascular niche that supports the expansion of tumor cells and their progenitors (46).

It was hypothesized that angiogenesis could be used as targeted therapy due to the high relevance of the tumor vasculature for tumor progression. The aim of this therapy was to block the formation of new vessels in the tumor, which would induce tumor starvation of oxygen and nutrients, eventually leading to the eradication of the tumor. However, the therapies developed work by inducing tumor vessel normalization (7). Current anti-angiogenic therapies aim to induce vascular normalization, with tight junctions leading to less tissue edema, enhanced perfusion and reduced hypoxia. This promotes a less pro-tumorigenic environment with enhanced drug delivery (47). However, anti-angiogenic therapies have not been very successful in the case of HCC. Sorafenib is the only effective treatment that was proven, for decades, to have a partial anti-angiogenic potential. This is a multikinase inhibitor, with VEGF as one of its multiple targets (48).

1.2.1.3. Treatments

Several treatment options are available, although their effectiveness is limited. The treatment of choice depends on the tumor stage determined by the BCLC (Barcelona Clinic Liver Cancer) staging system. Treatments can be classified into surgical intervention, and locoregional and systemic therapies (32).

Surgical interventions

Surgical interventions, such as resection and liver transplantation, are the first line of treatment for early stage patients. These interventions have almost 80% effectiveness in 5-year survival. The decision among them is based on general liver function and tumor characteristics, following the standard transplantation guidelines for any other solid organ. Resection is the preferred option for patients without cirrhosis, or a single tumor and good liver function. It may result in intrahepatic micrometastasis or de novo tumor formation in up to 70% of cases at a 5-year survival rate. In contrast, liver transplantation is the preferred

treatment for patients with cirrhosis and a certain degree of tumor burden, resulting in better long-term survival (31).

Locoregional therapies

There are three types of locoregional therapies: ablation, radiotherapy and transarterial therapies such as TACE. Ablation is a chemical, thermal or electrical injury directly into the tumor, making it an alternative to surgical interventions. There are several methods: radiofrequency ablation (RFA), microwave ablation (MWA) or cryoablation (CRA). Radiotherapy (i.e. external beam, photons or protons) is used to treat patients with different tumor burden and to treat extrahepatic metastasis. Transarterial therapies, particularly TACE, are the recommended line of treatment for intermediate-stage patients. It mechanically restricts blood supply into the tumor while delivering chemotherapy locally (31, 32).

Systemic therapies

Systemic therapies are the preferred treatment option for advanced disease or in the event of progression after surgery or locoregional therapies. This group accounts for 50-60% of patients (49, 50). Sorafenib, a multikinase inhibitor targeting Raf-1, B-Raf, Ras/Raf/MEK/ERK, c-Kit, FLT-3, VEGFR-2/3, PDGFR-β has been the first line of treatment for the past decade. Mechanistically, it reduces tumor cell proliferation and angiogenesis, resulting in an increased median survival of up to 5 months. However, Sorafenib may lead to side effects, including drug resistance (48). Therefore, it was necessary to establish more effective and precise treatments. Drugs analogous to Sorafenib with a comparable mechanism of action have been developed, including: Lenvatinib (anti-FGFR1-4, VEGFR, PDGFR, c-Kit, RET), Regorafenib (anti-VEGFR, PDGFR, B-raf, Tie2), Cabozantinib (anti-MET, VEGFR, RET), Ramucirumab (anti-VEGFR2) (49, 50). Of particular interest is Donafenib, which has an improved pharmacokinetic profile and is the only one that has proven to be more effective than Sorafenib as a first-line monotherapy (51).

Recently, in 2020, the IMbrave150 trial demonstrated that the combination of Atezolizumab (anti- PD-L1) and Bevacizumab (anti-VEGFA) resulted in better overall and progression free survival compared to the standard care of treatment (52, 53). The exact mechanism of action is currently being investigated to enable patient stratification. It has been described that preexisting tumor immunity is associated with better survival. The combination synergizes to target angiogenesis, T-reg proliferation, and myeloid cell inflammation (54). This is the first time that an anti-angiogenic treatment has been proven effective in treating HCC. Furthermore, this combination has recently been demonstrated effective in preventing recurrence after resection or ablation (55).

IMBrave has also uncovered immunotherapies for HCC systemic treatments. Pembrolizumab (anti PD-1) has been tested and found effective alone and in combination with Lenvatinib (56, 57). Similarly, Cabozantinib plus Nivolumab (anti-PD-1) was shown to enhance anti-tumor immunity and facilitate resection in advance HCC (58). Other combinations of ICIs, such as Nivolumab plus Ipilimumab (anti-CTLA4) have been investigated. This is the first immunotherapy combination approved after first-line treatment failure. ICIs combinations aim to induce an activated immune TME. The effectiveness of the immunotherapies, whether single, dual or combined with other systemic therapies, is reported to be related to virus etiology, particularly HBV (49, 51).

Similarly, other combinations are under investigation such as Lenvatinib plus EGFR inhibitor. In this case, Lenvatinib induces feedback activation of EGFR, which is subsequently blocked by its inhibitor, resulting in a significant clinical response for patients with high levels of EGFR (59).

Currently, the treatments available for HCC are somewhat limited, hence, there is still much room for improving the therapeutic landscape. The focus is on immunotherapies, sequential and alternating treatments, synthetic lethality, adoptive cell therapy and vaccination (51).

1.2.2. Preclinical models of hepatocellular carcinoma

1.2.2.1. In vitro models

Cell lines

Cell lines are commonly used in research, allowing extensive experimentation for mechanistic studies or high-throughput screening due to their homogeneity and the fact they can propagate almost unlimitedly (60). Hepa1.6 is one of the few murine HCC cell lines available and derives from a spontaneous hepatoma in a C57/L mouse (61). However, it is important to note that cell lines are typically generated from very aggressive and/or metastatic tumors, resulting in an underrepresentation of primary tumor that are less aggressive. In addition, tumor heterogeneity is lost when cells are adapted to *in vitro* conditions, resulting in a monoclonal population (60). Furthermore, the cell lines have has even the potential to transdifferentiate. A study described that liver cancer cell lines had the least correlation to matched tumor samples compared to other cell lines studied (62).

Organoids

Organoids were defined as 3D structures in which cells spontaneously self-organize into structures that resemble the *in vivo* tissue in terms of cellular composition and tissue function. They are derived from

either pluripotent stem cells (PSCs), neonatal tissue stem cells or adult-derived stem/progenitor cells (AdSCs) (63). The culture media required is very complex and well-defined. Organoids contain several cell types and have the capacity to differentiate *in vitro* by removing certain factors from the media (60, 64), unlike homogenous cell lines. The first complex 3D self-organized cell organization was a crypt villus like structure formed *in vitro* from single Lgr5+ intestinal stem cells (65). Organoids have been established from multiple organs, either from adult stem cells and tissues or from pluripotent stem cells. These include: colon and rectum, small intestine, liver, pancreas, lung, stomach, esophagus, kidney, brain, mammary gland, prostate, pituitary gland, fallopian tube, salivary gland, taste buds, inner ear and retina (66) and even from blood vessels (67). Liver organoids were initially established from the liver after injury by enhancing the Wnt-driven regeneration (68). They can now be isolated from duct cells (69) or hepatocytes (70).

Organoids have become state-of-the-art due to their great potential (71). Tumor biopsies can be biobanked as organoids to be used for drug screening in CRC (72) or in other gastrointestinal cancers (73), including the liver (74). Tumor organoids have been established from patient tumor needle biopsies. These organoids retain the morphology, genetic heterogeneity and markers expression of the original tumor, which makes them a valuable tool for personalized medicine (75). They can predict therapy responses in tumors derived from both mice (76) and humans (77). Additionally, healthy liver organoids can be used as tumor models by introducing tumor mutations to recapitulate HCC tumorigenesis *in vitro* (69). Liver organoids have been used as a tool to study how cell to cell contact between ductal and mesenchymal cells mediates epithelial cell proliferation based on the different cell to cell ratio (78).

Although organoids are more complex than cell lines, they still lack the intricate interactions provided by the TME (74), which hinders the retention of some of the hallmarks of HCC (79). To address this, co-culture systems have been established, such as intraepithelial lymphocytes (IELs) with intestinal epithelial organoids (80) or NSCLC and CRC organoids with peripheral blood lymphocytes (81). Furthermore, vascularized and functional human organoids (82) have been established from liver iPSCs, MSCs and HUVECs (83). Additionally, PDOs maintained in an air-liquid interface (AIL) have been shown to retain immune cells (84). However, it is important to note that this is still a reductionist and simplified system.

1.2.2.2. In vivo murine models

In vitro models have certain limitations, therefore, they need to be complemented with *in vivo* models. The mouse is a widely use animal model in research due to their high resemblance genetically and

molecularly with humans. Additionally, mice are relatively easy to handle, have a high breeding capacity and a short lifespan (85, 86). The most commonly used murine models in HCC are the following:

Induced models

Induced models aim to recapitulate the liver damage that predisposes to hepatocarcinogenesis. There are several types of induced models depending on the carcinogenic agent: chemical-, diet- or virus-induced. Chemically induced models can be classified as genotoxic and non-genotoxic, based on whether they directly cause DNA damage. Diethylnitrosamine (DEN), 2-acetylaminofluorene (2-AAF) and aflatoxin are the genotoxic agents utilized in HCC. On the contrary, carbon tetrachloride (CCl_4), thioacetamide (TAA) and phenobarbital (PB) are the non-genotoxic compounds used. Overall, DEN and CCl_4 are the most commonly used chemicals. A single i.p injection of DEN, based on the body weight, induces DNA alkylation and creates an inflamed environment that leads to tumorigenesis in 7 to 11 months. In contrast, several injections of the CCl_4 are required to induce hepatocyte necrosis and activate Kupffer cells. This leads to fibrosis, cirrhosis and HCC, in 4-6 weeks. Combinations of both, as well as others, such as TAA or PB, are frequently used to more faithfully mimic hepatocarcinogenesis. These models are effective in recapitulating HCC formation and its TME, although they are very time consuming and it is difficult to identify the genetic background of the tumor (85-87).

Several models have been established to recapitulate the metabolic syndrome that induces tumorigenesis due to the increase of HCC incidence caused by NAFLD. These models are diets that vary in the abundance and presence of certain elements such as fat, fructose and other compounds. The most commonly used diets are: high-fat diet (HFD), high-fat high-cholesterol diet (HFHCD), high-fat high-fructose diet (HFHFD), Western diet (WD), choline-deficient high-fat diet (CDHFD), methionine and choline-deficient diet (MCD) and choline-deficient l-amino acid-defined diet (CDAAD). These diets are administered *ad libitum*, but the time for tumorigenesis and the incidence is suboptimal. Therefore, they are often combined with other hepatotoxins, such as DEN or STZ (streptozotocin). There are also models in which alcohol is combined with other carcinogens to mimic hepatocarcinogenesis resulting from excessive alcohol consumption (85-87).

Developing virus-induced models is challenging due to the high tropism of HBV and HCV. The models available are GEM models that mimic the hepatitis induced by either virus (85-87).

Genetically engineered

The most commonly used genetic method is hydrodynamic tail vein injection (HTVI). It consists on injecting a large volume of solution (10% of mouse body weight) containing the plasmids expressing the genes of interest into the lateral tail vein. The high hydrodynamic pressure created by the injection of this large volume in a short period of time enhances capillarization in the liver endothelium, facilitating the incorporation of the plasmids into hepatocytes. This technique uses various systems to express the transgenes including the SB (sleeping beauty) transpose for genome integration, the Cre-loxP or the CRISPR-Cas9 system. These systems target some of the most commonly mutated genes including, YAP/TAZ, c-Myc, Met, β-catenin, AKT, NRas, HRas, p53, RBMY or pTen. The same genes can also be targeted in GEM (genetically engineering mouse) using the same systems Cre-lox-P and SB systems for deletion and overexpression of target genes, respectively. GEMs allow to investigate the effect of specific gene mutation or combinations. For instance, the time for tumorigenesis depends on the combination of tumor suppressor genes and oncogenes and the TME. However, these models have the disadvantage of requiring extensive time to create a stable mouse line with the correct genotype for subsequent generations (85-87).

The iAST model deserves special attention since it is one of the actual transgenic mouse lines available to induce hepatocarcinogenesis via transient viral hepatitis. These mice express the SV40 large T-antigen flanked by a loxP stop cassette under the albumin promoter in BL6. Upon injection of adenoviral Cre recombinase via the tail vein, the stop cassette is excised, leading to the expression of the oncogene, and eventually resulting in multinodular tumors within 5 to 8 weeks (**Fig. 4**). Besides, this model recapitulates histological and angiogenic features of human HCC including its response to Sorafenib (88).

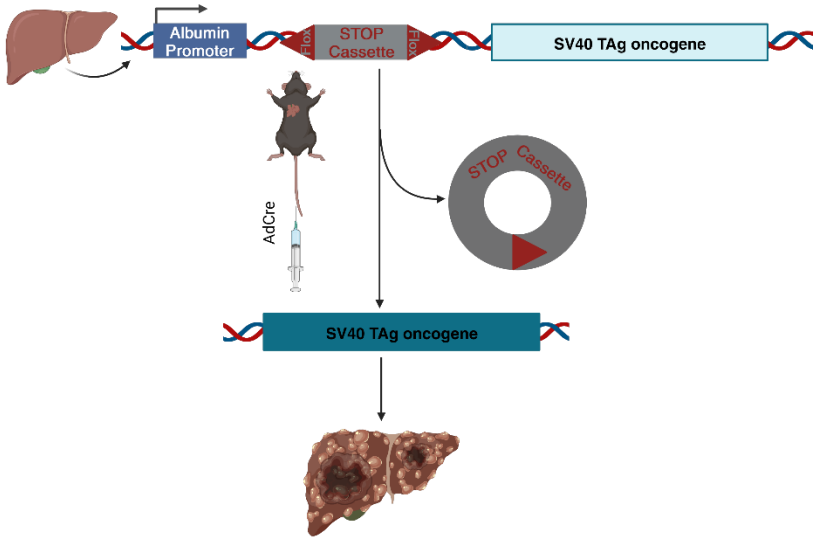

Figure 4. iAST mouse model
The GEM iAST expresses the SV40 large T antigen under the albumin promoter and a loxP-flanked stop cassette. Upon intravenous injection of AdCre, the flox-Stop cassette is deleted, resulting in the expression of the SV40 large T antigen and a transient viral hepatitis. Multinodular tumors formed within 5 to 8 weeks.

Engrafted models

In engrafted or transplantation models mouse (allograft) or human (xenograft) cell lines, tumor organoids or fragments of tumors are implanted into a recipient mouse either subcutaneously or orthotopically. The latter can be implanted via intrahepatic, intrasplenic or intraportal injection and has the potential to fully recapitulate the TME. Xenograft models have the advantage that they resemble the histological, molecular and genetic characteristics of human tumors, making them clinically relevant models. However, they are slow and complex models. In addition, the mice used as hosts are immunocompromised or immunodeficient (85-87), which means that the tumor-host interactions are not fully recapitulated due to the absence of the immune system (60). This is a significant drawback since the role of the immune system is not considered. This is particularly important given the recent research demonstrating the importance of the immune system in the progression and as a therapeutic potential (52). To overcome this limitation, humanized mouse models were generated by transplanting CD34+ hematopoietic stem cells and human peripheral blood mononuclear cells into sublethally irradiated mice (85).

The type of transplanted material is another point. When using a cell line, it is relatively straightforward. However, it is important to note that the limitations of the cell lines itself also applies such as the overrepresentation of aggressive populations due to their high engraftment yield. In addition, it is possible that only one or a few subclonal populations contribute significantly to the overall tumor volume, which

hinders the replication of tumor heterogeneity (60). Conversely, the transplantation of patient-derived material in patient-derived xenografts (PDXs) may result in low engraftment efficiency and prolonged tumorigenesis (85).

Preclinical models available for HCC are limited in terms of time and efficiency to recapitulate HCC initiation and progression (**Fig. 5**). This impedes a successful and more efficient drug discovery process. Additionally, some of the most commonly mutated genes in HCC, such as TP53, TERT, or CTNNB1, are not directly druggable (51). Although small molecules targeting the Wnt/β-catenin pathway have been investigated, nothing on this line has been translated into the clinics (89). Therefore, it is still necessary to understand the role of Wnt signaling in the initiation and progression of HCC.

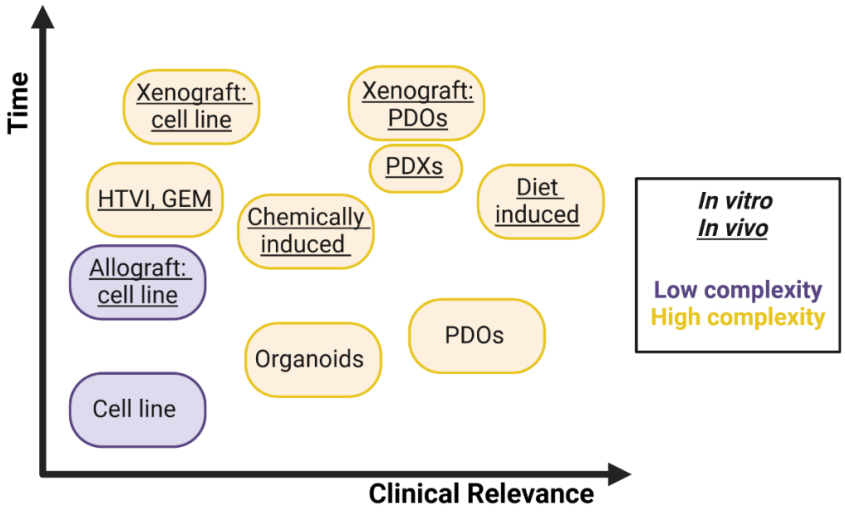

Figure 5. HCC models- *in vitro* and *in vivo* - classified based on the time for tumorigenesis, clinical relevance and complexity
Representation of the most commonly used HCC models *in vitro* and *in vivo*. They are classified based on the time required for tumor formation, their clinical relevance, and their complexity. Time and clinical relevance are described on the 2-axis graph. Complexity is represented by color code, with purple and yellow indicating low and high complexity. *In vivo* models are underlined.

1.3. Wnt signaling

1.3.1. Wnt signaling pathway

The Wnt signaling pathway is highly conserved evolutionary. It plays a crucial role in several functions in physiological and pathological conditions, including embryonic axis formation, organogenesis, tissue architecture maintenance, stem cell proliferation and cancer (90, 91).

The Wnt family comprises multiple Wnt secretory proteins that can bind to over 15 different receptors and co-receptors, resulting in the activation of different downstream pathways. Wnts are cysteine

enriched proteins, have a size of 40 KDa and undergo several posttranslational modifications (91). They interact with various receptors including Frizzled (1-10), low density lipoprotein receptor-related protein 5-6 (LRP5-6), receptor Tyr kinase-like orphan receptor (ROR), protein Tyr kinase 7 (PTK7), receptor Tyr kinase (RYK), muscle skeletal receptor Tyr kinase (MUSK), and syndecan and glypican (both belong to the proteoglycan family) (90). The activation depends on the specific combination of ligand-receptor and the cellular context (90, 91).

1.3.1.1. Canonical and non-canonical pathways

Traditionally, Wnt signaling was described as β-catenin, dependent and independent, also known as canonical and non-canonical, respectively (**Fig. 6**). However, recently, different sub-branches have been described based on the cellular context (90, 91). Canonical signaling is inactive by default, and the binding of the ligands activates it. In the inactive state, β-catenin is phosphorylated and hijacked in the "destruction complex". The proteins involved in this process are: proteasome, Disheveled (Dvl), adenomatosis polyposis coli (APC), Axin, the constitutively active kinases CKIα (casein kinase Iα) and GSK3 (glycogen synthase kinase 3), and the E3-ubiquitin ligase, β-TrCP. β-catenin is sequentially phosphorylated by CK1 and GSK3, when not activated, leading to its ubiquitination and degradation by the proteasome in the "destruction complex". Upon ligand binding, the receptor dimerizes and transitions into the activated state. The destruction complex is then recruited into the Wnt-receptor multiplex via Axin, which acts as a scaffold protein, and is inactivated. Upon inactivation, the destruction complex is degraded, leading to β-catenin stabilization and accumulation in the cytoplasm. Subsequently, β-catenin is translocated into the nucleus. In parallel, some co-receptors may sustain pathway activation, such as, LRP which can directly inhibit GSK3. Once in the nucleus, β-catenin interacts with transcription factors such as T cell factor (TCF) and lymphoid enhancer-binding factor (LEF), regulating the transcription of different target genes. In its inactivated state, TCF is also retained by its interactions with the repressor Groucho (90, 91).

The non-canonical signaling pathway is classified into two sub-branches: planar cell polarity (PCP) and Wnt-Ca^{2+}. The PCP is initiated by the activation of the Frizzled receptor, which then stimulates the small GTPases RHOA and RAC1, via Dvl. This induces activation of RHO kinase (ROCK) and JUN-N-terminal kinase (JNK), respectively, resulting in actin polymerization and JUN transcription factor activation. The PCP pathway regulates cell polarity, cell motility and morphogenetic movements. The Wnt-Ca^{2+} is specifically activated by Wnts acting on heterotrimeric G proteins. This leads to the activation of phospholipase C (PLC), which metabolites phosphatidylinositol-4,5-bisphosphate (PIP2) into diacylglycerol (DAG) and

inositol-1,4,5-trisphosphate (InsP3). Both DAG and InsP3 trigger the release of Ca^{2+} into the cytoplasm, which in turn activates calmodulin-dependent kinase II (CAMKII), protein kinase C (PKC) and calcineurin. Each of these proteins leads to the activation of different branches of the pathway. Calcineurin stimulates nuclear factor of activated T (NFAT), which translocates into the nucleus to regulate cell fate and migration. PKC activates cell division cycle 42 (CDC42), leading to actin polymerization. Both PKC and CAMKII induction block β-catenin nuclear activation. Similarly, PCP signaling antagonizes canonical Wnt signaling (90).

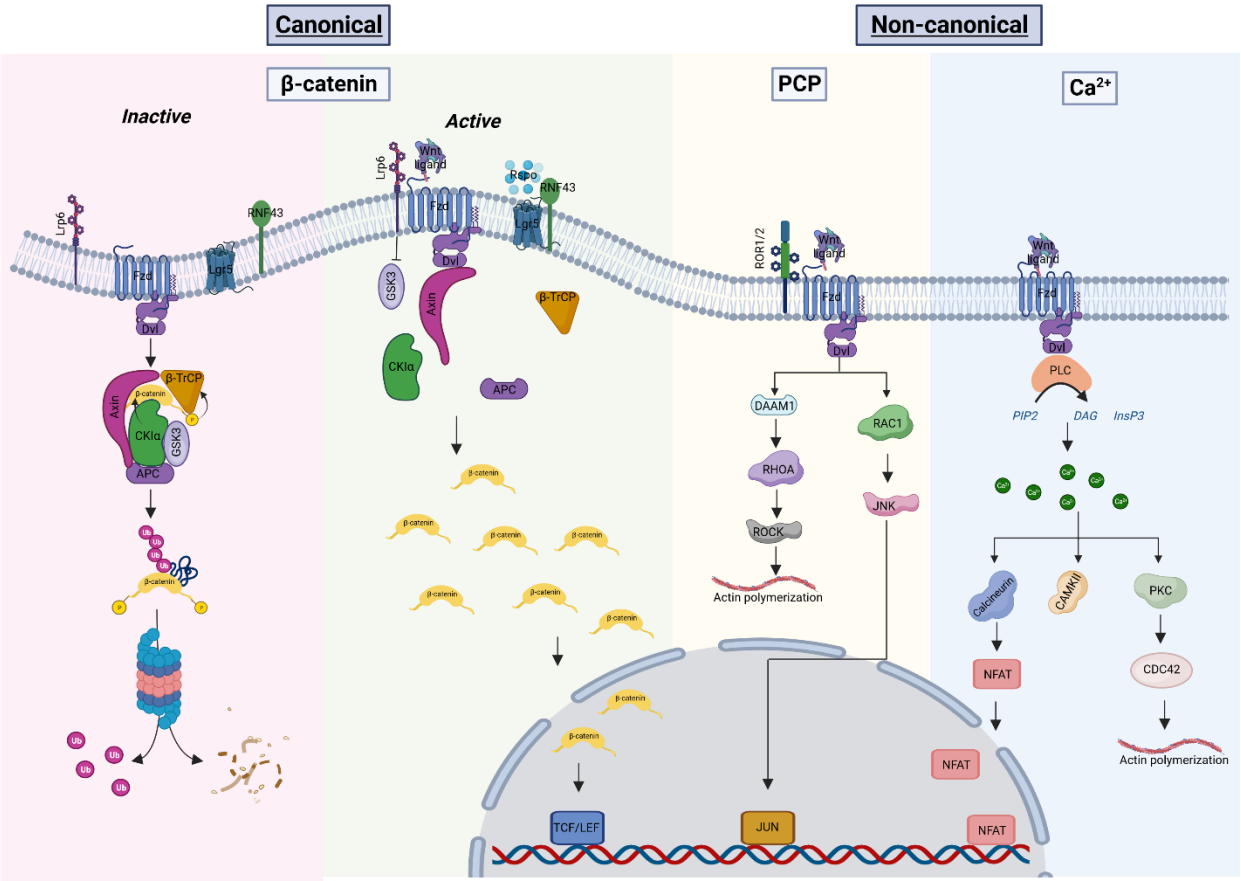

Figure 6. Wnt signaling pathway
The Wnt pathway is a highly conserved signaling pathway that is divided into two branches: canonical (β-catenin dependent) and non-canonical (β-catenin independent). In the canonical pathway, β-catenin exists in an inactive and active state. It is phosphorylated, in the inactive state, and hijacked in the destruction complex, later ubiquitinized, and destroyed by the proteasome. Upon ligand binding, the pathway is activated, leading to the dephosphorization of the β-catenin. This results in its release from the destruction complex and subsequent translocation into the nucleus, where it binds to several transcription factors. The non-canonical pathway can be divided into two sub-branches: planar cell polarity (PCP) and Ca^{2+}. In the PCP pathway, Frizzled receptor activation stimulates RHOA and RAC1, which in turn activate actin polymerization and transcription factors, via ROCK and JNK. This pathway regulates cell polarity, cell motility and morphogenetic movements. The Ca^{2+} pathway is activated by heterotrimeric G protein activation. This induces subsequent PLC activation producing DAG and InsP3, which trigger Ca2+ release into the cytoplasm. This, in turn, activates actin polymerization and transcription factors that mediate cell fate and migration.

1.3.1.2. Pathway regulation

Wnt signaling is widely expressed and involved in many functions and organs. Therefore, it requires a finely-tuned regulation. A key regulatory mechanism is the specific interaction between the Wnt receptors and their ligands. Frizzled receptors are ubiquitous in all Wnt signaling, so specificity is determined by the co-receptor they interact with. For instance, when combined with LRP5 and 6, they activate β-catenin dependent pathway. When combined with ROR or PTK7, they activate the PCP signaling and with RYK, both canonical and non-canonical. The other receptors also exhibit pathway specificity activation: MUSK and syndecan for PCP, and glypican for β-catenin and PCP (90). Moreover, the expression of certain ligands is restricted to specific locations, and their interaction is further specified by the receptor they bind to. For instance, Wnt7 is expressed in the brain and its interaction with Gpr/Reck results in specific activation (92).

Pathway regulation can occur through different agonists or antagonists extracellularly. Wnt agonists such as Rspondins and norrin have been identified. Rspondins1-4 have a similar structure, consisting of two N-terminal furin domains and one thrombospondin type I domain, which enhance β-catenin and PCP signaling, respectively. Rspondins can interact with three classes of transmembrane proteins: syndecans, Leu-rich repeat-containing G protein-coupled receptors (LGRs 4-6) and transmembrane E3 ubiquitin ligases (RNF43/ZNRF3). In the presence of Rspondins, they bind with high affinity to the LGR4-6 receptors via the furin ectodomain, together with ZNRF3, and leading to activation of canonical pathway. Rspo2-3 may signaling independently of Lgr4/6, by binding to heparan sulfate proteoglycans (HSPGs) via the thrombospondin domain (93). Similarly, syndecan can induce PCP signaling by binding to the LGRs through the thrombospondin domain (90, 91). Additionally, Norrin is a cysteine-knot protein that activates canonical Wnt by binding to Frizzled-4 and LRP5/6 (91).

Several antagonists have also been described such as Cerberus, Notum, Dickopf-related protein 1 (DKK1), secreted Frizzled-related protein (sFRP), WNT inhibitory factor (WIF), Sclerostin, and its homologue Wise (90, 91). They have different mechanisms of action. In the case of DKK and Sclerostin, they prevent the formation of the receptor complex. sFRP and WIF bind directly to Wnt, blocking their action in the receptors. Notum is a carboxylase that inactivates Wnts by removing the palmitate acid, thereby inhibiting canonical signaling (91).

Other regulatory mechanisms occur mostly at the intracellular level. The first occurs during their synthesis, since Wnts require posttranscriptional modifications. Acylation, specifically the incorporation of

palmitoleic acid into a conserved serine residue, is common to all Wnts. It is mediated by Porcupine, a palmitoyltransferase. This is necessary for the intracellular trafficking and is fully activated upon secretion. Later refinement steps include incorporation into Evi/Wls, which is a transmembrane protein that transports Wnts to the plasma membrane. There, they are secreted and act in a paracrine manner (90). In addition, receptors are also regulated based on their structure and accessibility in the membrane. They can undergo either phosphorylation (Frizzled, LRP6, RYK) or ubiquitinization, which induces receptor inactivation and/or internalization. They can also undergo proteolytic cleavage of the cytoplasmatic domain, or the extracellular portion at the lipid anchor level. These modifications apply mostly to the receptors, but also to other cytoplasmatic proteins that are intermediates in the pathway (90).

Another regulatory mechanism is internalization after the ligand has bound to the receptor. In this case, the ligand-receptor complex is endocytosed, sustaining or even enhancing the signaling. Caveolin mediates this type of endocytosis in canonical signaling and, clathrin in PCP pathway. Conversely, ZNRF3 and RNF43 mediate FZD multiubiquitinization, leading to receptor internalization and signaling downregulation (90).

1.3.2. Wnt signaling in physiological conditions

1.3.2.1. Embryo formation and vascular development

The high level of conservation of Wnt signaling during evolution highlights its relevance in physiological conditions, particularly during embryo development (29, 43, 90, 91, 94, 95). Wnt signaling plays a crucial role during the blastula stage, after several divisions of the fertilized egg. A Wnt signaling gradient, decreasing from the posterior to the anterior end, breaks the embryonic symmetry. The posterior end is enriched in Wnt ligands, while the anterior end is enriched in Wnt antagonists. Differential expression of Wnt, together with BMP and FGF components, induces the formation of the blastopore in the posterior end. This initiates nodal-mediated gastrulation leading to the three layers of the embryonic stage: ectoderm, endoderm and mesoderm. Each layer is committed to one specific fate. Mesoderm contains progenitor cells organized in the blood islands. Hemangioblasts, one of the precursor cell types, differentiate into ECs. They are involved in establishing the vascular bed that connects the yolk sac and the aortic primordia of the embryo proper. This process is mediated by vasculogenesis, in which these ECs proliferate, migrate and coalesce to form the primitive vascular network (96). Canonical Wnt signaling, in particular Wnt2, 3a and 5a, has been shown to mediate embryonic precursors´ differentiation into ECs (97-99). Additionally, the Wnt enhancer Rspo3 has also been reported to mediate EC differentiation (100,

101). Rspo3 is indispensable for development since its deletion induces embryonic lethality due to vessel remodeling defects (102).

Angiogenesis mediates the posterior development of the immature plexus into the complex branching of the mature vascular system. Sprout formation is regulated by canonical Wnt signaling, which is differentially expressed between stalk and tip cells. Stalk cells have high expression, while in tip cells is relatively low (43). Mechanistically, non-canonical Wnt signaling has been reported to play a role in ECs proliferation. Endothelial expression of Wnt5a activates non-canonical Wnt signaling, which in turn induces conventional angiogenic signaling such as Ang-Tie, leading to the proliferation and survival of ECs (103, 104).

Wnt is also involved in the final specification of the new blood vessels into the different vascular beds (43, 98). Different Wnt expression profiles influence the organotypicity of ECs (6, 43). For instance, the blood brain barrier (BBB) is one of the most specialized vascular beds in the mammalian body. Canonical Wnt signaling induced by Wnt7a and 7b, has been shown to induce EC differentiation in the CNS, contributing to the establishment of this elaborate and permeable network (43).

Vessel formation terminates postnatally in certain vascular beds. In this regard, the eye is the most commonly studied organ, where Wnts are also involved. Pericytes secrete Ang2, which induces the expression of Wnt7b in macrophages. This macrophage-derived Wnt7b binds to Lrp and Frizzled receptors in vascular ECs that regulate cell cycle entry and cell death, via myc and CDKN1a, respectively (105). ERG drives β-catenin stabilization via VE-cadherin and Frizzled 4, leading to vascular stability in postnatal retinal development and tumor angiogenesis (106). Furthermore, during postnatal arterial and arteriolar formation, Frizzled receptor 4 regulates EC proliferation and migration through non-canonical Wnt/PCP signaling, particularly in ischemia (107).

During vascular development and under physiological conditions, ECs are exposed to shear stress, which is regulated through Wnt signaling. Non-canonical Wnt ligands stabilize blood flow and induce EC polarization, making ECs responsive to shear stress. This process is particularly important in the primitive plexus during vascular network formation (108).

1.3.2.2. Liver development

Analogously to the mesoderm development, the endoderm is committed to hepatic differentiation due to reduced Wnt signaling and antagonist secretion from the anterior end of the endoderm. This allows

expression of HHEX, synergistically with other pathways. In parallel, the posterior end exhibits high Wnts, which prevents hepatic differentiation. Later, Wnt signaling increases in the anterior part of the endoderm leading to the formation of the liver bud. The bipotent hepatoblasts residing in the liver bud, proliferate rapidly in an undifferentiated state, inducing liver bud expansion. The hepatic fate commitment in hepatoblasts is determined by the expression of albumin and AFP. Later, β-catenin is involved in the proliferation of hepatoblasts and is responsible for both hepatocyte and cholangiocyte cell fate commitment. Mechanistically, the expression of HNF4α, C/EBPα, oncostatin M and HGF induces cells into hepatocyte fate, while HNF-1β, HNF-6 and the Notch–Jagged signaling commits the cell to cholangiocytes (95).

1.3.3. Wnt signaling in pathological conditions: the hallmarks of cancer

The description and subsequent updates of the "hallmarks of cancer" aimed to rationalize the complexity of cancer (109-111). Almost every hallmark is directly or indirectly mediated by Wnt signaling (112). Wnts are known to play an intrinsic role in tumorigenesis as oncogenic drivers of several cancers, including sustained proliferation, evading growth suppressors and cell death, replicative immortality, altered metabolism and genome instability. Besides, certain cancers such as CRC [113] or HCC [114] show Wnt alterations more often.

Furthermore, the importance of the TME in tumor progression has been highlighted by the "next generations" and "new dimensions" of the hallmarks of cancer. These include inducing angiogenesis, invasion and metastasis, tumor promoting inflammation and immune evasion (110, 111). The role of Wnt signaling in the TME has also been widely described (112). However, it remains somewhat controversial.

Angiogenesis is regulated through Wnt signaling in both physiological and pathological conditions. ECs mainly express non-canonical Wnt ligands, which are mediated via the Wnt ligand secretion factor Evi/Wls. These ligands act in an autocrine manner, upregulating Tek and downregulating Cdkn1a, Bax, and Stat2. This shifts the cell cycle into proliferation instead of apoptosis and has been described in both developmental retina and tumor angiogenesis (113). Similarly, Rspo3 is mainly secreted by ECs and its endothelial-specific KO phenocopies the one previously described for Evi ECKO. Analysis of commonly differentially expressed genes revealed that non-canonical vessel regression is mediated via Rnf213, Usp18 and Trim30α, which alters NFAT protein levels, regulating Wnt/Ca^{2+}/NFAT pathway (102).

Vascular developmental factors were repurposed to treat neurological disorders, such as glioblastoma and stroke. To ensure specificity and avoid side effects, Wnt7 agonists were genetically engineered to

bind Gpr124/Reck complex, resulting in BBB repair and vascular normalization, improving disease progression (114).

Furthermore, tumor invasion and metastasis are also mediated via Wnt signaling. In glioma, invasion is regulated mechanistically by Olig2 expression. Olig2-positive cells invade via vessel co-option, whereas negative-expressing cells do so via angiogenesis. Vessel co-option is regulated by Wnt7 from glioma oligodendrocyte-like cells (OPCL), and blocking its expression improves survival with standard glioma treatment (115). Similarly, in breast cancer cells, secretion of Rspo2 activates canonical Wnt signaling in an autocrine or paracrine manner, leading to the secretion of Dkk1 inhibitor. This, in turn, acts on osteoclasts precursor cells, recruiting them and preparing the niche for bone metastasis (116).

Tumor immune invasion is a hallmark with great therapeutic potential. The role of Wnt signaling has recently been investigated in this context. The canonical pathway in NSCLCs with high tumor mutation burden has been shown to impair anti-tumor immunity, resulting in reduced immune cell infiltration in the TME. Inhibiting Wnt β-catenin improves tumor T cell infiltration, both alone and in combination with PD1 blockade (117). In melanoma and pancreatic cancer, Rspo3 from ECs and cancer-associated fibroblasts (CAFs) activates Wnt signaling, which generates effective adaptive anti-tumor immunity via NK and subsequently T and dendritic cells. The expression of Rspo3 can be impaired by several factors of the TME. Supplementation of Rspo3 induces activation of cytotoxic effector cells, alone and in combination with anti-PD1 therapy (118).

Further elements of the TME mediate tumor progression via Wnt signaling, activating several hallmarks. In cutaneous squamous cell carcinoma (cSCC), higher levels of Wnt and porcupine activity were reported compared to the healthy tissue. Blocking this activity impairs CSC and their differentiation, indicating a Wnt-dependent role in sustaining the CSC niche (119). Rspo3 expression was also crucial for sustaining proliferation and tumorigenicity in a gestational tumor, choriocarcinoma (120).

Two Wnt interactive subpopulations have been identified in lung adenocarcinoma. A porcupine+ve population constitutes the niche for the Wnt responsive population. The former provides Wnt5a, Wnt7a and Wnt7b that bind to Frizzled receptors in the second subpopulation, activating canonical Wnt signaling. This signaling is reinforced by the secretion of Rspo1 and 3 from the niche cells, which act on Lgr 4 and 5 receptors in the Wnt responsive population. The outcome is the induction of CSC properties and impaired survival (121).

Similarly, although colorectal cancer harbors APC or β-catenin mutations, they do not always display high Wnt activity. This is sustained by myofibroblasts that secrete factors such as HGF, inducing stemness capability (122). In a physiological context, secretion of Wnt ligand influences the number of intestinal stem cells (ISC). Reducing its secretion led to a decrease in the number of cells, but an increase in the fixation of APC mutations, thereby increasing the probability of forming adenomas (123). In contrast, it was reported that supplementation of Rspo1 in CRC with Apc mutation, leads to less aggressive tumors and more prolonged survival, by altering Wnt and TGFβ signaling (124).

Wnt signaling has been extensively described in various tumor types and affects multiple hallmarks of cancer. It has been considered to be druggable (112, 125, 126). However, the safe and optimal manner to address this is still far from reality. Further investigation is required to determine whether the Wnt mechanism of activation changes for different tumor types and whether it has a pro or anti-tumorigenic effect.

2. AIMS OF THE STUDY

The consequence of angiocrine Wnt signaling in shaping liver homeostasis is a well-established concept. Despite the fact that the angiocrine Wnt factors serve as crucial regulators of liver function, their role during the pathophysiological condition, notably cancer, remains controversial. For instance, Wnt secretion derived from the TME has been reported to act both pro- and anti-tumorigenic in several tumor entities. Here, I investigated the function of angiocrine Wnt signaling during liver tumor progression.

I first aimed to establish a clinically relevant hepatocarcinogenesis model in order to mimic tumor initiation and progression. I developed various *in vivo* methods for inducing HCC that meet the following criteria: tumorigenesis (1) does not occur preferentially in one specific liver region, (2) exhibits different tumor growth patterns (i.e. focal and multifocal), and (3) recapitulates the TME. The focus was on the endothelium, and specifically on its Wnt secretion. The genes of interest for this study were the main drivers of angiocrine Wnts. These are: the Wnt enhancer-Rspo3 that regulates liver metabolic zonation in physiological conditions, and the Wnt secretion factor-Evi/Wls that mediates the secretion of fully functionally produced Wnt ligands.

Secondly, I explored the impact of Wnt signaling on HCC development, focusing on the angiocrine effect during tumor initiation and the autocrine effect during angiogenesis. Additionally, I investigated the crosstalk between tumor cells and (tumor) endothelial cells.

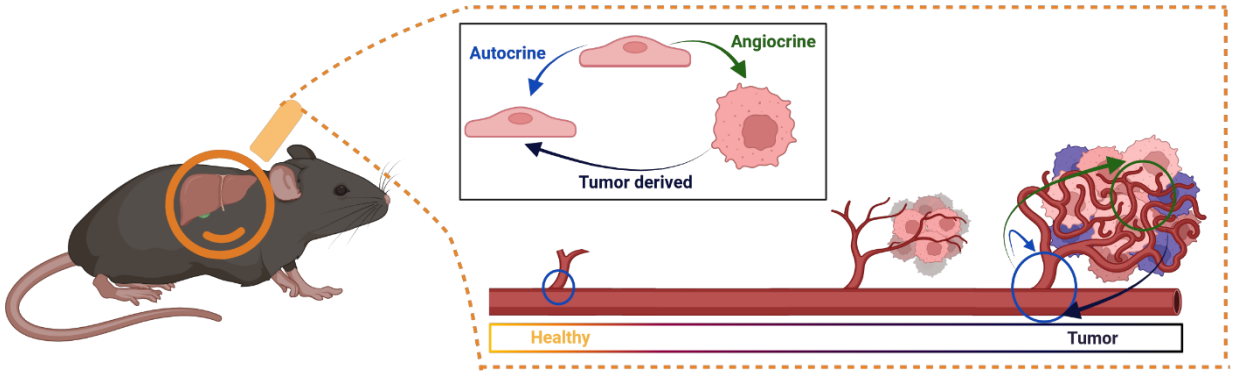

Figure 7. Schematic representation of the aims of the study
This project aimed to investigate the impact of endothelial-derived Wnt signaling on HCC initiation. To address this question, various *in vivo* murine models were established. Rspo3 and Evi/Wls expression was investigated in healthy and tumor ECs, in both murine and human samples. The effect of angiocrine Wnt secretion in HCC initiation was studied by deleting endothelial Rspo3 and Evi/Wls secretion prior to tumor induction and analyzing the tumor cells and the TME at the morphological and transcriptomic level. The study focused on the crosstalk between tumor cells and tumor ECs analyzing the autocrine, angiocrine and tumor derived effect.

3. RESULTS

3.1. Establishment of advanced *in vivo* and *in vitro* murine models for HCC induction

3.1.1. Establishment of a local electroporation HCC model

Most HCC models induce tumorigenesis preferentially in a specific liver zone and fail to fully recapitulate human hepatocarcinogenesis (85-87). It was, therefore, essential to circumvent these limitations, in order to address the main question of this project. Consequently, a local electroporation model was established based on the transformation of some of the most commonly mutated genes in HCC: deletion of p53 and overexpression of cMyc and KRas (31). All of these mutations were introduced under the albumin promoter to ensure their specific transduction in hepatocytes. Deletion of p53 was induced via the CRISPR/Cas9 system and overexpression via the sleeping beauty transpose, SB13. Several combinations of these transgene and oncogenes were assessed: p53 alone, in combination with cMyc or KRas and the combination of all three (**Fig. 8A**), by electroporating 25μg of each plasmid in the left liver lobe of 8 weeks old mice. Tumor incidence after 13 weeks and time for tumor initiation and progression were the main readouts used to determine the most relevant plasmid combinations. No tumor was detected with the electroporation of p53 plasmid alone or in combination with KRas. In parallel, tumors were detected already at two weeks post electroporation with a 100% tumor incidence using the combination of p53, cMyc and Kras (**Fig. 8B**). Given that the triple mixture of p53, cMyc and Kras robustly developed aggressive tumors, I focused on the combinations of cMyc together with p53 or KRas. The cMyc-p53 pair induced tumors between 6 weeks and 13 weeks with an incidence of 50%, whereas KRas and cMyc initiated tumor development at 7 weeks in 40% of the mice. In both combinations, the incidence was higher in males compared to females (75 and 25%; 50 and 25%) (**Fig. 8B**) mimicking the clinical setting (31). Therefore, I decided to perform electroporation of p53 deletion and cMyc overexpression on male mice as the most representative electroporation-based HCC model based on the efficacy and time for tumorigenesis.

A

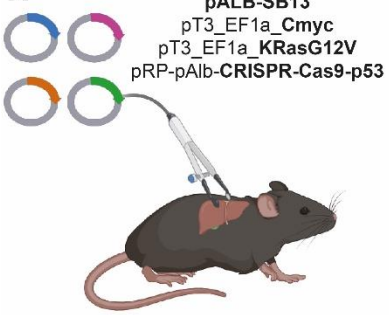

B

Plasmid combination	Tumorigenesis	Incidence
pRP-pAlb-**CRISPR-Cas9-p53**	ND	0%
pALB-SB13 pT3_EF1a_**KRasG12V** pRP-pAlb-**CRISPR-Cas9-p53**	ND	0%
pALB-SB13 pT3_EF1a_**Cmyc** pRP-pAlb-**CRISPR-Cas9-p53**	6-13 weeks	50% (25%♀, 75% ♂)
pALB-SB13 pT3_EF1a_**Cmyc** pT3_EF1a_**KRasG12V**	7 weeks	40% (25%♀, 50% ♂)
pALB-SB13 pT3_EF1a_**Cmyc** pT3_EF1a_**KRasG12V** pRP-pAlb-**CRISPR-Cas9-p53**	1-2 weeks	100%

C

D

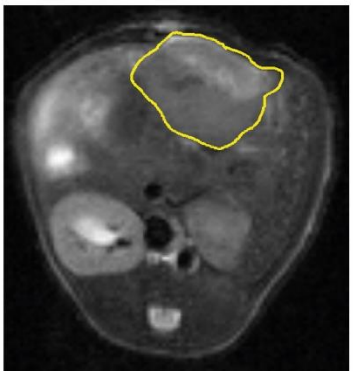

Figure 8. Description of the focal electroporation HCC model
A) Schematic representation of the model showing the different plasmids: pAlb-SB13, pT3_EF1a_Cmyc, pT3_EF1a_KRasG12V and pRP-Alb-CRISPR-Cas9-p53. **B**) Table showing the different plasmid combinations electroporated in the left liver lobe, the time for tumor formation until mice reached endpoint criteria up to 13 weeks and the incidence (n=4 in each group). **C**) Representative picture of a tumor bearing mice from p53 deletion and cMyc overexpression 7 weeks after electroporation (left liver lobe) "B". **D**) MRI scan of the same tumor as shown in C.

The model combining p53 deletion and cMyc overexpression was advanced first by introducing luciferase expression to measure tumor volume. This was transduced by another plasmid that works with the same sleeping beauty transposase (SB13) system as for cMyc. Mice expressing luciferase in the tumors metabolize luciferin upon luciferin injection and generate bioluminescence that is measured by *In vivo* Imaging System (IVIS). The intensity of bioluminescence is directly proportional to the tumor volume (**Fig. 9A**). Next, I further reduced the plasmid concentration up to 8 μg of each plasmid for better efficacy of the electroporation without translating this in changes in tumor incidence. Two independent pathologists characterized and confirmed the model as HCC. Hematoxilin-Eosin staining showed undifferentiated tumors (**Fig. 9B**) occasionally with the typical HCC vasculature (**Fig. 9C**). Moreover, Hepar positive (marker of HCC tumors) (**Fig. 9D**) with a barely negative CKPan (a marker of epithelial tumors) (**Fig. 9E**), led to

categorize the tumors as undifferentiated HCC. Besides, glutamine synthetase expression was dramatically reduced (**Fig. 7F**). This model was then described as a non-proliferative HCC subtype, according to the classification described by Llovet *et al*. (31). This focal HCC model is from now referred to as EPO.

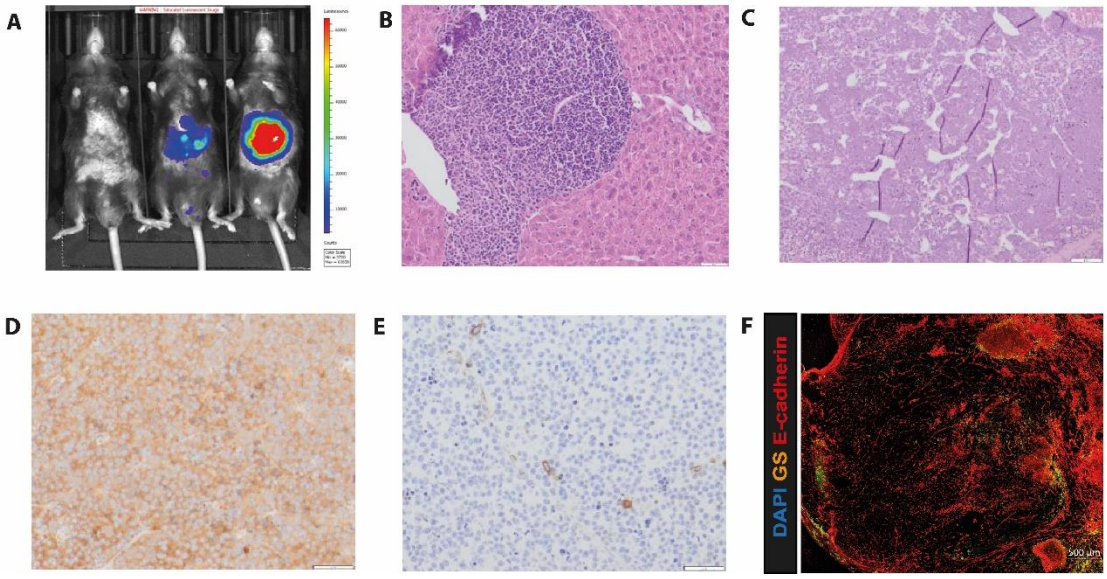

Figure 9. Refinement and characterization of the plasmid combination of p53 deletion and cMyc overexpression
A) Representative images of tumor bearing mice under IVIS measurement, expressing luciferase at different intensities due to different tumor volume. **B**) Representative images of H&E staining of an EPO tumor. **C**) Representative Hepar staining of an EPO tumor, scale bar 500µM. **D**) Representative CK-Pan staining of an EPO tumor, scale bar 500µM. **E**) Representative immunofluorescence staining of an EPO tumor showing in green glutamine synthetase and E-cadherin in red, scale bar 500µM.

3.1.2. Establishment of tumor-derived organoids from local and multifocal HCC models

Tumor-derived organoids were established from both HCC murine models from EPO and iAST. Tumor-derived organoids are much more complex than conventional cell line system, thereby making them a powerful tool for screening and mechanistic experiments. Organoids are cultured in a complex and elaborated medium that prevents positive selection and transdifferentiation. This avoids the formation of a monoclonal culture and maintains its stemness properties.

Tumor tissue was isolated from the focal EPO tumor, or from several nodules in the iAST model. The tissues were processed as described in section 5.2.4. In brief, tumors were minced and washed several times to remove large debris. Tumor samples were further digested with Collagenase D and DNase I solution, washed and finally mixed with Basement Membrane Extract (BME) (**Fig. 8A**). Tumor-derived

organoids were successfully maintained in culture for up to 16 passages (**Fig. 8B**) in a defined medium as indicated in section 5.2.4. The medium was further supplemented with mNoggin for the first three days after isolation. Furthermore, supplementation of Wnt ligands in the medium is a standard for different organoids and tumor-derived organoid cultures. Yet, the supplementation of Wnt ligands is dependent on the mutational status of the original tumor (i.e. when the tumor has β-catenin mutations, Wnt supplements are not required in the medium). The reason to test this was also that Wnts were part of the research question, therefore, addition of unnecessary Wnt supplements to the medium may have introduced a bias. Therefore, I tested whether the Wnt supplements, Rspo1 and Wnt3a, were required in the complete medium. Tumor-derived organoids had better growing efficacy in the absence of both. Furthermore, biobanking (e.g. freezing at -80^{o}C and later thawing) was successful. In this case, the organoids were supplemented with mNoggin after thawing. Tumor derived organoids were further characterized by staining for the general cytoplasmatic and nuclear markers, phalloidin and DAPI, and Epcam as a HCC marker (**Fig. 8C**).

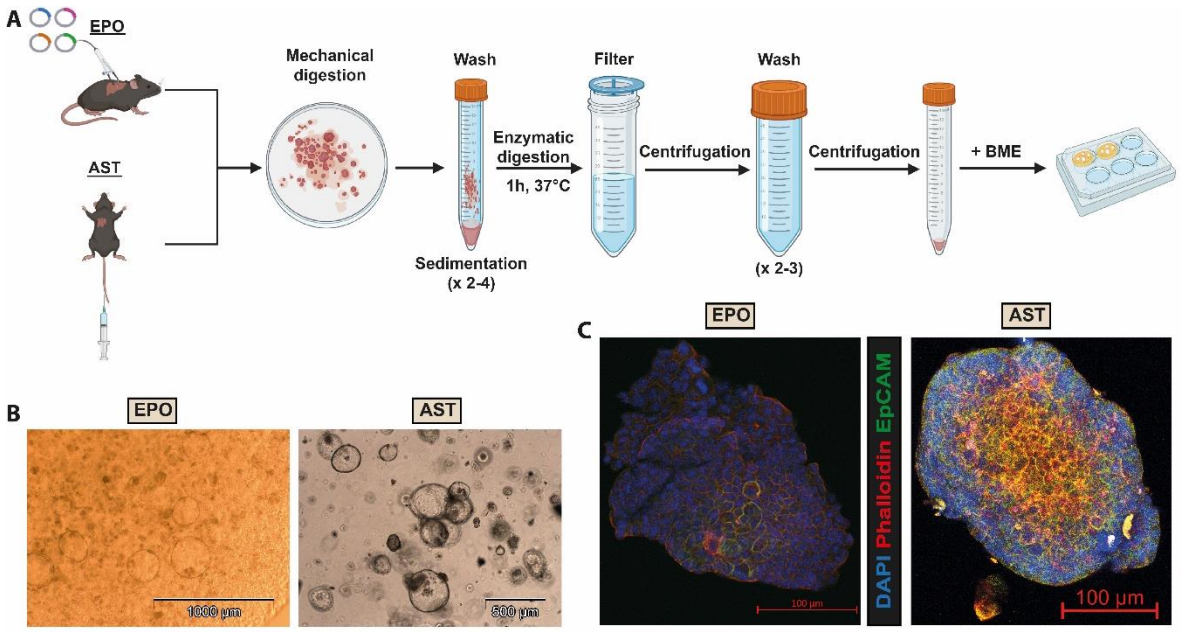

Figure 10. Establishment of tumor-derived organoids from the *in vivo* murine HCC models
A) Schematic representation of the isolation protocol to establish tumor-derived organoids from EPO and iAST tumor models. **B**) Representative images of tumor-derived organoids from both models at passage 6 under a bright field microscope; scale bar 1000µM and 500µM. **C**) Representative images of confocal microscopy shown as a maximum projection of fluorescence organoids for both HCC models stained for DAPI in blue, phalloidin in red and EpCAM in green; scale bar 100µM.

3.2. Angiocrine Wnt signaling affects HCC initiation and progression

3.2.1. Endothelial Wnt signaling is decreased in selected murine HCC models

To study the effect of endothelial-derived Wnt signaling in HCC, I investigated the expression of *Rspo3* and *Evi/Wls* in isolated liver ECs and tumor endothelial cells from the EPO and iAST models. In the EPO model, tumor transformation occurred locally in the electroporated left lobe. Thus, I could obtain both, healthy and tumor samples from the same liver (**Fig. 11A**). In contrast, for the iAST model, non-injected iAST transgenic mice were used as controls (**Fig. 11D**). In both models, Rspo3 (**Fig. 11B, E**) and Evi/Wls expression (**Fig. 11C, F**) were decreased in tumor ECs, being this decreased statistical significance in the case of Rspo3. These findings suggested reduced expression of angiocrine Wnt signaling in HCC compared to healthy liver endothelium.

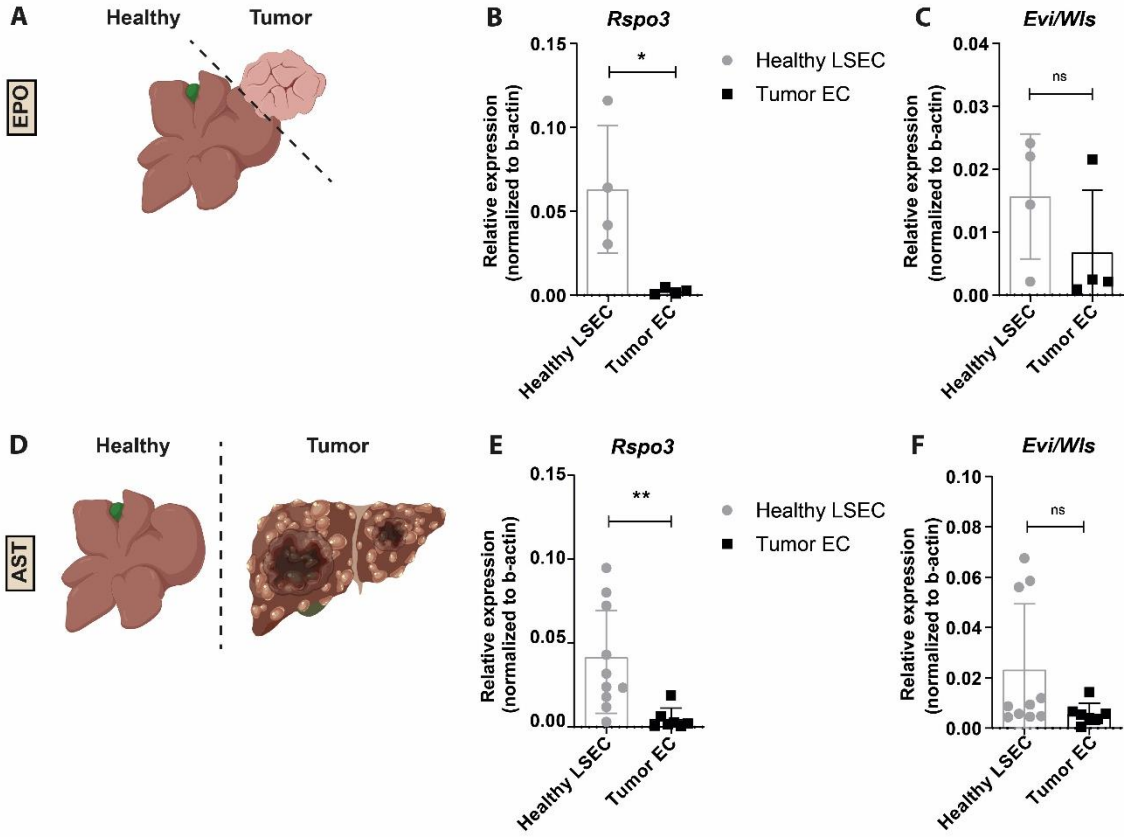

Figure 11. Endothelial expression of Wnt genes of interest is decreased in the murine HCC models compared to healthy livers

A) Representation of electroporation (EPO) liver showing the healthy and tumor sections. **B**) Expression of Rspo3 in isolated ECs from healthy and tumor EPO livers. **C**) Expression of Evi/Wls in isolated ECs from healthy and EPO-derived tumors. **D**) Representation of iAST transgenic model (iAST) showing healthy and iAST-derived tumors. **E**) Expression of Rspo3 in isolated ECs from healthy and tumor iAST livers. **F**) Expression of Evi/Wls in isolated ECs from healthy and tumor iAST livers. Each point represents one biological replicate. Gene expression was normalized to b-actin. Data are represented as mean ± s.d. p-value by unpaired t-test; ns, not significant; * $p<0.05$, ** $p<0.01$.

3.2.2. Endothelial-specific deletion of Wnt secretion promotes maturation of the tumor vasculature

Based on the downregulation of Rspo3 and, to a lesser extent, Evi/Wls in tumor ECs, I investigated their role in HCC initiation by deleting the entire endothelial Wnt secretion machinery prior to tumor initiation. Five consecutive i.p. injections of tamoxifen induced endothelial-specific deletion of Rspo3 and Evi/Wls floxed genes in Rpo3floxed x Evi/Wls floxed x VE-CadCreERT2 mouse line. Cre – mice, without cre, but containing the floxed alleles were used as a control. Since glutamine synthetase (GS) expression is controlled by endothelial-derived Rspo3 and Wnt factors, the genetic recombination efficacy can be easily traced by the loss of GS expression. Therefore, GS expression served as an experimental readout of EC specific Wnt deletion in all experiments. Tumors were induced by focal electroporation (**Fig. 12A**). Mice were euthanized when they had reached the endpoint criteria. Loss of GS expression validated endothelial specific *knock-out* (KO) of the candidate genes, Rspo3 and Evi/Wls (**Fig. 12C, D**). Tumor formation was determined by luciferase activity (**Fig. 12B**), showing a slightly delay in tumor initiation in the Cre + group. Tumor growth was indicated by the slope of the luminescence intensity, showing similar tumor growth in both groups (**Fig. 12B**). The tumor vasculature was studied in the resulting tumors to investigate the role of autocrine Wnt on tumor vasculature. Rspo3 and Evi/Wls deletion showed a slight decrease tumor vessel area (**Fig. 12E, G**) as previously reported in single Rspo3 and Evi/Wls deletion (102, 113). The vasculature was more mature as indicated by increased aSMA coverage (**Fig. 12E, F**).

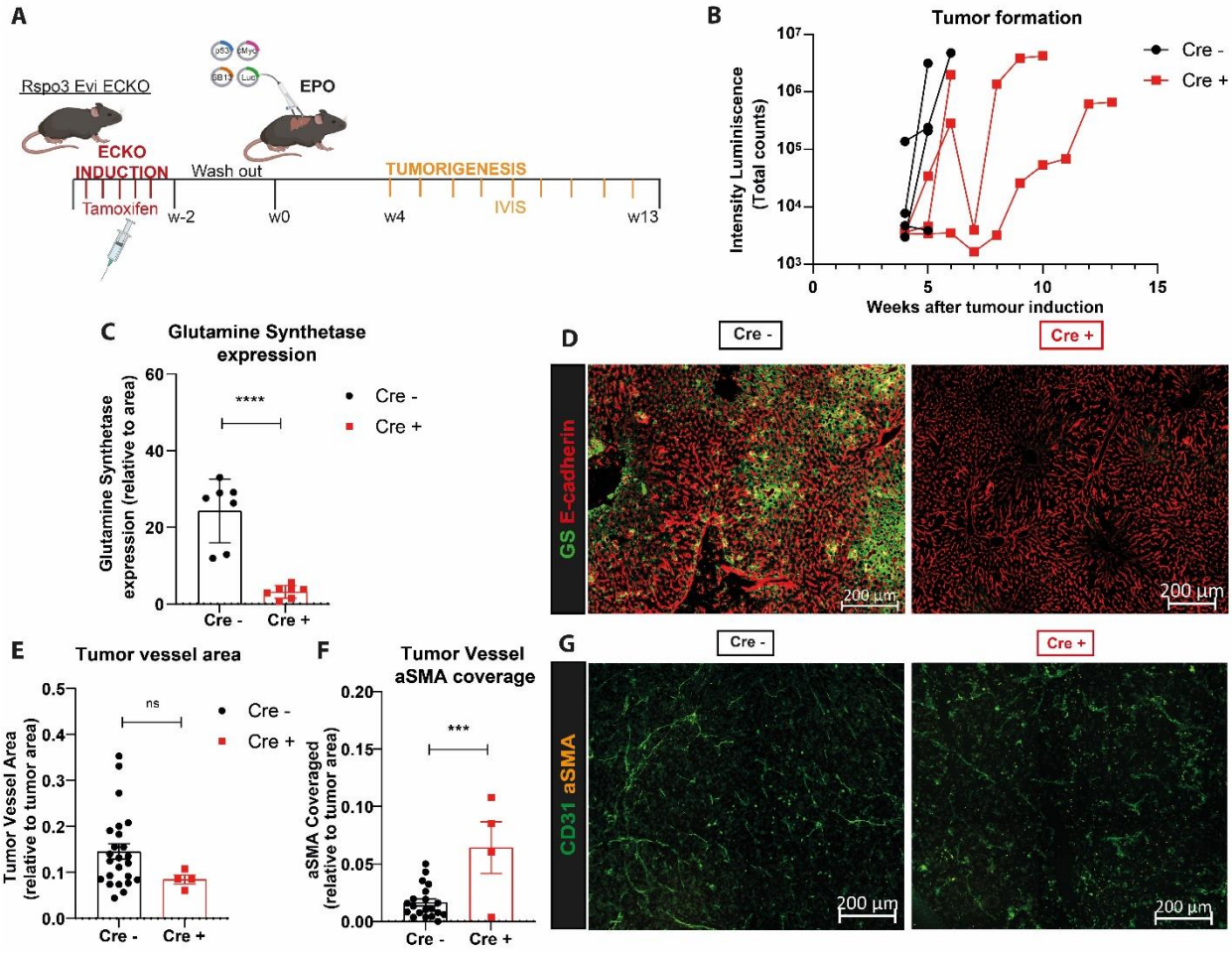

Figure 12. Tumor formation of focal electroporation model in Rspo3-Evi-iECKO mice
A) Schematic representation of the experimental design showing tamoxifen injection for ECKO induction, followed by wash - out period, electroporation for tumor induction and IVIS measurement during tumorigenesis at indicated timepoints. **B**) Intensity of luminescence measured via IVIS to determine tumor growth over time in Cre – and Cre + mice from Rspo3-Evi/Wls-iECKO (Cre-, n=4; Cre +, n=3). **C**) Quantification of Glutamine Synthetase immunofluorescence staining in livers extracted from Rspo3-Evi/Wls-iECKO, Cre – and Cre + mice. **D**) Representative images of Glutamine Synthetase immunofluorescence staining as quantified in C, scale bar 200µm. **E**) Quantification of CD31 immunofluorescence staining as vessel area relative to tumor area in percentage in livers extracted from Rspo3-Evi/Wls-iECKO, Cre – and Cre + mice. **F**) Quantification of aSMA immunofluorescence within CD31 staining as tumor vessel coverage relative to tumor area livers extracted from Rspo3-Evi/Wls-iECKO, Cre – and Cre + mice. **G**) Representative images of immunofluorescence staining of CD31 and aSMA as quantified in E and F, scale bar 200µm. Data are represented as mean ± s.e.m. (B), mean ± s.d. (C, E, F) and p-value by unpaired t-test (C, D, F), each point represents one liver section analyzed (C, E, F); ns, not significant; *** p<0.001, **** p<0.0001.

3.2.3. Deletion of endothelial-specific Wnt secretion increases tumor burden in a multifocal HCC murine model

Results of in the focal electroporation-based model investigating endothelial deletion of both candidate genes, Rspo3 and Evi/Wls, were complemented in the iAST model. In this GEM model, the SV40 Tag is

under the albumin promoter and its expression is prevented by a floxed stop cassette. Intravenous injection of AdCre induces the deletion of the stop cassette and expression of SV40, leading to multifocal HCC tumors. This model was further established by crossing the Rspo3-Evi/Wls-iECKO mouse line with the iAST. First, I characterized this mouse line by validating Rspo3 and Evi/Wls expression and its functional consequences. The double KO mice phenotype was characterized by significantly decreased mRNA expression of Rspo3 and Evi/Wls in isolated ECs (**Fig. 13A, B**), leading to significantly reduced expression of the central vein marker, GS (**Fig. 13C, D**). The iAST phenotype showed HCC nodules starting 5 weeks after intravenous injection of AdCre (**Fig. 13E**).

Next, I investigated tumor formation at the same time point in an endothelial Wnt deficient microenvironment. The genetic recombination was induced by 5 consecutive shots of tamoxifen i.p. followed by 2 weeks of wash-out period, and later injection of AdCre to activate SV40 expression (**Fig. 14A**). The genetic recombination efficacy was evaluated based on GS expression, as before (**Fig. 14C-D**). Tumor detection by MRI (**Fig. 14B**) showed that Cre + mice developed tumors at 5 weeks, while it was delayed up to week 7 in the Cre – group. Tumor burden in terms of number of nodules (**Fig. 14E**), liver body/weight ratio (**Fig. 14F)** and tumor volume (**Fig. 14G**) was increased in the absence of endothelial Wnt secretion. It is worth mentioning that Cre + mice have a lower liver body/weight ratio at baseline, so this may not be a relevant experimental readout as it could mask the differences in tumor burden. Overall, these data suggested that deletion of angiocrine Wnts accelerates HCC tumor initiation.

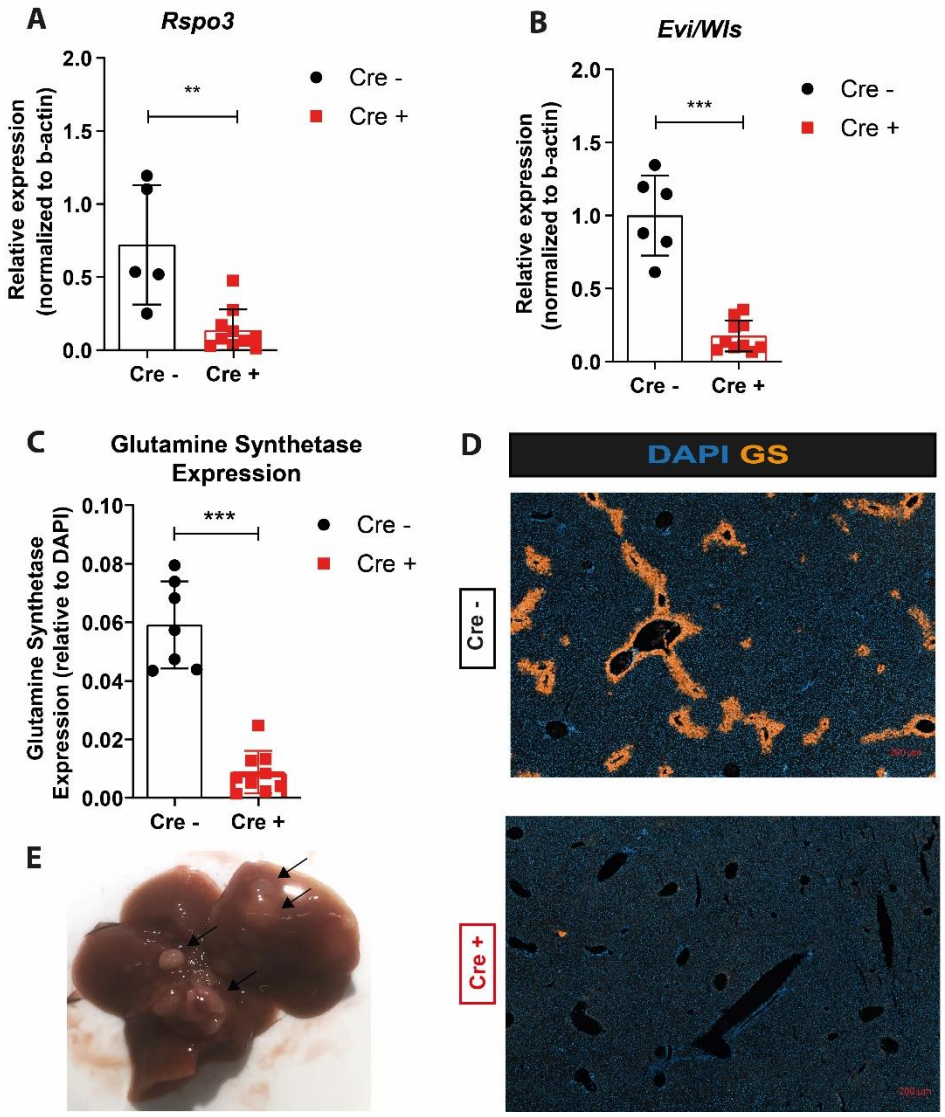

Figure 13. Characterization of Rspo3-Evi/Wls-iECKO-iAST mouse line

A) Relative gene expression of *Rspo3* in isolated tumor endothelial cells from Rspo3-Evi/Wls-iAST, Cre – and Cre + mice. **B**) Relative gene expression of *Evi/Wls* in isolated tumor endothelial cells from Rspo3-Evi/Wls-iAST, Cre – and Cre + mice. **C**) Quantification of Glutamine Synthetase immunofluorescence staining in livers extracted from Rspo3-Evi/Wls-iAST, Cre – and Cre + mice. **D**) Representative images of Glutamine Synthetase immunofluorescence staining as quantified in C, scale bar 200µm. **E**) Representative images of a tumor bearing liver from the Rspo3-Evi/Wls-iAST mouse line, black arrows indicating nodules. Gene expression was normalized to b-actin (A, B). Each point represents one biological replicate; data are represented as mean ± s.d. p-value by unpaired t-test; ns, not significant; * $p<0.05$, *** $p<0.001$.

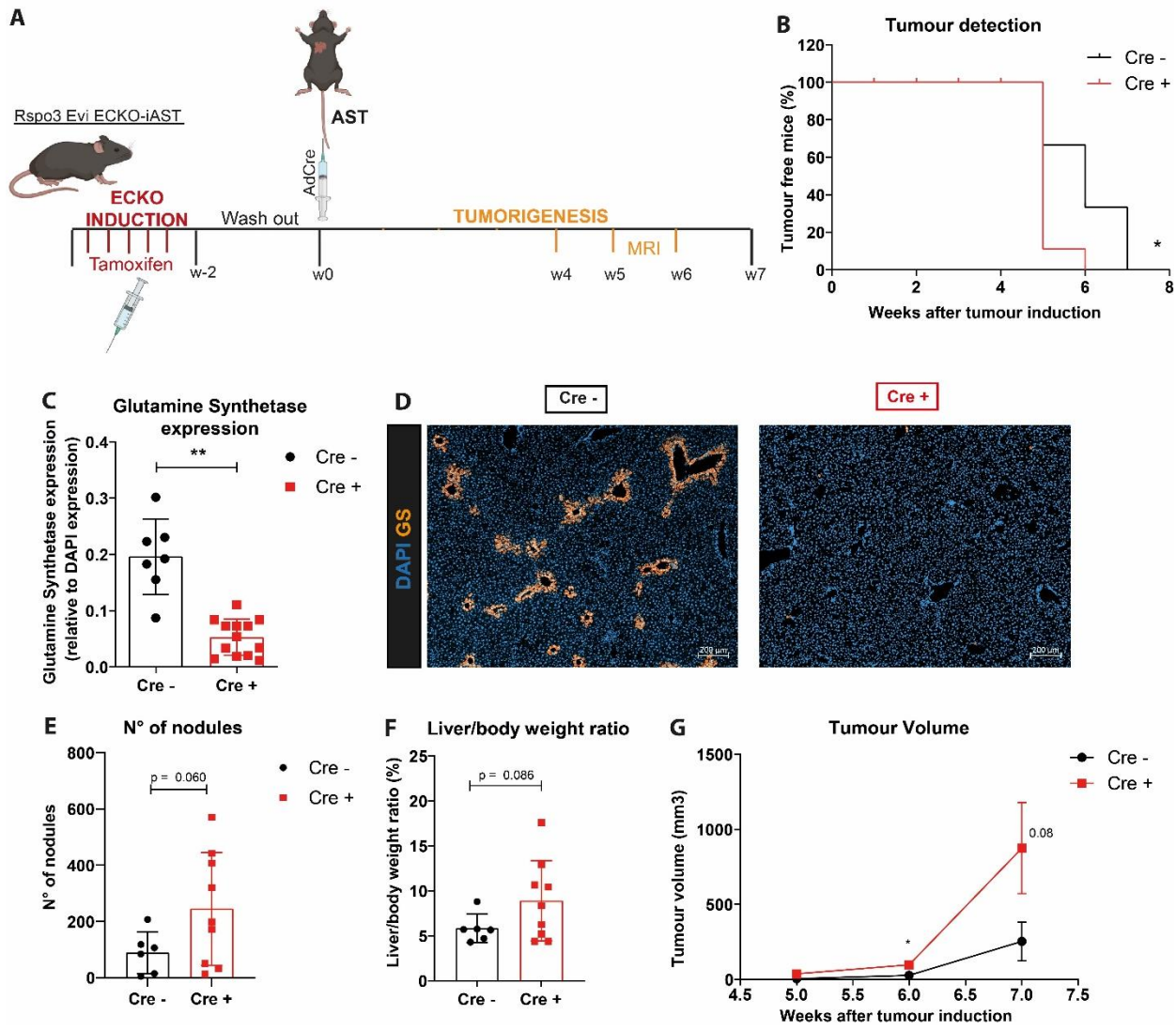

Figure 14. Complete deletion of angiocrine Wnt factors in the GEM iAST accelerated tumor formation
A) Schematic representation of the experimental design showing tamoxifen injection for ECKO induction, followed by wash-out period, Ad-Cre injection for tumor induction and MRI measurement during tumorigenesis at indicated timepoints. **B**) Kaplan-Meier survival representing the percentage of tumor-free mice after tumor induction (Cre-, n=6; Cre +, n=9). **C**) Quantification of the number of nodules in the livers at the endpoint of Cre – and Cre + mice. **D**) Liver/body weight ratio (%) at the endpoint of Cre – and Cre + mice. **E**) Quantification of tumor volume in mm^3 overtime based on MRI DICOM images by adding up the area of manually selecting tumor nodules and multiplied by slide thickness. Each point represents one biological replicate; data are represented as mean ± s.d. (C-D) and mean ± s.e.m. (E) p-value by Kaplan-Meier survival analysis (B) and unpaired t-test (C-D) and at each time point (E); * p<0.05, ** p<0.01.

3.2.4. Endothelial Wnt deletion induces a decrease of tumor vessels in the TME in multifocal HCC murine models

I interrogated how the TME contributed to the establishment of this protumorigenic environment in a Wnt dependent manner. Several parameters of the tumor itself and the TME were analyzed. First, the

pathological evaluation revealed no infiltrative growth pattern and no difference in tumor growth pattern (i.e. pseudoglandular, solid, trabecular) between the groups. Besides, tumor necrosis was only present in 3 out of 17 samples, all from the Cre + group. E-cadherin, a marker of liver tumors (127) and downstream of Wnt signaling, was not altered between both groups (**Fig. 15A, B**), indicating an angiocrine effect independent of this marker. Since it was described that Rspo3 mediates the TME immune status in other tumor entities (118), CD3 infiltration was evaluated as a parameter of tumor immune activation in the iAST model. No difference in the number of infiltrated CD3 positive T cells per nodule was detected (**Fig. 15C, D**). Tumor vascular area was measured as a readout of the Wnt autocrine effect and as performed previously in the EPO model (**Fig. 12E-G**). Cre + mice showed a significantly decreased in tumor vessel area per nodule at different nodule size ranges (**Fig. 15E, F**). This vessel phenotype did not fully explain the increased tumor burden described in **Fig. 14**.

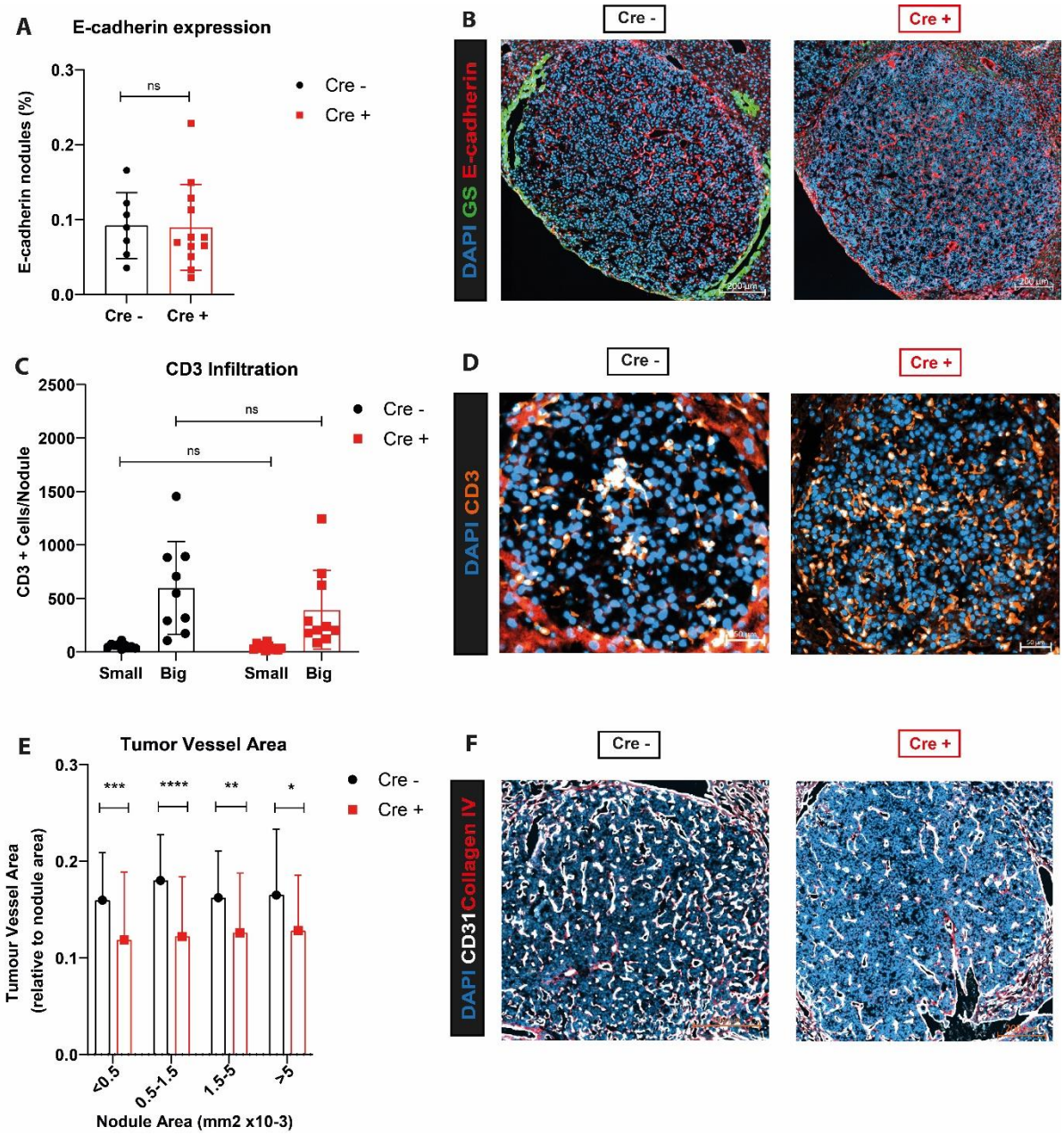

Figure 15. Deletion of angiocrine Wnts in the multifocal iAST model leads to reduced tumor vessel area and minor changes in other components of the TME

A) Quantification of E-cadherin immunofluorescence staining in tumor nodules from Rspo3-Evi/Wls-iAST, Cre – and Cre + mice, scale bar 200µm. **B**) Representative images of E-cadherin immunofluorescence staining in tumor nodules as quantified in A. **C**) Quantification of CD3 cells per liver nodule by immunofluorescence staining from Rspo3-Evi/Wls-iAST, Cre – and Cre + mice, scale bar 200µm, threshold between small/big nodules 0.5mm. **D**) Representative images of CD3 immunofluorescence staining in tumor nodules as quantified in C. **E**) Quantification of tumor vessel area by CD31 immunofluorescence staining in tumor nodules from Rspo3-Evi/Wls-iAST, Cre – and Cre + mice, scale bar 200µm. **F**) Representative images of vessel (CD31) immunofluorescence staining in tumor nodules as quantified in E. Data are represented as mean ± s.d. (A-C) (each point corresponds to one tissue section) and mean ± s.e.m. (E) p-value by unpaired t-test; ns, not significant; *** p<0.001.

3.2.5. Deletion of angiocrine Wnt signaling induces earlier tumor formation but does not translate into a difference in survival in a multifocal HCC murine model

I interrogated whether the difference in tumor initiation, and tumor burden, may translate into a difference in survival. The same experimental setup was used and the mice were kept until they reached the endpoint criteria (**Fig. 16A**). ECKO validation was performed based on Rspo3 and Evi/Wls expression in isolated ECs (**Fig. 16D, E**). As previously described (**Fig. 14**), Cre + mice developed tumors earlier (**Fig. 16B**). However, this did not translate into a difference in survival (**Fig. 16C**). The systemic liver damage markers, aspartate aminotransferase (AST) and Alanine transaminase (ALT), were analyzed to follow disease progression. The time points selected were: "baseline" (when MRI measurements started), right before tumor detection, when the tumor was first detected and the endpoint. At these time points, no statistically significant difference were detected in AST and ALT (**Fig. 16M, N**). I hypothesized that the observed differences in tumor initiation and tumor vessel area (**Fig.12, 14, 15**) are due to a local effect, based on the lack of significant changes in survival and liver enzymes (**Fig. 16C, M, N**). Therefore, the expression of Wnt ligand receptors and other members of the Wnt signaling pathway, that are also some of the most common cancer stem cell (CSC) markers, was analyzed by qPCR. Both tumor endothelial cells (TEC) and tumor cells (TC) showed no significant difference in the expression of the Wnt enhancer receptor, Znrf3 (**Fig. 16F, G**). While Lgr5 was lowly expressed in TEC (Ct value not detected), it showed a slight decrease in TC (p value=0.0527) (**Fig. 16H**). Other CSC or proliferation markers such as Ki67, Axin2 or ICAM-1 presented no difference between both groups (**Fig. 16J-L**). Only CD44, a CSC marker and a downstream of Wnt signaling, exhibited an increase in the Cre + group (p value=0.0709) (**Fig. 16I**). Overall, the increase in CD44 and decrease in Lgr5 expression did not explain the angiocrine and autocrine phenotype (**Fig. 12, 14-15**), but may indicate the presence of a CSC pool independent of Lgr5-Wnt signaling.

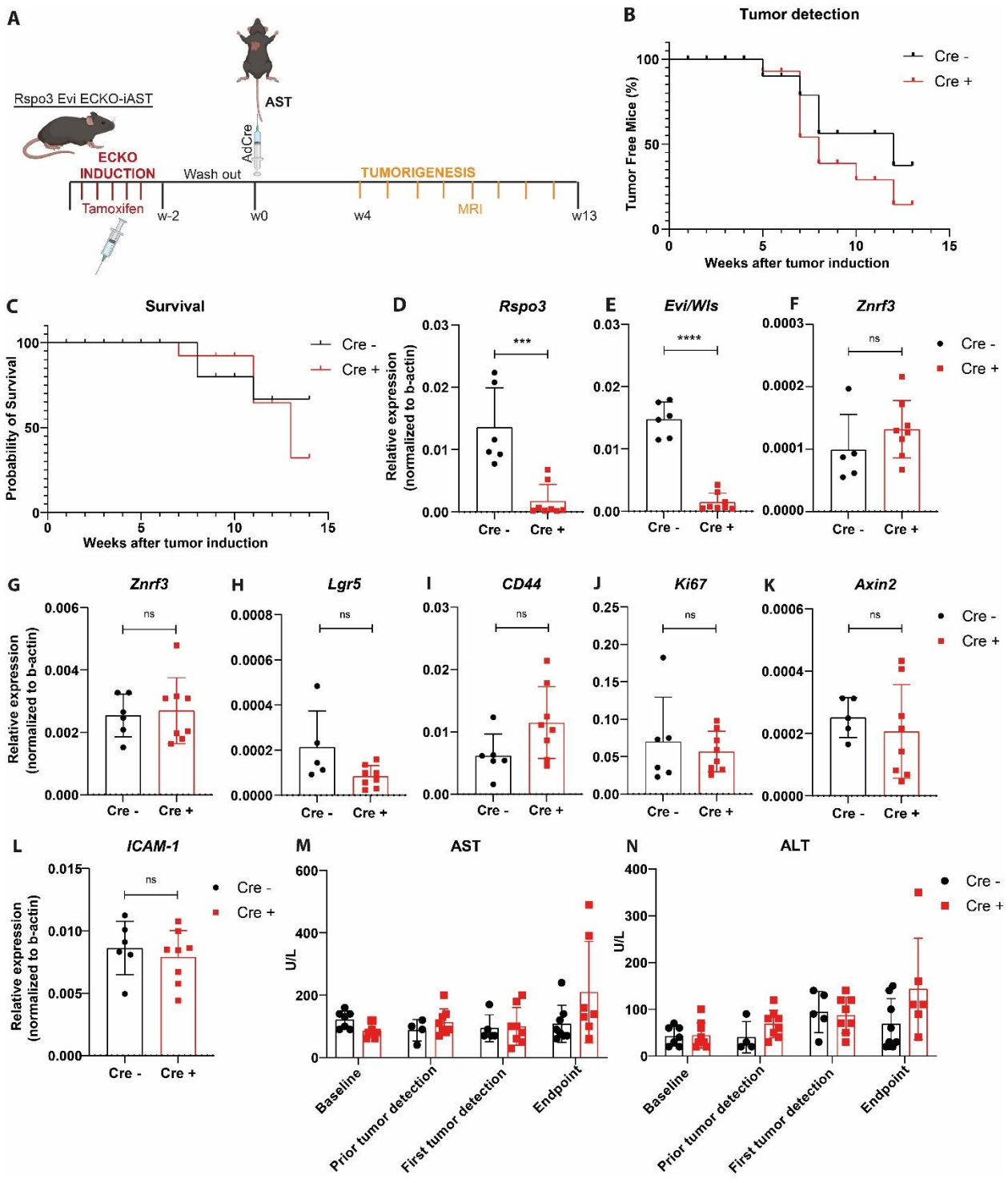
A
Rspo3 Evi ECKO-iAST
AST
AdCre
ECKO INDUCTION
Wash out
TUMORIGENESIS
Tamoxifen
w-2
w0
w4
MRI
w13
B
Tumor detection
Tumor Free Mice (%)
Weeks after tumor induction
Cre -
Cre +
C
Survival
Probability of Survival
Weeks after tumor induction
D
Rspo3
E
Evi/Wls
F
Znrf3
Relative expression (normalized to b-actin)
G
Znrf3
H
Lgr5
I
CD44
J
Ki67
K
Axin2
L
ICAM-1
M
AST
N
ALT
U/L
ns
Baseline
Prior tumor detection
First tumor detection
Endpoint

Figure 16. Deletion of angiocrine Wnt factors in the GEMM is dispensable for tumor progression
A) Schematic representation of the experimental design showing tamoxifen injection for ECKO induction, followed by wash-out period, Ad-Cre injection for tumor induction and MRI measurement during tumorigenesis at indicated time points. **B**) Kaplan-Meier survival represents the percentage of tumor-free mice after tumor induction. **C**) Kaplan-Meier survival representing the percentage of alive mice after tumor induction (Cre-, n=8; Cre +, n=10). **D**) Relative gene expression of Rspo3 and **E**) Evi/Wls in isolated tumor endothelial cells from Rspo3-Evi/Wls-iECKO-iAST Cre – and Cre + mice. **F**) Relative gene expression of the Wnt receptor Znrf3 in isolated tumor endothelial cells and **G**) tumor cells from Rspo3-Evi/Wls-iECKO-iAST Cre – and Cre + mice. **H**) Relative gene expression of the CSC marker and Wnt receptor Lgr5, **I**) CSC marker and Wnt downstream target CD44, **J**) proliferation marker ki67, **K**) Wnt downstream target Axin2, **L**) CSC marker ICAM-1 in isolated tumor cells from Rspo3-Evi/Wls-iECKO-iAST Cre – and Cre + mice. **M**) Levels of the blood liver damage markers AST and **N**) ALT (U/L) at baseline, right before tumor detection, first time tumor was detected by MRI and at the endpoint. Gene expression was normalized to b-actin (D-F). Each point represents one biological replicate; data are represented as mean ± s.d. (C-G). p-value by Kaplan-Meier survival analysis (B, C) and unpaired t-test (C-D) and at each time point (G); ns, not significant; *** p<0.001, **** p<0.0001.

3.2.6. Endothelial Evi/Wls is dispensable in the induction of a local electroporation based HCC murine model

I investigated whether the TME in HCC showed any specificity by a particular Wnt ligand (from Evi/Wls derived transport) or enhancer (Rspo3). Based on the differential *Rspo3* and *Evi/Wls* expression between healthy and tumor ECs (**Fig. 11**), I hypothesized that Rspo3 may be the main factor driving this phenotype and Evi/Wls was either dispensable or acted in a synergetic manner (**Fig. 12-14-16**). First, I focused on Evi/Wls to exclude a potential contribution of Evi/Wls mediated Wnt secretion. HCC was induced after a single Evi/Wls deletion (Evi/Wls iECKO) using the same experimental strategy as shown before, in the focal HCC model (**Fig. 17A**). The genetic recombination of Evi/Wls ECKO was confirmed based on the significantly decreased expression of GS (**Fig. 17C, D**). As expected, deletion of Wnt secretion led to no major differences in the time of tumor detection nor their growth. This was indicated by the similar growth curves in the intensity of IVIS luminescence during tumor formation (**Fig. 17B**). Analysis of the tumor vasculature revealed no significant differences in both tumor vessel area (**Fig. 17E, G**) and tumor vessel coverage (**Fig. 17F, G**). In short, these data suggested that endothelial Evi/Wls derived factors are dispensable for earlier tumor formation as shown in **Fig. 12-14-16**.

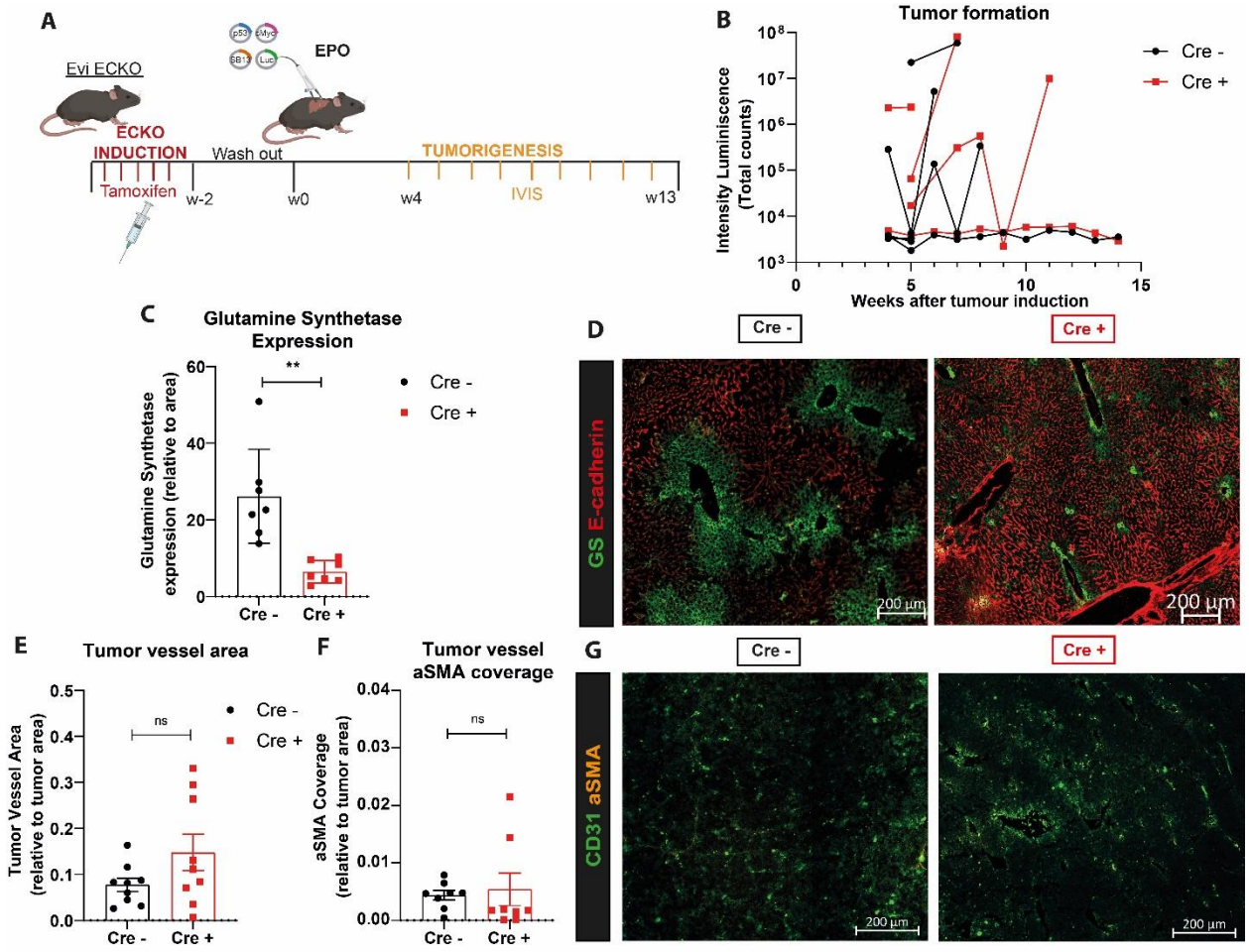

Figure 17. Local tumor formation is not affected by endothelial Evi/Wls deletion
A) Schematic representation of the experimental design showing tamoxifen injection for ECKO induction, followed by wash-out period, electroporation for tumor induction and IVIS measurement during tumorigenesis at indicated timepoints. **B**) Intensity of luminescence measured via IVIS to determine tumor growth overtime in Cre – and Cre + mice from Evi/Wls-iECKO (Cre-, n=3; Cre +, n=3). **C**) Quantification of Glutamine Synthetase immunofluorescence staining in livers extracted from Evi/Wls-iECKO, Cre – and Cre + mice. **D**) Representative images of Glutamine Synthetase immunofluorescence staining as quantified in C, scale bar 200µm. **E**) Quantification of CD31 immunofluorescence staining as vessel area relative to tumor area in percentage in livers extracted from Evi/Wls-iECKO, Cre – and Cre + mice. **F**) Quantification of aSMA immunofluorescence within CD31 staining as tumor vessel coverage relative to tumor area livers extracted from Evi/Wls-iECKO, Cre – and Cre + mice. **G**) Representative images of immunofluorescence staining of CD31 and aSMA as quantified in E and F, scale bar 200µm. Data are represented as mean ± s.e.m. (B), mean ± s.d. (C, E, F) and p-value by unpaired t-test (C, E, F), each point represents one liver section analyzed; ns, not significant; ** p<0.01.

3.2.7. Endothelial Evi deletion accelerates tumor formation in a multifocal HCC murine model

Tumor induction after Evi/Wls endothelial deletion was addressed in the multifocal iAST model obtained by crossing the iAST mouse line together the single Evi/Wls-iECKO. First, this mouse line was characterized

and endothelial Evi/Wls deletion was verified (**Fig. 18B**). As expected, the loss of Evi/Wls expression did not affect *Rspo3* expression (**Fig. 18A**), yet induced a decrease in GS expression (**Fig. 18C, D**). Tumor nodules also developed 5 weeks after AdCre injection (**Fig. 18E**). For the survival experiment, Evi ECKO was induced via tamoxifen injection, wash-out for 2 weeks and tumor formation was induced via AdCre injection, and mice were kept until they reached the endpoint criteria (**Fig. 19A**). The genetic recombination efficacy was evaluated based on the GS expression (**Fig. 18C**). Interestingly, Cre + mice showed attenuated tumor growth (**Fig. 19B**). The systemic liver damage markers, AST and ALT, recapitulated this phenotype by showing reduced levels in the Cre + group (**Fig. 19C, D**). Furthermore, the reduction of tumor vessel area per nodule was observed (**Fig. 19E, G**) recapitulating the phenotype observed in the double ECKO (**Fig. 16C, D**) and in the proliferating vasculature upon single Evi/Wls and Rspo3 ECKO (102, 113). Yet, this decreased tumor vessel area per nodule was not accompanied by significant changes in the aSMA vessel coverage (**Fig. 19 F, G**). Overall, these results suggested, that endothelial Wnt factors do not make a major contribution to sustain HCC initiation. However, endothelial-cell derived Wnt ligands contribute to the decreased tumor vessel area in an autocrine manner.

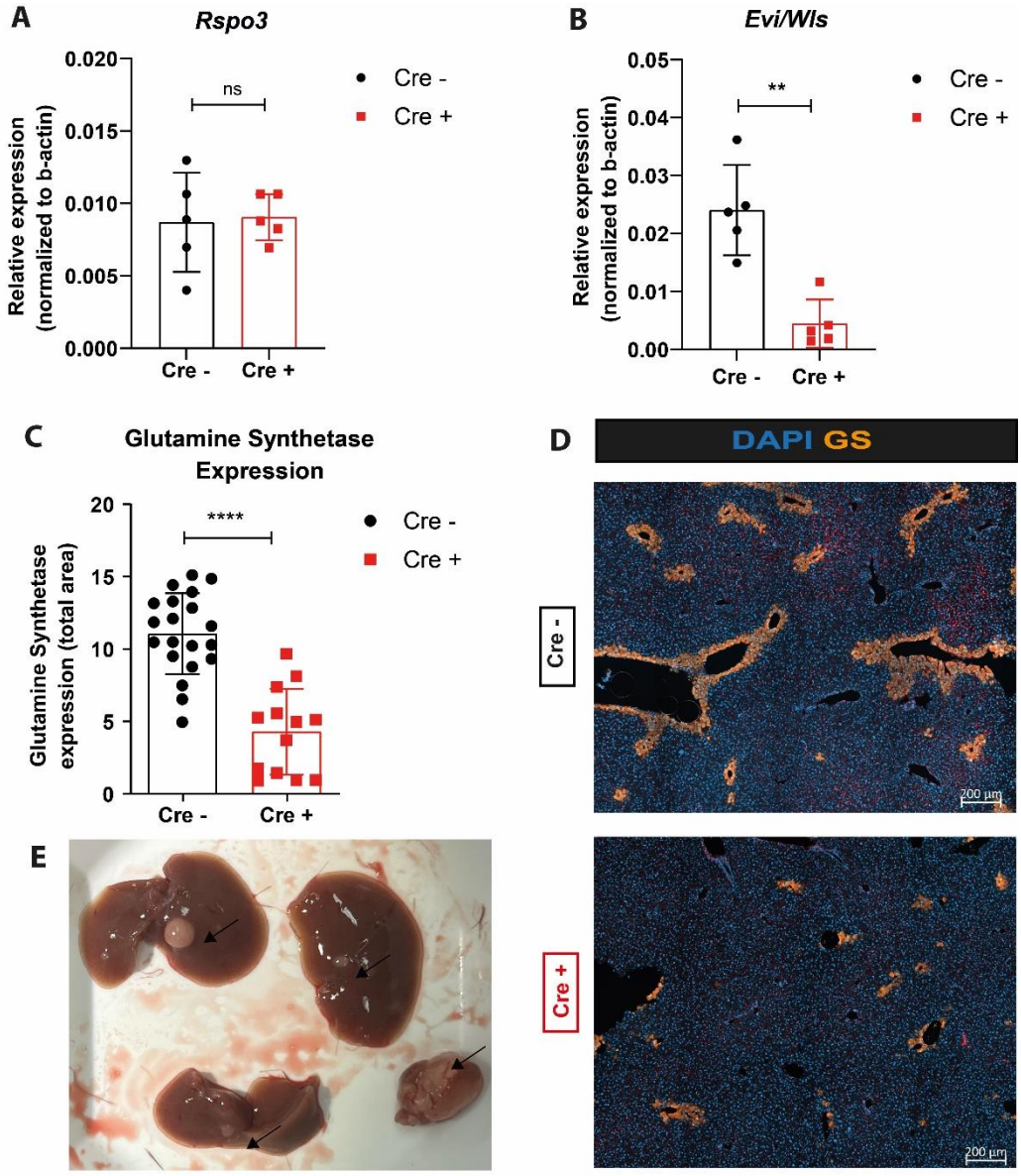

Figure 18. Characterization of Evi/Wls-iECKO-iAST mouse line

A) Relative gene expression of *Rspo3* in isolated tumor endothelial cells from Evi/Wls-iECKO-iAST, Cre – and Cre + mice. **B**) Relative gene expression of *Evi/Wls* in isolated tumor endothelial cells from Evi/Wls-iECKO-iAST, Cre – and Cre + mice. Each point represents one biological replicate. **C**) Quantification of Glutamine Synthetase immunofluorescence staining in livers extracted from Evi/Wls-iECKO iAST, Cre – and Cre + mice. Each point represents one tissue section. **D**) Representative images of Glutamine Synthetase immunofluorescence staining as quantified in C, scale bar 200µm. **E**) Representative images of a tumor bearing liver from the Evi/WlsiECKO-iAST mouse line, black arrows indicate nodules. Gene expression was normalized to b-actin (A, B). Data are represented as mean ± s.d. p-value by unpaired t-test; ns, not significant; ** p<0.01,**** p<0.0001.

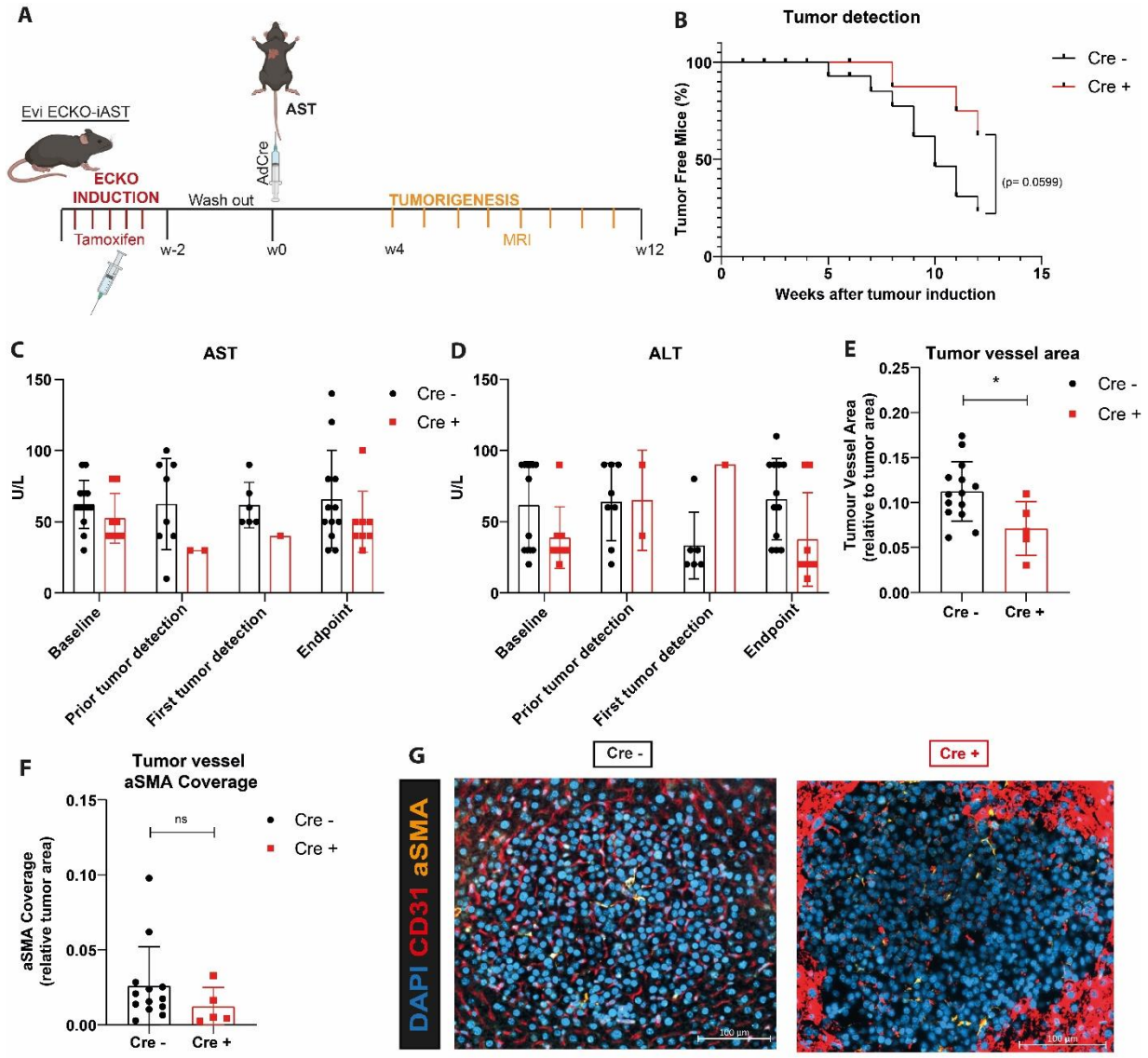

Figure 19. Deletion of endothelial Wnt ligand secretion prolongs survival in the GEM iAST model

A) Schematic representation of the experimental design showing tamoxifen injection for ECKO induction, followed by wash-out period, Ad-Cre injection for tumor induction and MRI measurement during tumorigenesis at indicated timepoints. **B**) Kaplan-Meier survival representing the percentage of tumor-free mice after tumor induction (Cre-, n=13; Cre +, n=8). **C**) Levels of the blood liver damage markers AST and ALT (U/L) at baseline, right before tumor detection, first time tumor was detected by MRI and at the endpoint. **D**) Quantification of CD31 immunofluorescence staining as vessel area relative to nodule area in percentage in livers extracted from Evi/Wls-iECKO-iAST, Cre – and Cre + mice. **E**) Quantification of aSMA immunofluorescence staining as tumor vessel coverage relative to tumor nodule area inside tumor nodules in livers extracted from Evi/Wls-iECKO-iAST, Cre – and Cre + mice. **F**) Representative images of immunofluorescence staining of CD31 and aSMA as quantified in G and H, scale bar 200μm. Each point represents one biological replicate (C-D) and one tumor nodule (E, F); data are represented as mean ± s.d. (C-D) and mean ± s.e.m. (E) p-value by Kaplan-Meier survival analysis (B) and unpaired t-test (C-D) and at each time point (E); ns, not significant; * p<0.05.

3.2.8. Endothelial Rspo3 deletion does not induce HCC formation in a local electroporation based murine model

Next, I investigated whether Rspo3 was responsible for the phenotype observed in the HCC models from the double Wnt ECKO: accelerated tumor formation that does not translate in a difference in survival (**Fig. 14, 16**). Furthermore, I determined whether the autocrine phenotype observed above (**Fig. 12, 15, 19**) was independent of endothelial Rspo3. To tackle these questions, HCC was induced after a single endothelial Rspo3 deletion. Tumors were induced with the focal electroporation model with the same experimental scheme as before (**Fig. 20A**). Rspo3 ECKO deletion was validated based on differential GS expression (**Fig. 20C, D**). Tumor initiation occurred earlier in the case of the Cre + group as shown by the higher luminescence intensity at the initial time of tumor measurement (**Fig. 20B**). No significant changes were detected in the tumor growth rate shown as bioluminescence intensity overtime (**Fig. 20B**). Analysis of the tumor vasculature revealed similar changes as in the double ECKO (**Fig.12**) but to a lesser extent. Decreased tumor vessel area (**Fig.20 E, G**) and increased tumor vessel aSMA coverage were observed (**Fig.20 F, G**). This indicates that the differences in tumor initiation were driven mainly by endothelial secretion of Rspo3 and the changes in the tumor vasculature are dependent endothelial Wnt secretion, either Evi/Wls derived or Rspo3.

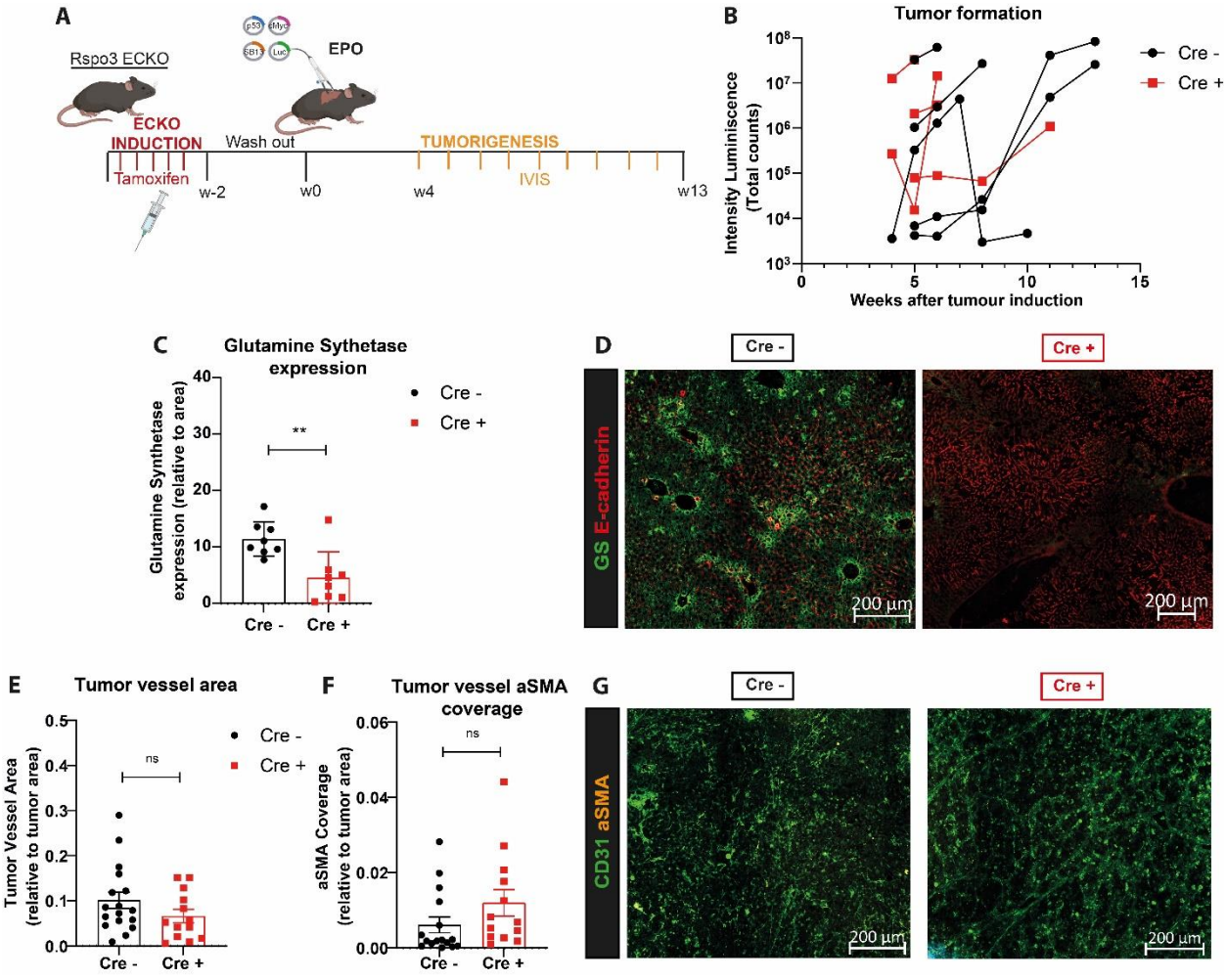

Figure 20. Deletion of endothelial Rspo3 enhances tumor formation in a focal electroporation HCC model
A) Schematic representation of the experimental design showing tamoxifen injection for ECKO induction, followed by wash-out period, electroporation for tumor induction and IVIS measurement during tumorigenesis at indicated timepoints. **B**) Intensity of luminescence measured via IVIS to determine tumor growth overtime in Cre – and Cre + mice from Rspo3-iECKO (Cre-, n=5; Cre +, n=4). **C**) Quantification of Glutamine synthetase immunofluorescence staining in livers extracted from Rspo3-iECKO, Cre – and Cre + mice. **D**) Representative images of Glutamine synthetase immunofluorescence staining as quantified in C, scale bar 200µm. **E**) Quantification of CD31 immunofluorescence staining as vessel area relative to tumor area in percentage in livers extracted from Rspo3-iECKO, Cre – and Cre + mice. **F**) Quantification of aSMA immunofluorescence within CD31 staining as tumor vessel coverage relative to tumor area livers extracted from Rspo3-iECKO, Cre – and Cre + mice. **G**) Representative images of immunofluorescence staining of CD31 and aSMA as quantified in E and F, scale bar 200µm. Data are represented as mean ± s.e.m. (B), mean ± s.d. (C, E, F) and p-value by unpaired t-test (C, D, F), each point represents one liver section analyzed; ns, not significant; ** p<0.01.

3.2.9. Endothelial Rspo3 deletion results in vessel maturation in a multifocal HCC murine model

To corroborate the role of angiocrine and autocrine Rspo3 in HCC formation, iAST tumors were induced after the endothelial deletion of Rspo3. First, the Rspo3-iECKO and iAST mouse lines were crossed and the new Rspo3-iECKO-iAST mouse line was characterized. The genetic recombination efficacy was confirmed in terms of Rspo3 deletion (**Fig. 21A)**, corresponding effect in Evi/Wls (**Fig. 21B**) and GS expression (**Fig. 21C, D**) and formation of tumor nodules (**Fig. 21E**). To address the contribution of Rspo3 in HCC initiation and survival, the iAST model was induced and mice were kept until they reached the endpoint criteria (**Fig. 22A**). Endothelial deletion was validated according to GS expression (**Fig. 21C**). Rspo3 deletion alone did not show a difference in tumor initiation (**Fig. 22B**). Similarly, the systemic liver damage markers AST and ALT were not altered between both groups (**Fig. 22C, D**). Cre + mice showed increased tumor vessel area per nodule (**Fig. 22E, F**) without changes in aSMA coverage (**Fig. 22E, G**).

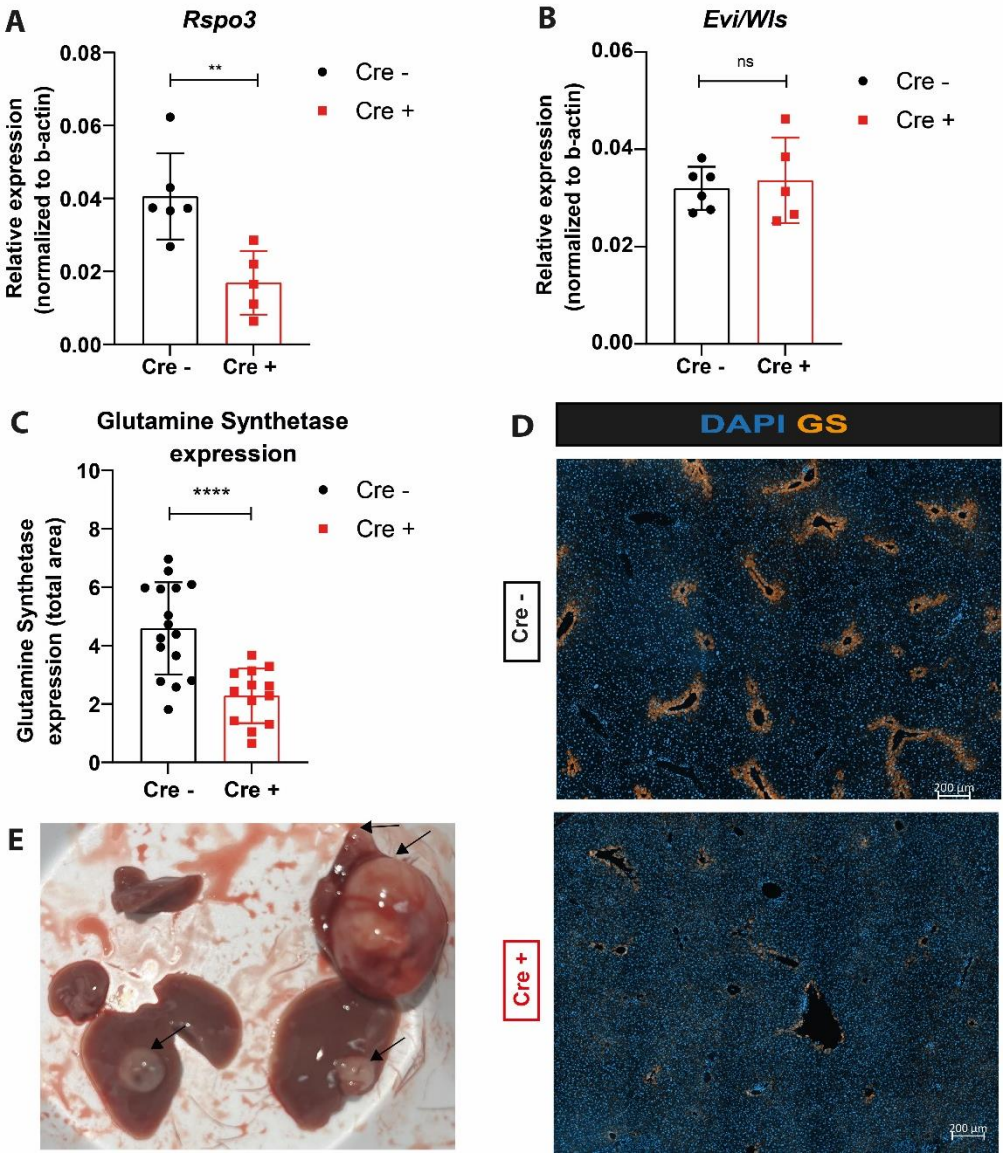

Figure 21. Characterization of Rspo3-iECKO-iAST mouse line

A) Relative gene expression of Rspo3 in isolated tumor endothelial cells from Rspo3-iECKO-iAST, Cre – and Cre + mice. **B**) Relative gene expression of Evi/Wls in isolated tumor endothelial cells from Rspo3-iECKO-iAST, Cre – and Cre + mice. Each point represents one biological replicate. **C**) Quantification of Glutamine Synthetase immunofluorescence staining in livers extracted from Rspo3-iECKO-iAST, Cre – and Cre + mice. Each point represents one tissue section. **D**) Representative images of Glutamine Synthetase immunofluorescence staining as quantified in C, scale bar 200µm. **E**) Representative images of a tumor bearing liver from the Rspo3-iECKO-iAST mouse line, black arrows indicate nodules. Gene expression was normalized to b-actin (A, B). Data are represented as mean ± s.d. p-value by unpaired t-test; ns, not significant; ** p<0.01,**** p<0.0001.

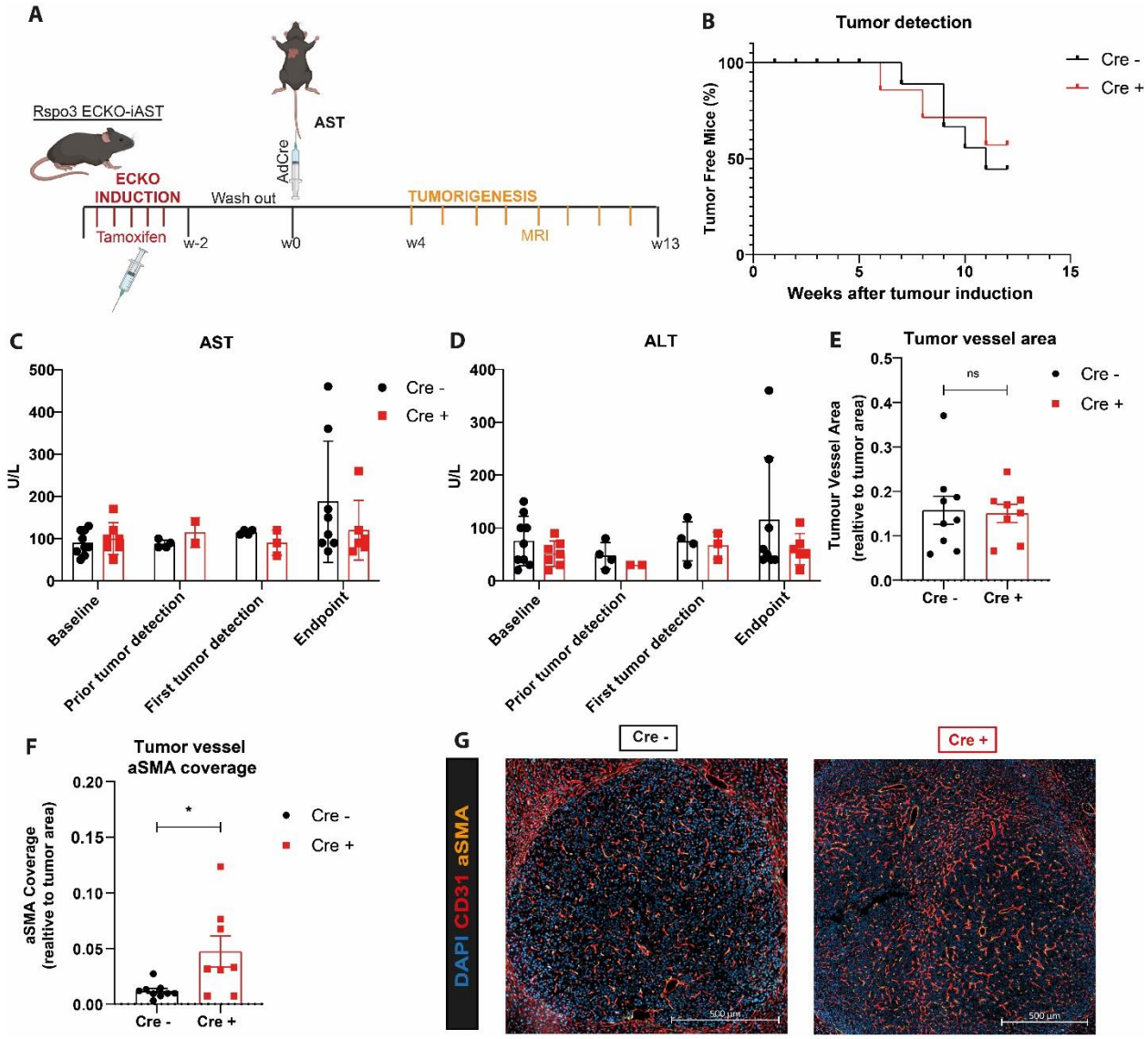

Figure 22. Deletion of endothelial Wnt enhancer Rspo3 in the GEM iAST induces vessel maturation
A) Schematic representation of the experimental design showing tamoxifen injection for ECKO induction, followed by wash-out period, Ad-Cre injection for tumor induction and MRI measurement during tumorigenesis at indicated timepoints. **B**) Kaplan-Meier survival representing the percentage of tumor-free mice after tumor induction. (Cre-, n=8; Cre +, n=8). **C**) Levels of the blood liver damage markers AST and ALT (U/L) at baseline, right before tumor detection, first time tumor was detected by MRI and at the endpoint. **D**) Quantification of CD31 immunofluorescence staining as vessel area relative to nodule area in percentage in livers extracted from Rspo3-iECKO-iAST, Cre – and Cre + mice. **E**) Quantification of aSMA immunofluorescence staining as tumor vessel coverage relative to tumor nodule area inside tumor nodules in livers extracted from Rspo3-iECKO-iAST, Cre – and Cre + mice. **I**) Representative images of immunofluorescence staining of CD31 and aSMA as quantified in G and H, scale bar 500µm. Each point represents one biological replicate (C-D) and one tumor nodule (E, F); data are represented as mean ± s.d. (C-D) and mean ± s.e.m. (E) p-value by Kaplan-Meier survival analysis (B) and unpaired t-test (C-D) and at each time point (E); ns, not significant; * p<0.05.

3.2.10. Wnt signaling is decreased in human liver tumors

I interrogated whether the decrease endothelial Wnt expression of Rspo3 and Evi/Wls reported in murine HCC models was also found in human HCC. First, I investigated their expression in publicly available datasets of human HCC tumors compared to healthy tissues. In the GEPIA2 database, expression of Rspo3 was significantly decreased in liver tumor compared to healthy livers, whereas Evi/Wls remained unchanged. Next, I questioned whether this difference, especially in the case of Rspo3, may translate into differences in HCC survival. The TCGA data showed no correlation between the whole liver expression of both candidates and overall survival in liver cancer. However, the contribution of Wnt signaling in HCC initiation cannot be excluded from these data since the analysis was performed from whole liver expression and other cell types may contribute to the Wnt signaling pathway. Based on these human data and the murine data described, I hypothesized that Rspo3 may be the main regulator of the angiocrine Wnt effect in HCC. To study Rspo3 expression specifically in endothelial cells, I established the view RNA system *in situ* hybridization (ISH) expression of Rspo3 and CD34, as a marker of endothelial cells (**Fig. 23D**). This was complemented by immunofluorescence staining of DAPI and GS. GS was used as a marker of the central vein in healthy livers, where Rspo3 is specifically expressed (22). Besides, it was used as a negative marker of proliferative liver tumors (as the ones used in this study). **Figure 23** shows a representative image of a non-tumor liver, in which Rspo3 is highly expressed around the central vein which is indicated by the coexpression of CD34 and Rspo3 (**Fig. 23D**). On the contrary, in a human liver tumor sample from cirrhosis (**Fig. 24**) etiology, CD34 expression barely colocalized with Rspo3. This suggested that Rspo3 expression in endothelial cells was decreased in HCC human tumors.

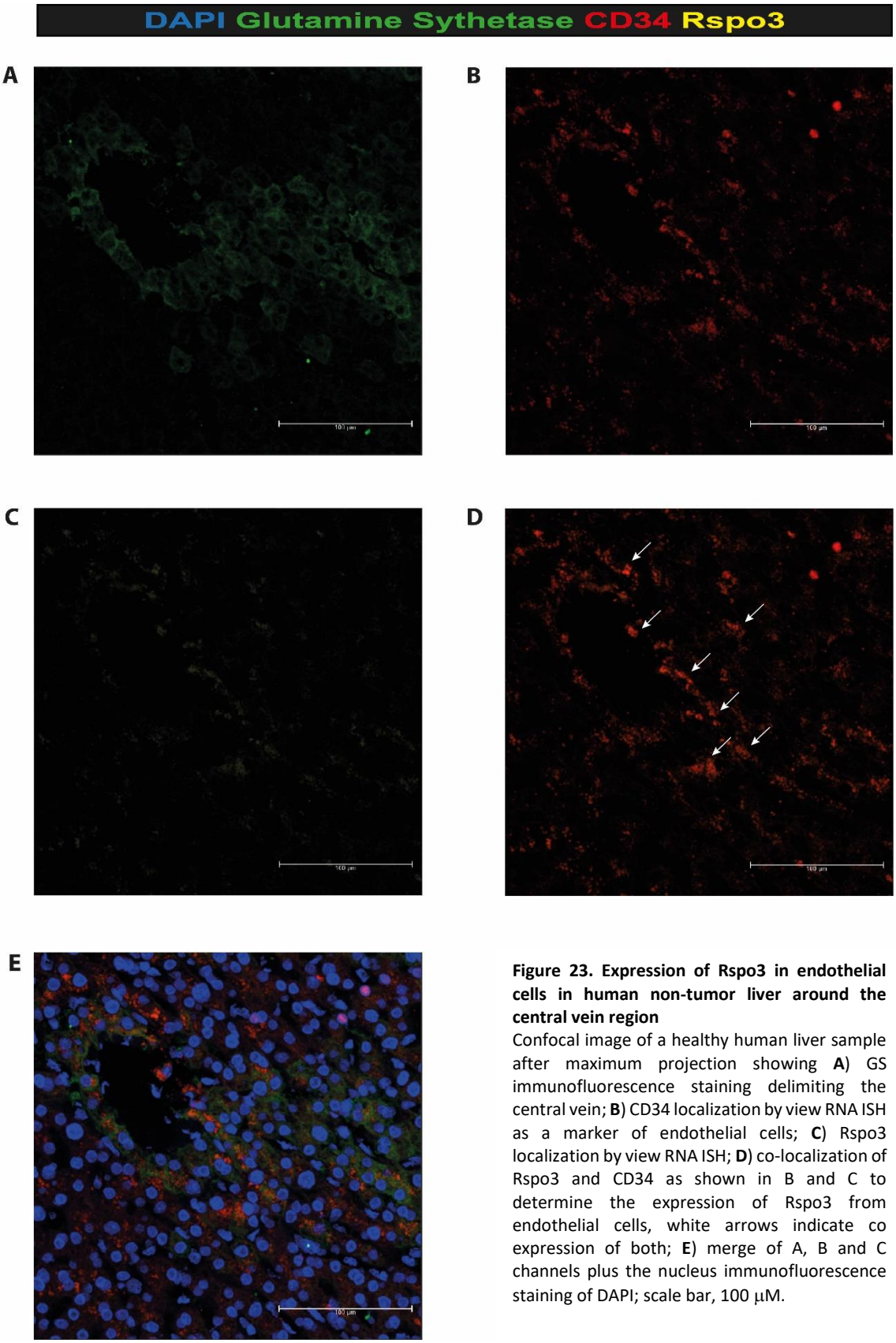

Figure 23. Expression of Rspo3 in endothelial cells in human non-tumor liver around the central vein region

Confocal image of a healthy human liver sample after maximum projection showing **A**) GS immunofluorescence staining delimiting the central vein; **B**) CD34 localization by view RNA ISH as a marker of endothelial cells; **C**) Rspo3 localization by view RNA ISH; **D**) co-localization of Rspo3 and CD34 as shown in B and C to determine the expression of Rspo3 from endothelial cells, white arrows indicate co expression of both; **E**) merge of A, B and C channels plus the nucleus immunofluorescence staining of DAPI; scale bar, 100 μM.

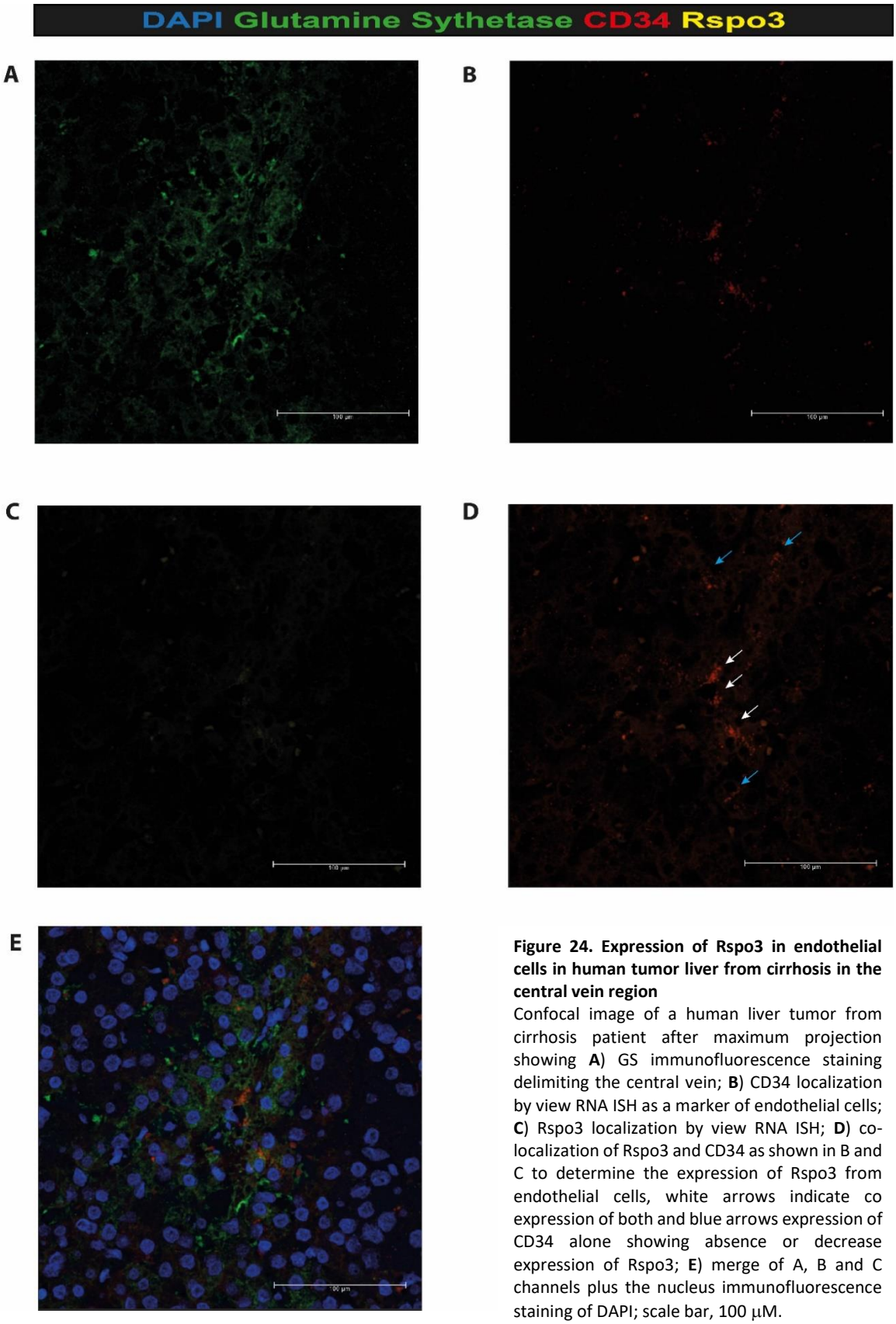

Figure 24. Expression of Rspo3 in endothelial cells in human tumor liver from cirrhosis in the central vein region

Confocal image of a human liver tumor from cirrhosis patient after maximum projection showing **A**) GS immunofluorescence staining delimiting the central vein; **B**) CD34 localization by view RNA ISH as a marker of endothelial cells; **C**) Rspo3 localization by view RNA ISH; **D**) co-localization of Rspo3 and CD34 as shown in B and C to determine the expression of Rspo3 from endothelial cells, white arrows indicate co expression of both and blue arrows expression of CD34 alone showing absence or decrease expression of Rspo3; **E**) merge of A, B and C channels plus the nucleus immunofluorescence staining of DAPI; scale bar, 100 μM.

Overall, the data suggest that the HCC TME is characterized by decreased endothelial Wnt signaling. This Wnt-deficient microenvironment induces a more tumorigenic environment, where the vasculature is decreased but more mature. Theoretically, this tumor vessel normalization is associated with reduced tumorigenesis, especially therapeutically. However, autocrine effects of Wnt have previously been described to induce vessel regression in physiological and pathological angiogenesis (102, 113) without affecting tumor growth. Therefore, I hypothesized that in HCC, the Wnt-dependent endothelial secretome may induce two independent phenotypes: angiocrine and autocrine. I focused on the role of angiocrine Wnt during HCC initiation, investigating the interaction between liver endothelial cells and both, healthy and tumor cells.

3.3. Crosstalk between tumor cells and liver endothelial cells sustain tumorigenesis

3.3.1. Tumor-derived factors modulate the expression of LSEC landmark genes

I focused, first, on the interaction between tumor cells and (tumor) endothelial cells and questioned whether the decrease in Wnt ligand secretion in tumor ECs is induced by tumor cells. To address this question, freshly isolated liver ECs were treated for 48 h with a conditioned medium from a murine HCC cell line. Fresh serum-free medium was used as a control (**Fig. 25A**). Expression of landmark endothelial zonation and capillarization genes, and members of the Wnt signaling pathway were analyzed. *Rspo3* and *Evi/Wls* expression were decreased after treatment (**Fig. 25B, C**), resembling the previous findings (**Fig. 11**). The expression of the CV Wnt ligands, *Wnt2* and *Wnt9b*, was also significantly decreased (**Fig. 25D, E**), while, the portal vein marker *Dll4* was increased (**Fig. 25G**). On the contrary, the portal vein marker *Efnb2* (**Fig. 25H**) and the non-zonated *Wnt4* ligand was unchanged (**Fig. 25F**). Other LSEC, arterial and sinusoidal markers were further analyzed. *Gata4* (**Fig. 25I**), *Ly6a*, *Aplnr* and *Cd9* (**Fig. 25J, K, M**) remained unchanged, while *Itga6*, *Lyve1* and *Cdh5* (**Fig. 25L, N, O)** were upregulated. Overall, these data suggest that tumor-derived factors induced transcriptomic changes in liver ECs, mostly in Wnt signaling, that recapitulate the Wnt profile previously described in TEC in HCC (**Fig. 11**). These changes were, in principle, not dependent on liver metabolic zonation, since central vein markers were decreased, while portal markers were either unchanged or also increased. The increase of *Dll4*, *Aplnr* and *Cdh5* may be explained by the capillarization that LSECs undergo during hepatocarcinogenesis (128).

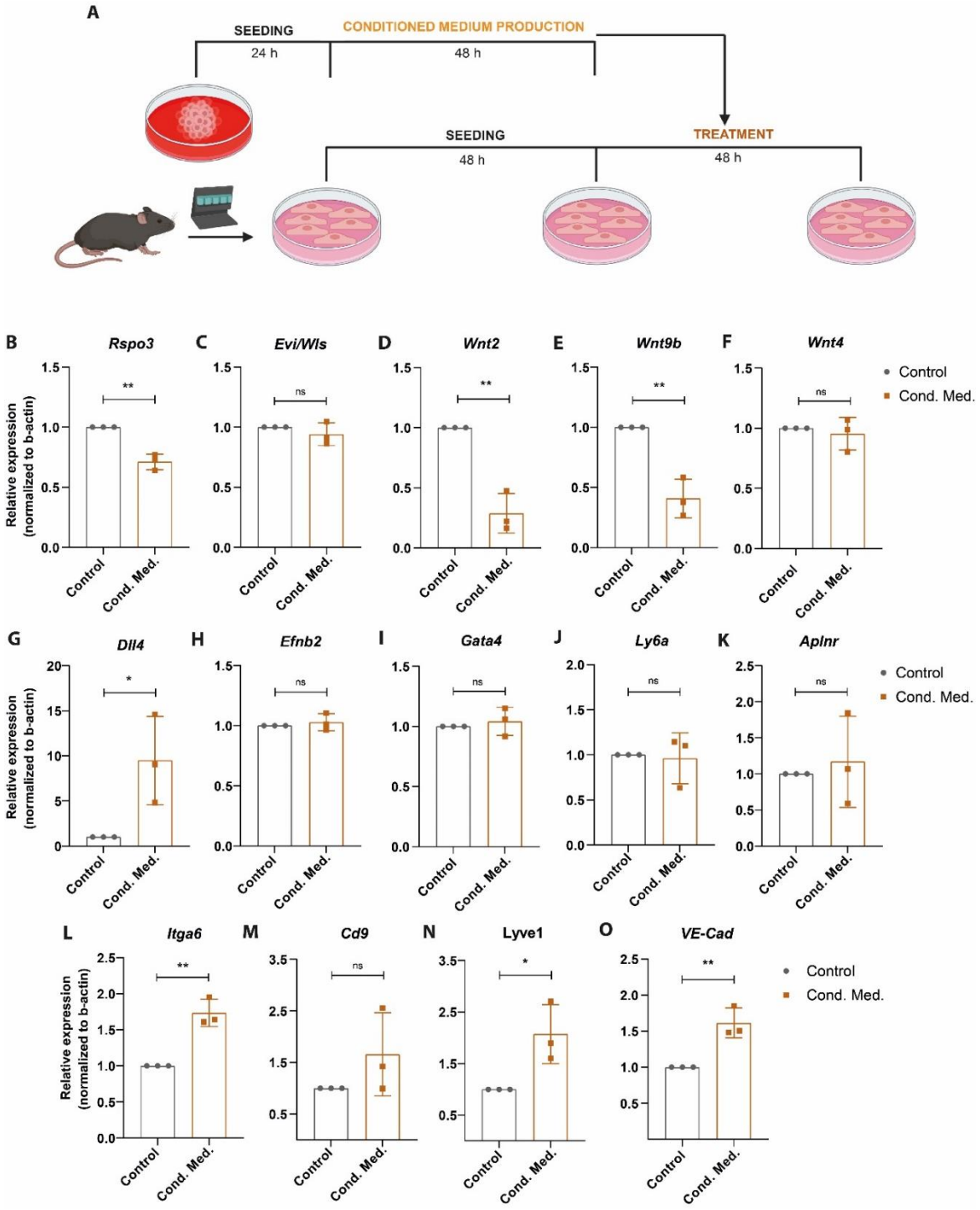

Figure 25. Tumor-derived factors induce transcriptomic changes in healthy liver ECs

A) Schematic representation of the experimental design showing isolation of primary liver ECs from wild type (Wt) mice, seeding for 48 hours and posterior treatment with conditioned medium produced from the murine HCC cell line, Hepa1.6. Relative gene expression of **B**) the Wnt candidate genes *Rspo3* and **C**) *Evi/Wls*; **D**) central vein Wnt ligands *Wnt2* and **E**) *Wnt9*b; **F**) non zonated Wnt ligand, *Wnt4*; **G**) portal vein markers *Dll4* and **H**) *Efnb2*; **I**) LSEC markers *Gata4*; **J**) arterial markers *Ly6a*, **K**) *Aplnr*, **L**) *Itga6*; **M**) *Cd9*; **N**) sinusoid marker LSEC, *Lyve1*, and **O**) *VE-Cad* in primary isolated liver ECs treated for 48 hours with conditioned medium or fresh serum-free, as control, plus complete medium (60/40). Gene expression was normalized to b-actin (B-H) and relative to each control. Each point represents one biological replicate; data are represented as mean ± s.d. p-value by unpaired t-test; ns, not significant; * p<0.05,** p<0.01.

3.3.2. In vitro deletion of Rspo3 enhances proliferation in the murine HCC cell line, Hepa1.6

Tumor-derived factors decreased Wnt signaling in liver ECs. Consequently, I investigated whether a reduced Rspo3 expression could enhance proliferation in HCC tumor cells. To corroborate the role of Rspo3 in regulating tumor growth, HCC tumor cells were treated for 48 h with conditioned medium from freshly isolated liver ECs from Rspo3 ECKO mice which were further treated with hydroxytamoxifen to induce Rspo3 deletion (**Fig. 26A**). Endothelial Rspo3 deletion was validated by qPCR (**Fig. 26B**) and cell cycle distribution was assessed by Edu and FxCycle incorporation. Treatment with conditioned medium from liver ECs with diminished Rspo3 secretion induced an increase in cells in S phase (**Fig. 26C**). This suggests that loss of Rspo3 secretion from ECs promotes tumor cells to undergo cell cycle division in an angiocrine manner.

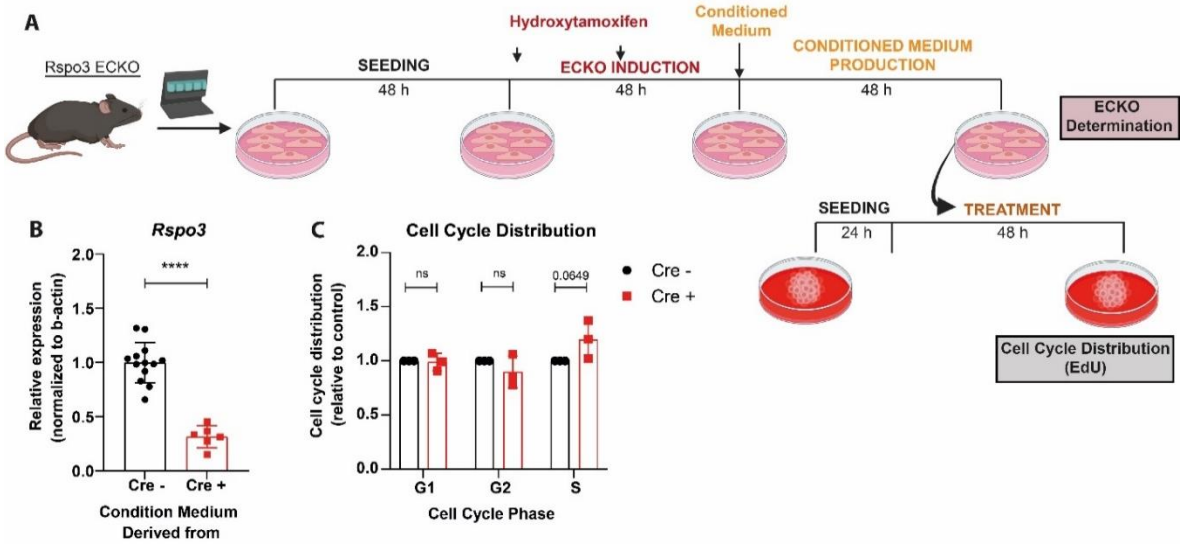

Figure 26. Endothelial secretome after Rspo3 deletion induces tumor cells to enter cell cycle division
A) Schematic representation of the experimental design showing isolation of primary liver ECs from Rspo3 ECKO mice (Cre – and Cre +), seeding for 48 hours, Rspo3 deletion was induced using hydroxytamoxifen *in vitro*, production of conditioned medium which was later on used to treat the murine HCC cell line, Hepa1.6. **B**) Relative gene expression of Rspo3 in primary isolated liver ECs after hydroxytamoxifen treatment for ECKO induction; each point represents one biological replicate. **C**) Cell cycle distribution of Hepa1.6 after 48 hours of treatment with condition medium derived from Cre – and Cre + mice, relative to Cre – as a control; each point represents one replicate from different passages. Gene expression was normalized to b-actin (B). Each point represents one biological replicate; data are represented as mean ± s.d. p-value by unpaired t-test; ns, not significant;**** p<0.0001.

3.3.3. Treatment of the murine HCC cell line, Hepa1.6, with recombinant Rspo3 protein reduces proliferation

I hypothesized whether Rspo3 have a role as an antitumorigenic agent since reduced secretion of Rspo3 induced cell proliferation in tumor cells. To address this question, Hepa1.6 was treated with different concentrations of recombinant Rspo3 protein (0.005, 0.025, 1, 10 μg/mL) 24h after seeding (**Fig. 27A**). Proliferation was assessed by EdU and Fx-Cycle incorporation after 48h of treatment. EdU incorporation showed a dose-dependent decrease, but it was statistical significance at the highest concentration (**Fig. 27B**). At this concentration, cells in the S phase decreased at the expense of an increase in the G1 phase (**Fig. 27C**). In conclusion, Rspo3 supplementation reduced tumor cell proliferation.

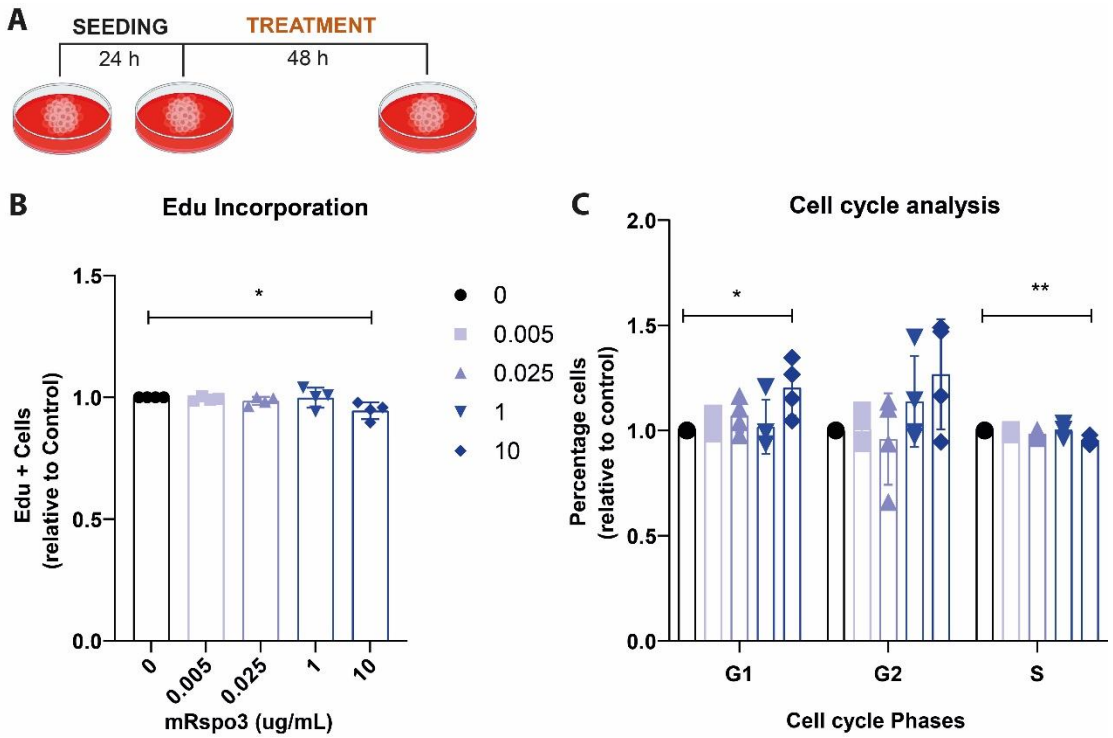

Figure 27. Treatment with murine recombinant Rspo3 protein reduces proliferation in Hepa1.6
A) Schematic representation of the experimental design showing treatment with murine recombinant protein Rspo3 for 48 hours after seeding. **B**) Determination of the amount of proliferating cells as EdU incorporation; and **C**) cell cycle distribution as Fx-Cycle and EdU incorporation of Hepa1.6 after 48 hours of treatment with different concentrations of murine Rspo3 recombinant protein relative to vehicle treated sample; each point represents one replicate from different passages. Each point represents one biological replicate; data are represented as mean ± s.d. p-value by unpaired t-test; ns, not significant; * p<0.05, ** p<0.01.

3.3.4. Treatment of tumor-derived organoids with recombinant Rspo3 protein reduces proliferation

To validate the effect of Rspo3 reducing proliferation in a more complex *in vitro* system, I took advantage of the tumor-derived organoids established from both HCC models. Tumor-derived organoids were treated after split with recombinant Rspo3 protein (1, 10 μg/mL) for 72 h (**Fig. 28A**) and proliferation was assessed by EdU incorporation. In both cases, a decrease in cell proliferation was observed, reaching statistical significance at the highest concentration. These data validate the previous finding in Hepa1.6 cell line indicating Rspo3 had an antiproliferative effect.

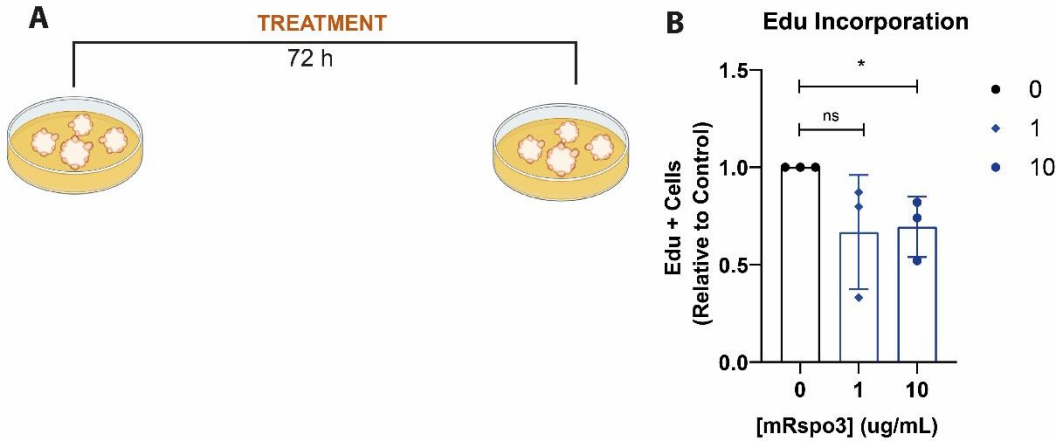

Figure 28. Treatment with murine recombinant Rspo3 protein reduces proliferation in tumor-derived organoids
A) Schematic representation of the experimental design showing treatment with murine recombinant protein Rspo3 for 72 hours right after seeding. **B**) Determination of the amount of proliferating cells as EdU incorporation of cells from tumor-derived organoids after 48 hours of treatment with different concentrations of murine Rspo3 recombinant protein relative to vehicle treated sample; each point represents one replicate from different passages. Each point represents one biological replicate; data are represented as mean ± s.d. p-value by unpaired t-test; ns, not significant; * $p<0.05$.

4. DISCUSSION

4.1. Suitable model to study HCC

Liver cancer is a major health issue. HCC is the most common subtype and its incidence has been increasing during the last decades (31-33). However, the available treatments are limited due to the lack of HCC models that fully recapitulate hepatocarcinogenesis, while maintaining the TME. This impedes successful and more efficient drug discovery processes. The most commonly used models for HCC research are cell line derived (81%), environmentally induced (28%), GEM (25%), and PDX (3%) (129). The fact that the most commonly used model is based on the injection of an aggressive subclonal population may explain the low rate of success of the HCC therapeutic landscape. Recently, tumor fragments or organoids have been used to advance these engraftment models. These partially overcome the limitations of clonality by introducing a much more heterogeneous population, which recapitulates the complexity of the tumor (85). However, this type of experimental approach still has two main limitations. In most cases, when the parental tumor is human, the recipient has to be immunocompromised or even immunodeficient. (85-87). Therefore, the use of these models hinders not only the contribution of the immune TME in HCC initiation and progression, but also the establishment of any immunotherapy treatment. This is of utmost importance, especially in light of the recent IMBRave clinical trial. For the first time, an immunotherapy treatment (anti-PD-L1) in combination with an antiangiogenic (anti-VEGF) offers an improved treatment compared to the previous standard care of treatment (52). Another major limitation of these models is their inability to recapitulate the initial stages of hepatocarcinogenesis. This is critical in HCC that arises from chronic liver damage. However, these models can serve as useful tools to specifically investigate colonization or metastatic dissemination, or develop avatar mice for co-clinical trials (129).

An alternative to address these issues is to use environmentally induced models. These models are highly suitable to address specific experimental questions as they have the potential to recapitulate the initial stages of liver transformation. However, it has to be considered that many commonly use carcinogens, such as DEN or CCl_4, have the limitation that tumors tend to develop preferably in certain regions of the liver metabolic zonation axis. This is also the case in HTVI, a tumor model unique for liver. In HTVI and DEN, hepatocytes located around the central vein region are prone to tumor transformation (85-87). Therefore, the resulting TME may not resemble the one developing from chronic injury, where most of

the liver metabolic zonation axis is altered in a more unbiased way. Furthermore, viruses are considered as a very frequent carcinogen in HCC, although there are very few models which truthfully recapitulate the tumorigenesis process. The western diet is the most clinically relevant model within this subgroup. It accurately recapitulates liver transformation resulting from chronic liver damage into HCC, while maintaining the TME (40). Additionally, this model mimics HCC development from one of the most common etiologies today, NASH/NAFLD, which is expected to further increase in the upcoming years. However, it may not be very suitable for certain studies due to the relatively low incidence and extended time for tumor formation.

There is no doubt that every tumor model is a simplification of the very complex and long-term process of tumorigenesis. Therefore, selecting an appropriate mouse model should compromise between time, complexity and clinical relevance. The main aim of this study was to elucidate how the metabolically zonated angiocrine WNTs affect hepatocarcinogenesis. Using tumor models that preferentially develop in one particular region would have introduced a bias. In that case, it may be difficult to address whether central hepatocytes are predisposed to tumorigenesis due to the bias or a Wnt angiocrine gradient effect. Thus, it was essential to develop a model that fully recapitulates HCC initiation and progression in an unbiased manner. Additionally, since the study focused on the endothelial comparment of the TME, it was crucial to maintain the TME at large. Therefore, using a cell line-based model in an immunocompromised or immunodeficient mice was also ruled out. Another important parameter to consider for model selection is the feasibility including the time frame for tumor formation, which has to be suitable for the study.

It was required to choose models for this study that would fulfil all those criteria. For this reason, I established a local electroporation-based model by introducing some of the commonly mutated genes in HCC (31). This model also offers potential beyond the scope of this study. Here, p53 deletion and cMyc overexpression was employed as the tumor transformation element. In principle, any other transgene and oncogene could be electroporated to recapitulate any particular tumors, allowing to replicate almost any tumor entity. Furthermore, this model may be a suitable tool to study the importance of the endothelium and the high rate and lethality of intrahepatic metastasis induced by HCC. By performing partial hepatectomy in the electroporated left liver lobe bearing the tumor, it is possible to investigate the development of intrahepatic metastasis under certain circumstances such as adjuvant treatment after tumor resection. The available models to study such a process are very limited.

This model also has certain limitations. For instance, tumor induction via electroporation involves surgery, which is risky and a more time-consuming procedure in comparison to injections, the standard induction method for most of the cell line and environmentally induced models. Additionally, it requires precise handling; otherwise, it may result in a decreased yield in tumor induction. Furthermore, the model was described as undifferentiated HCC. This may be attributed to the presence of p53 deletion as one of the tumor-inducing factors. Its expression has been extensively reported in hepatocarcinogenesis. It induces liver inflammation and subsequent expansion of progenitor cells (130) and it is enhanced by increasing cholesterol esterification (131). Therefore, it is not surprising that mutant p53 was reported to be highly expressed in primary hepatic undifferentiated carcinomas (132). To improve this model, some points to consider are increasing tumor induction efficacy, inducing tumors with a more differentiated profile, and reducing ectopic tumor formation. To overcome these limitations, it was beneficial to have a complementary model, such as iAST, to substantiate the results.

Due to the complexity of *in vivo* models, *in vitro* models, and particularly cell lines, are often used as a reductionist system to perform complementary and mechanistic studies. However, this may be an oversimplification. Therefore, organoids have become state of the art, offering a middle ground between cell lines and *in vivo* models. On the one hand, they are relatively easy to handle and less time-consuming, similar to cell lines. On the other hand, tumor-derived organoids offer greater complexity and better resemble the tissue of origin than cell lines (60, 64). Therefore, tumor-derived organoids were established in this study to be used for drug screening and validation purposes. The use of cell lines was reduced to the minimum, only to what is strictly necessary for mechanistic studies.

4.2. Rspo3 as a potential therapeutic candidate for HCC

The role of angiocrine Wnt signaling has been extensively investigated in the liver, mediating the so-called liver metabolic zonation (1, 16, 17, 19, 22, 27, 133). However, in pathological conditions, the contribution of Wnt signaling is controversial, varying from pro- to anti-tumorigenic, depending on the tumor entity (71, 121, 122, 124). In HCC, where the liver metabolic zonation pattern is completely altered, its contribution has not been investigated. I aimed to examine the role of angiocrine Wnt signaling in HCC initiation and progression.

This study shows that endothelial Wnt secretion was reduced in the tumor endothelial cells compared to the healthy liver endothelium. Rspo3 was downregulated in both the murine models used in this study and human patient samples. Consistent with this, complete inhibition of endothelial Wnt secretion led to

earlier tumor formation, while single Rspo3 deletion resulted in minor changes. In the case of endothelial deletion of Wntless, there were no changes observed in the EPO and a slight delay in tumor formation in the iAST model. Overall, the data suggest that angiocrine Wnt secretion acted as a gatekeeper of the endothelial cell status. Endothelial Wnt deletion led to a protumorigenic microenvironment. In both models, deletion of endothelial Wnt secretion reduced tumor vessel area and increased maturation. Additionally, tumor-derived factors can induce a decrease in endothelial Wnt secretion in liver ECs, instructing the endothelium to sustain a protumorigenic TME. This indicated the existence of a feedback loop between the tumor cells and the (tumor) endothelial cells, and vice versa, aiming to reduce Wnt secretion (**Fig. 29**).

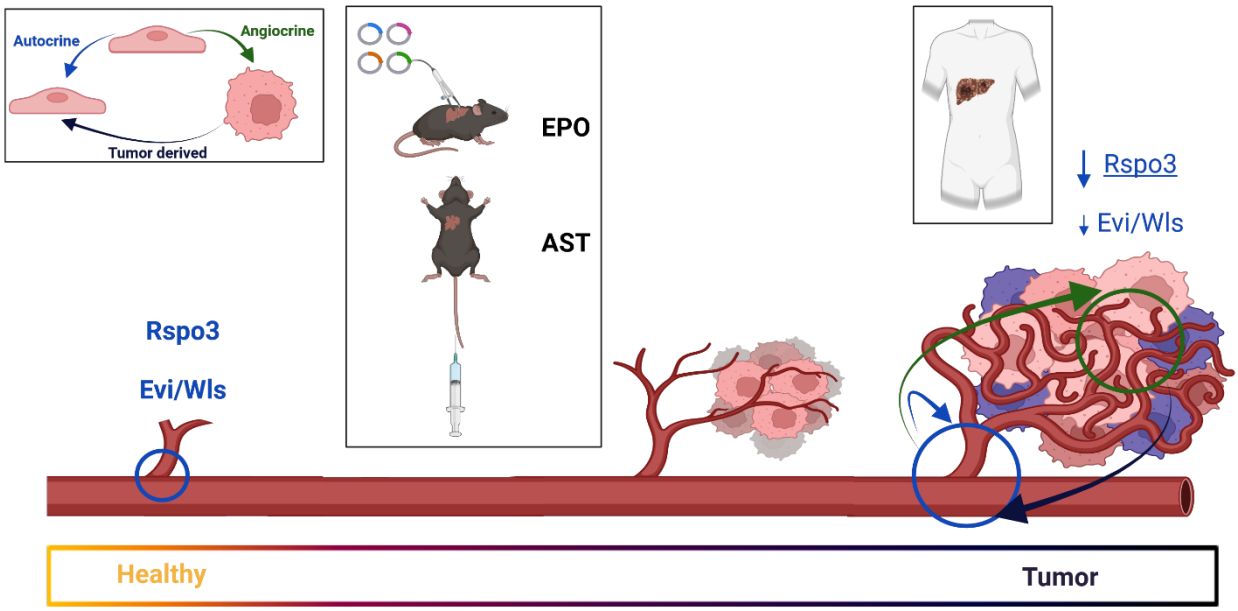

Figure 29. Proposed model
An *in vivo* murine model was established to induce HCC in a non-zonated dependent manner and recapitulate hepatocarcinogenesis: EPO. This was complemented with a multifocal HCC model: iAST. Tumor-derived organoids were established from both *in vivo* models. The expression of *Rspo3* and *Evi/Wls*, which are the Wnt candidate genes for this study, were decreased in liver tumor endothelial cells compared to healthy endothelium. In the case, of RSPO3 this decreased was further found in human liver tumor samples. As a result, deletion of endothelial Wnt secretion, mainly Rspo3 alone or combined with Evi/Wls, led to earlier tumor formation, and vessel regression and maturation. Additionally, tumor-derived factors induced decrease in *Rspo3* and *Evi/Wls* expression, indicating the existence of a positive feedback loop of low Wnt secretion between tumor and tumor endothelial cells. Preliminary data suggested Rspo3 may have a potential antitumorigenic effect.

This is consistent with the idea that the stroma is responsible for Wnt secretion. In the case of the healthy intestine, Wnt supplementation is necessary to maintain intestinal homeostasis (134). Likewise, in the context of tumors, myofibroblasts induce Wnt activation to sustain stemness properties in CSCs (122). In

lung adenocarcinoma, a similar subpopulation of tumor cells is sustained by a niche subpopulation that secretes Wnt ligands and enhancers (121). In lung metastasis, Wnt secretion from the TME especially from the endothelium, have an antitumorigenic effect inducing dormancy and preventing metastatic outgrowth in melanoma and breast cancer (135, 136). The specific Wnt ligand or enhancer that maintains a pro tumorigenic microenvironment is organ dependent. For example, Rspo2 has been described as the ligand in pancreatic cancer (137), which is barely detected in the case of liver (133).

In general, liver cancer cells exhibit upregulation of Wnt genes (30). However, the loss of Znrf3 predisposes to HCC by impairing liver regeneration (138). Its deletion induces HCC formation, and there is an inverse correlation between metabolism and proliferation (139). Wnt2 expression was also reported to decrease in severe alcohol-associated hepatitis, while other members of the Wnt signaling pathway were upregulated (140). This suggests that a specific Wnt secretion pattern could serve as an indicator of a protumorigenic tumor microenvironment. In addition, I reported that tumor-derived factors caused a decrease expression of *Wnt2* and *Wnt9b* in endothelial cells, while others, such as *Wnt4* or *Dll4*, remained unchanged or even increased.

The initial changes in tumor initiation did not result in differences in survival, and no other systemic changes were observed. Therefore, it is reasonable to hypothesize that changes in endothelial Wnt secretion are responsible for initiating tumor transformation rather than its progression. To address this question more in depth, endothelial Wnt secretion should be manipulated therapeutically after tumor induction. Given that angiocrine Wnts regulate liver metabolic zonation, it is reasonable to assume that they would play a role mainly in the early stages of tumor initiation rather than in disease progression, when metabolic zonation is already significantly altered. It has been questioned whether HCC formation has a certain inclination to develop in a specific region within the liver metabolic zonation axis; for instance, regarding the proliferation capacity. Although, this is broadly expressed by hepatocytes, it is only the ploidy status that confers an advantage for proliferation after injury (141). Hyperpolyploid regions are described to be located in the central region, where they are more susceptible to the formation of pre-neoplastic lesions formation, as observed in a DEN model that is predisposed to developing tumors around this region (142).

The expression of GS, which is located in the central vein region, was significantly reduced after angiocrine Wnt deletion. GS is also a differential marker use to distinguish between the proliferative and the non-proliferative HCC subclass (31). However, its role in tumorigenesis is controversial. In HCC, tumors with β-catenin mutation (i.e. GS + tumors), it has a protective role due to ammonia clearance (143). On the

contrary, the expression of GS, regardless of its metabolic function, regulates the transition from metaphase to anaphase in liver and lung cancer cells (144).

At the autocrine level, it was described that decreased expression of both Rspo3 and Evi/Wls, both alone or in combination, reduced tumor vessel area and increased vessel coverage. This Wnt-dependent effect mediates vessel regression and leads to a more mature vasculature, as previously described in physiological angiogenesis and in subcutaneous lung and melanoma tumors (102, 113). This resemblance is quite notable, considering the uniqueness and versatility of the hepatic vasculature (6). It adapts to the environment to create a tumorigenic environment that promotes disease progression. Liver endothelial cells undergo a collective transcriptomic alteration similar to the process that occurs during fetal formation, which is mediated by PVLAP (145). During metastasis formation, hepatic endothelial cells regulate their adhesion molecules through Notch signaling, which has a protective role (146). Although the importance of the liver vasculature in HCC progression is well known, the endothelium was only recently utilized efficiently in a therapeutic manner. For decades, Sorafenib, a multikinase inhibitor with VEGFR as one of its downstream targets, was the standard care of treatment. The dual combination of anti-VEGF and anti-PD-L1 replaced the previous treatment after the IMBRave150 clinical trial (52). The exact mechanism of action is still under investigation, but it appears to rely on vessel normalization synergizing with improved antitumor immunity (54). Therefore, blocking of endothelial-derived Wnt signaling could be a therapeutic alternative, following the same principles as the Atezolizumab and Bevacizumab combination.

However, this interpretation may be a bit oversimplified. Firstly, the data indicated that the number of T cell infiltrations remained unchanged with differential Wnt expression in HCC. It is important to investigate whether cytotoxicity remains constant and whether the myeloid compartment is affected. Additionally, recent data has shown that Rspo3 supplementation induces a more active immune system in melanoma, resulting in decreased tumor growth (118). This suggests an antitumorigenic role of Rspo3. It also goes in line with the angiocrine effect seen in terms of tumor initiation. Likewise, the data indicated that tumor-derived factors induced the decreased Wnt expression that characterized tumor ECs. Similarly, Rspo1 supplementation was recently described in colorectal cancer to have anti tumorigenic role mediated by TGFβ signaling (124).

Based on the current knowledge and the data described here, I hypothesized that Rspo3 may have antitumorigenic properties. Treatment with recombinant Rspo3 resulted in decreased tumor cell

proliferation in a HCC murine cell line and tumor-derived organoids, indicating a potential therapeutic advantage. Further investigation is needed to assess the contribution of the other members of the TME and the systemic effects of this treatment.

The focus of this project was on the endothelium as the primary source of liver Wnt secretion and the tumor cells as the primary mediators of tumor initiation and progression. However, the contribution of other cell types in the TME (e.g. HSCs, fibroblasts or neutrophils) are affected by Wnt signaling and how they contribute to HCC progression remain elusive. Recently, two subpopulations of HSCs were described as having opposite tumorigenic potential. Quiescence HSCs have an antitumorigenic effect. However, they become protumorigenic once they express type I collagen (147). Secretion from tumor associated neutrophils (TANs) also sustains CSCs and promotes tumor progression (148). Therefore, it remains unclear how decreased endothelial Wnt secretion in the tumor context affects HSCs and TANs, and whether Rspo3 supplementation would reinforce an antitumorigenic HCC progression. Thus, it is recommended to conduct *in vivo* experiments to overexpress Rspo3 in either preventively (right after tumor induction) or therapeutically (once the tumor has formed).

The potential side effects of Rspo3 supplementation as a treatment for HCC extend beyond the close interaction within the tumor microenvironment. Indeed, Wnt signaling is broadly expressed throughout the liver (149) in both physiological and pathological conditions (95), and is also involved in maintaining stem cells and homeostasis in other organs, such as the intestine. Therefore, it is likely that the side effects are also considerable. Despite being highly mutated in many cancers, Wnt pathway inhibitors do not have a high success rate in clinics (91). An alternative may be to find a highly specific target and/or activator. For example, a very precise Wnt7 agonist was engineered to modulate brain vasculature in pathological conditions (114).

In summary, in this study, I established a focal electroporation-based model to induce HCC formation independently of liver zonation, recapitulating hepatocarcinogenesis. The model was complemented with a multifocal GEM model, and tumor-derived organoids were established from both *in vivo* models. The models were used to investigate the angiocrine and autocrine role of Wnt signaling in HCC initiation and progression. I discovered a decrease in the expression of Rspo3 and Evi/Wls in liver tumor ECs, which was also validated in human livers in the case of Rspo3. At the autocrine level, decreased Wnt expression induced vessel regression and maturation. From the angiocrine point of view, this differential Wnt expression was intended to sustain a protumorigenic liver microenvironment, which in turn induced a decrease in endothelial Wnt expression, creating a positive feedback loop. This study presented

angiocrine Wnt factors as gatekeepers of the healthy endothelium. Rspo3 was identified as a potential antitumorigenic factor that can reduce tumor cell proliferation. These findings require further validation in larger cohorts and more clinically relevant models, such as the western diet. Additionally, the exact mechanism of action between liver tumor cells and endothelial-derived Wnts requires further investigation.

5. MATERIALS AND METHODS

5.1. Materials

5.1.1. Chemicals

Chemicals were purchased from the following companies:

Table 2. Chemicals

Company	Company reference webpage
AppliChem	www.applichem.com
B.Braun	www.bbraun.de
Carl Roth	www.carlroth.com
Gerbu	www.gerbu.de
Merck	www.merck.de
Qiagen	www.qiagen.com
Roche	www.roche.com
Santa Cruz Biotechnology	www.scbt.com
Selleckchem	www.selleckchem.com
Sigma-Aldrich	www.sigmaaldrich.com
Thermo Fisher Scientific	www.thermofisher.com

5.1.2. Enzymes

Table 3. Enzymes

Reagent	Company
Collagenase D	Merck
Liberase	Roche
Proteinase K	Qiagen
RNase-free DNase	R&D Systems

5.1.3. Growth factors and proteins

Table 4. Growth factors and proteins

Reagent	Company
Ampicillin	AppliChem
Recombinant mouse EGF	Thermo Scientific (Gibco)
Recombinant human Gastrin	Sigma Aldrich
Recombinant human FGF10	Peprotech
Recombinant mouse HGF	Peprotech

Forskolin	HelloBio
TGFb inhibitor	Biozol
Rock inhibitor (Y27632)	ATCC
Recombinant mouse Noggin	Peprotech
Recombinant mouse Rspo1	R&D Systems
Recombinant mouse Rspo3	R&D Systems
Recombinant mouse Wnt3a	PeproTech

5.1.4. Cells

Table 5. Murine cell lines

Cell	Description	Source	Medium
Hepa1.6	Murine HCC cell line	Prof. Dr. Kai Breuhahn (Michaela Bissinger)	DMEM + 10% FCS + 1% penicillin/streptomycin
Primary LSECs	Murine primary LSECs isolated by perfusion	Perfusion based digestion from BL6 mice as indicated in section 5.2.5	Complete Endothelial Cell Medium (Cell Biologics)
Tumor derived organoids	Primary tumor derived organoids isolated from HCC tumor bearing mice	Digestion from EPO and iAST tumors from BL6 mice as indicated in section 5.2.4	Advance DMEM with all supplements as described in section 5.2.4

5.1.5. Cell culture reagents

Table 6. Cell culture reagents

Reagent	Company
B-27™ Supplement	Thermo Scientific
Complete Endothelial Cell Medium kit (including supplements)	Cell Biologics
Dimethylsulfoxide (DMSO)	AppliChem
Dulbecco´s phosphate buffered saline (PBS)	Sigma Aldrich
Dulbecco's Modified Eagle medium - Glutamax (DMEM)	Thermo Fisher Scientific
Fetal Calf Serum (FCS, heat-inactivated)	Gibco
Glutamax	Gibco
HEPES	Gibco
Hydroxytamoxifen	Sigma Aldrich
N-2 Supplement	Thermo Scientific
n-Acetyl-cysteine	Sigma Aldrich
Nicotinamide	Sigma Aldrich
Penicillin/streptomycin (100x 104U/10mg/ml)	Sigma Aldrich
Reduced growth factor BME	R&D Systems
Trypan blue	Thermo Fisher Scientific
TrypLE	Thermo Fisher Scientific

Trypsin-EDTA (10x)	Sigma Aldrich

5.1.6. Bacteria strains

Table 7. Bacteria strains

Description	Source
E. coli pALB-SB13	DKFZ (Dr. Anja Runge)
E. coli pT3_EF1a_Cmyc	DKFZ (Dr. Anja Runge)
E. coli pT_EF1a_KRasG12V	DKFZ (Dr. Anja Runge)
E. coli Stbl3 pRP[CRISPR]-hCas9-U6>{p536 guide ghAlb>hCas9:BGH pA	Vector Builder
E. coli pSBT-FLucL272A	DKFZ (Prof. Dr. Ana Banito)

5.1.7. Primers and oligonucleotides

All primers were purchased from Eurofins, except for SV40TAg from Taqman (Applied Biosystems).

Table 8. Primers and oligos

Primer name	Application	Sequence (5´-3´)
Actb-Fwd	Genotyping: VE-Cad-Cre^{ERT2}	CAATGGTAGGCTCACTCTGGGAGATGATA
Actb-Rev	Genotyping: VE-Cad-Cre^{ERT2}	AACACACACTGGCAGGACTGGCTAGG
Cre-Fwd	Genotyping: VE-Cad-Cre^{ERT2}	GCCTGCATTACCGGTCGATGCAACGA
Cre-Rev	Genotyping: VE-Cad-Cre^{ERT2}	GTGGCAGATGGCGCGGCAACACCATT
Evi/Wls-Fwd	Genotyping: Evi/Wls floxed	AAGGAAACGAGATTGAGATGAGG
Evi/Wls-Rev	Genotyping: Evi/Wls floxed	GTTTATTTTTCCTCTTACCACTCTG
Rspo3-Fwd	Genotyping: Rspo3 floxed	ATGCTTTGAGGCTTGTGACC
Rspo3-Rev	Genotyping: Rspo3 floxed	TACATTCTGGTTTCTCATCTGG
SV40TAg-Fwd	Genotyping: SV40TAg	TTAGCAATTCTGAAGGAAAGTCCTTG
SV40TAg-Rev	Genotyping: SV40TAg	ACCTGTTTTGCTCAGAAG
MGSO	Mycoplasma detection	TGCACCATCTGTCACTCTGTTAACCTC
GPO	Mycoplasma detection	GGGAGCAAACAGGATTAGATACCCT

5.1.8. TaqManTM assays

All TaqMan^{TM} asays were purchased from Applied Biosystems.

Table 9. Mouse TaqManTM assays

Gene	Ordering number
Actin	Mm00607939_s1
Alb	Mm00802090_m1
Aplnr	Mm00442191_a1
Axin2	Mm00443610_m1
Cd44	Mm01277160_m1
Cd9	Mm00514275_g1

Dll4	Mm00444619_m1
Efnb2	Mm00438670_m1
Emr1	Mm00802529_m1
Evi/Wls	Mm00509695_m1
Gata4	Mm00484689
Hnf4a	Mm01247712_m1
ICAM-1	Mm00516023_m1
Itga6	Mm00434375_m1
Lgr5	Mm00438890_m1
Ly6a	Mm00726565_s1
Lyve1	Mm00475056_m1
mKi67	Mm01278617_m1
Pecam1	Mm01242584_m1
Ptprc	Mm01293577_m1
Rspo3	Mm01188251_m1
SV40	FAM—MGB based*
Wnt2	Mm00470018_m1
Wnt4	Mm01194003_m1
Wnt9b	Mm00457102_m1
Znrf3	Mm01191453_m1

*5'- ATGTTGAGAGTCAGCAGTAGCC-3'

5.1.9. PCR reagents

Table 10. Reagents for RT, PCR and qPCR

Reagent	Company
Direct PCR Lysis Reagent	PeqLab
DNase/Rnase free H2O	Gibco
QuantiTect Reverse Transcription Kit for cDNA Synthesis	Qiagen
RedTaq® ReadyMix™ PCR Reaction Mix	Sigma-Aldrich
TaqMan® Fast Advanced PCR Master Mix Applied	Biosystems

5.1.10. Antibodies

Table 11. Primary antibodies

Antigen - clone	Reactivity	Species	Dilution	Conjugate	Company	Ordering number	Application
CD3	Human, mouse	Rabbit	1:200	-	Agilent	A045229-2	IF
CD31	Mouse	Goat	1:100	-	R&D Systems	AF3628	IF
Desmin	Mouse	Rabbit	1:200	-	Abcam	Ab15200-1	IF

E-cadherin	Mouse	Mouse	1:100	-	BD Bioscience	610181	IF
Glutamine Synthetase	Human, mouse	Rabbit	1:1000, $1:10^4$	-	Abcam	ab49873	IF
αSMA	Mouse	-	1:200	Cy3	Sigma	C6198	IF
CD146 [ME-9F1]	Mouse	-	1:200	PECy7	BioLegend	134713	Flow cytometry
CD16/32	Mouse	-	1:100	-	e Bioscience	14-0161-86	Flow cytometry
CD31 [MEC13.3]	Mouse	-	1:200	APC	BD Bioscience	551262	Flow cytometry
CD31 [MEC13.3]	Mouse	-	1:200	PE	BD Bioscience	553373	Flow cytometry
CD45.2 [30-F11]	Mouse	-	1:200	FITC	BD Bioscience	553080	Flow cytometry

Table 12. Secondary antibodies

Reactivity	Species	Dilution	Conjugate	Company	Ordering number
Goat	Donkey	1:400	Alexa Fluor 647	Life Technologies	A21447
Goat	Donkey	1:400	Alexa Fluor 488	Life Technologies	A11055
Mouse	Donkey	1:400	Alexa Fluor 647	Life Technologies	10-1223
Rabbit	Donkey	1:400	Alexa Fluor 546	Invitrogen	A10040
Rabbit	Donkey	1:400	Alexa Fluor 647	Life Technologies	A31573
Rabbit	Goat	1:400	Alexa Fluor 546	Life Technologies	A11071
Rabbit	Goat	1:400	Alexa Fluor 488	Invitrogen	A21206

5.1.11. Staining reagents

Table 13. Staining reagents

Reagent	Company
Bovine Serum Albumin	PAA
CD31 MicroBeads, mouse	Miltenyi Biotech
Donkey serum	Thermo Fisher Scientific
Fetal Calf Serum (FCS, heat inactivated)	PAA
Fluorescent mounting medium	Dako
FxCycle Violet	Thermo Fisher Scientific
Histomount	Thermo Fisher Scientific
Hoechst Dye 33258	Merck
Mayers' Hematoxylin solution	Sigma-Aldrich
Normal goat serum ready-to-use	Zymed
Tissue-Tek® O.C.T.™ Compound	Scigen

5.1.12. Kits

Table 14. Kits and RNA/DNA extraction

Reagent	Company
Arcturus PicoPure RNA Isolation Kit GenElute	Thermo Fisher Scientific
Click-iT™ EdU Alexa Fluor Flow Cytometry Kit	Thermo Fisher Scientific
EndoFree Plasmid Mega, Giga Kits	Qiagen
GenElute Mammalian Total RNA Purification Kit	Sigma
PureLinkTM Quick Plasmid Miniprep-Kit	Thermo Fisher Scientific
QuantiTect® Reverse Transcription Kit for cDNA Synthesis	Qiagen
RNase-Free Dnase	Qiagen

5.1.13. Reagents for animal experimentation

Table 15. Reagents and tool for animal experimentation

Reagent	Company
Alcoholic iodine solution	WDT
Bepanthen eye cream	Roche
Ethicon suture silk 4-0	Johnson & Johnson MEDICAL
Ethicon suture silk 5-0	Johnson & Johnson MEDICAL
Ketamin	Pfizer
Liver Digestion Medium	Thermo Fisher Scientific
Liver Perfusion Medium	Thermo Fisher Scientific
Metamizol/Metapyrin	Serumwerk
NaCl solution 0.9%	Braun
Peanut oil	Sigma Aldrich
Rompun	Bayer
RPMI	Thermo Fisher Scientific
Surgical tools and equipment	Fine Science Tools
Tamoxifen	Sigma Aldrich
XenoLight RediJect D-Luciferin Ultra	PerkinElmer

5.1.14. Consumables

Table 16. Plastic ware and consumables

Consumable	Company
384 well plates	4titute
96 well plates	Steinbrenner Laborsysteme
Blood glass capillary	VWR international
Blood lancet	Th. Geyer
Cannula (18G, 19G, 27G)	BD
Cell culture dishes (6, 12, 24, 48 well plates, 10cm)	Sarstedt

Cell scraper	Corning
Cell strainer (100 µm)	BD Falcon
Cotton swab	Edeka elcos face
Countess™ cell counting chamber slides	Invitrogen
Cryotubes	Carl Roth
Disposable scalpel (No. 15, 20)	Feather
FACS tubes	BD Biosciences
FACS tubes with strainer cap	Corning
Filter containing pipette tips	Sarstedt
Hamilton syringe (27G)	Hamilton
Micronfine (29G, 30G)	BD
Microscope cover glasses	VWR international
Microscope glass slides	Menzel-Gläser
Microtome blade (N35)	PFM medical
MS columns	Miltenyi Biotech
Pipette tips	Nerbe
Pipette tips - filter	Sarstedt
Pipette tips - multichannel	Rainin
Reaction tubes (0.2ml, 0.5ml, 1.5ml, 2ml)	Eppendorf
Reaction tubes (1.5ml) - DNA LoBind	Eppendorf
Reaction tubes (15ml, 50 ml)	Greiner
Sealing foil	Applied Biosystems
Sterile pipettes	Corning
Syringe - SoftJect 1ml	Thermo Fisher Scientific
Syringes	Dispomed
Tissue embedding cassetes	Kartell Spa

5.1.15. Devices

Table 17. Devices and equipment

Equipment	Company
Aria cell sorting platform	BD Biosciences
Axio ScanZ7.1 slide scanner	Zeiss
Canto II	BD Biosciences
Cell culture hood	Thermo Fisher Scientific
Cell culture incubator	Thermo Fisher Scientific
Centrifuge	Eppendorf
Confocal Leica TCS SP8	Leica
Confocal Zeiss LSM 710 ConfoCor3	Zeiss
Countess automated cell counter	Thermo Fisher Scientific
Heating block	Eppendorf
HM355S microtome	Thermo Fisher Scientific
IVIS Lumina Series III	PerkinElmer
Light cycler 480	Roche
MasterCycler 384-Well	Eppendorf

Microm EC 350-2 (tissue embedding)	Thermo Fisher Scientific
Mixer mill MM200	Retsch
Mr. Frosty Freezing Container	Thermo Fisher Scientific
BioSpec Bruker 3/9.4Tesla	Bruker
Multichannel pipete	Rainin
Multistep pipete	Eppendorf
Nanophotometer N60	Intas
NEPA Super Electroporator	NEPAGENE
Olympus IX 71	Olympus
Peristaltic pump	Ismatec
Pipetes	Eppendorf
Power supply	BioRad
QIAxcel Advanced System	Qiagen
QuadroMACS multistand	Miltenyi Biotech
Scale	Ohaus
Shaver	Moser
Special accuracy weighing device	Metler Toledo
Spin tissue processor STP120	Thermo Fisher Scientific
StepOnePlus Real-Time PCR System	Thermo Fisher Scientific
Table centrifuge (5417R)	Eppendorf
Thermocycler	Thermo Fisher Scientific
Vortex	Neolab
Water bath	Julabo
Warm pad	ThermoLux

5.1.16. Softwares

Table 18. Software

Software	Company
Cell P® software	Olympus
FACSDivaTM	BD
Fiji	ImageJ
FlowJo	Miltenyi Biotec
Graph Pad Prism (v6.0, v8.0)	Graph Pad
Leica LAS X (v3.7.6)	Leica
Light Cycler 480 software	Roche
Living Image Software version 4.5.5	PerkinElmer
RadiAnt DICOM Viewer	RadiAnt
StepOne™ Software v2.1	Applied Biosystems
ZEN black	Zeiss
ZEN blue	Zeiss

5.1.17. Solutions

Table 19. Solutions and buffers

Buffer	Formulation	
4% Paraformaldehyde (PFA)	4 % (m/v) ~1/400 1/10	Paraformaldehyde in VE water NaOH (until dissolve) adjust pH7.2-7.4 10x PBS adjust pH7.4
Ammonium chloride potassium buffer (ACK buffer)	150mM 10 M 100 mM	NH_4Cl $KHCO_3$ Na_2EDTA Adjust pH 7.2-7.4
Blocking buffer (organoids staining)	0.3%	Triton X-100 in 10% Normal Goat serum ready to use
Blocking buffer (tissue staining)	10% 3%	Fetal calf serum Bovine serum albumin in PBS
FACS buffer	5% (v/v)	Fetal calf serum in PBS
LB Medium	12 gr. 5gr. 5gr. 1 gr. 1 L 1/1000	Tryptone enzymatic digest from casein Yeast exctract Sodium chloride D-(+)-glucose VE water Autoclaved and add amplicilin
Phosphate buffered saline (PBS)	1.34 M 27 mM 200 mM 4.7 mM	NaCl KCl Na_2HPO_4 KH_2HPO_4 Adjust pH 7.4
TE buffer	0.1 mM 10 mM	EDTA Tris-HCl pH 8.0
Tris-Buffered Saline Tween-20 (TBS-T)	10 mM 100 mM 0.1 %	Tris/HCl, pH 7.5 NaCl Tween-20
Wash Buffer (organoids isolation)	1% 1%	Fetal calf serum penicillin/streptomycin in DMEM

5.2. Methods

5.2.1. Animal studies

5.2.1.1. Animal husbandry

C57BL/6J (wildtype) mice were purchased from Janvier. Transgenic mouse lines for endothelial-Wnt deletion (B6 Evi/Wls$^{fl./fl.}$ x Cdh5-Cre^{ERT2}, B6 Rspo3$^{fl./fl.}$ x Cdh5-Cre^{ERT2}, B6 Rspo3$^{fl./fl.}$ x Evi/Wls$^{fl./fl.}$ x Cdh5-Cre^{ERT2}) and the iAST transgenic model (88, 102, 113), were used for the study and to generate three additional mouse lines. Each of the Wnt-iECKO were bred with the iAST to induce the iAST model in the background of endothelial deleted Wnt signaling. All mice were homozygous for the floxed allele; either heterozygous or negative for the Cre allele, representing Cre + or control Cre – mice. All mice were housed in specific pathogen-free animal facilities and in a temperature-controlled 12h light/dark cycle with *ad libitum* access to food and drinking water. All animal experiments were performed under the guidelines of the governmental animal Care and Use Committees and approved by the regional council Karlsruhe (DKFZ370, EP-Z111I02, G-291/15, G-107/18 and G-36/22).

5.2.1.2. Tamoxifen administration

Cre deletion was induced in 8 to 12 weeks old mice by intraperitoneal administration during five consecutive days with 50 μL of a 40mg/mL of Tamoxifen (Sigma Aldrich), followed up by two weeks washout period. Tamoxifen was dissolved in 100% ethanol (1/500 ml/mg) and subsequently in peanut oil (8% vol/vol).

5.2.1.3. Tumor models

Tumors were induced in both models in mice between 8 to 12 weeks old. If applied, tamoxifen administration started at this aged, and tumors were induced after the washout period.

Focal electroporation-liver tumor model

Mice were anesthetized with a solution of Ketamin (120mg/kg) and Xylazin (16mg/kg) diluted in 0.9% NaCl injected i.p. After fixation on a heat mat, eyes were prevented to drying with Bepanthen cream. The abdominal area below the breastbone was sterilized with 70% ethanol and an incision was made in the linea alba in the skin and peritoneum. The left lobe was exposed with a Bowman and two sterile applicators. Plasmid solution was injected with a Hamilton syringe in the left liver lobe under the liver subcapsule towards the edge. Subsequently immediately after injection, electrodes were placed covering the site of injection to electroporate with transfer pulse settings as follows: voltage (35.0 V), pulse length

(35.0 msec), pulse interval (500.0 msec), n° of pulses (4), decay rate (0%) and polarity (+/-). Afterwards, mouse cavity was washed with 10mL pre-warm 0.9% NaCl solution to ensure complete removal of potential left over plasmid solution. Lastly, both the peritoneum and the skin were sutured with 5 and 4 suture silk, respectively. Mice were monitored to ensure recovery from the intervention, and thereafter, to determine when the defined endpoint criteria was reached while measuring tumor growth.

AdCre injection in AST model

Deletion of the stop cassette in the iAST transgenic mice was induced by tail vein injection of adenovirus expressing Cre recombinase (Vector Biolabs/SignaGen). Stock virus solution was diluted prior injection in 0.9% NaCl solution up to $1x10^9$ PFU in 100 μL per mouse. Injection was performed under a laminar flood hood, where mice were fixed with a mouse restrainer and tail vein was dilated using a red light.

5.2.1.4. Tumor detection

Mice were regularly checked for general health status. Tumor growth was monitored via MRI or IVIS, depending on the tumor model and as indicated for each experiment.

Magnetic resonance imaging (MRI)

MRI was carried out in the small animal imaging core facility in DKFZ using a Bruker BioSpec 3/9.4Tesla (Ettlingen, Germany) with ParaVision software 360 V1.1. For the imaging, mice were anesthetized with 3.5% sevoflurane in air. For lesion detection, with 3 Tesla MRI,T2 weighted imaging were performed using a T2_TurboRARE sequence: TE = 48 ms, TR = 2200 ms, FOV 35x35 mm, slice thickness 1,3mm, averages = 6, Scan Time 5m16s, echo spacing 12 ms, rare factor 8, slices 17, image size 192x192, resolution 0,182mm." For lesion detection, with 9.4 Tesla, T2 weighted imaging were performed using a T2_TurboRARE sequence: TE = 25 ms, TR = 2200 ms, FOV 35x35 mm, slice thickness 1 mm, averages = 3, Scan Time 3m31s, echo spacing 6.4 ms, rare factor 8, slices 20, image size 256x256. Tumor volume was calculated measuring nodule area by Image J software exports from RADIANT DICOM Viewer and multiplying by slide thickness (based on MRI raw data). Single nodules were selected manually in each slide from RADIANT DICOM exports.

IVIS

IVIS Lumina Series III with the XFOV-24 lens attached and the Software Living Image 4.5.5 were used to measure tumor luminescence in mice expressing luciferase. Mice were anesthetized with isofluorane 2.1% vol./vol. at a flow rate of 4-5L/min. Subsequently, mice were i.p. injected with IVISbrite D-Luciferin Ultra, RediJect (PerkinElmer) based on body weight (30mg/mL at 150 mg/kg body weight) and incubated for 10

minutes. During this time, mice were shaved on the abdomen, eyes were covered with Bepanthen cream, and transferred to the imaging chamber in supine position with a isoflurane flow rate of 1.5L/min. Imaging was performed with the following settings: exposure time (7 min), binning (8), f/stop (1,2), excitation filter blocked and emission filter opened. Mice were defined using the "Subject" tool and ROIs over the abdominal region where the liver is located. Tumor growth was followed over time based on the "Total flux" parameter given as raw data.

5.2.1.5. Blood withdrawal

Blood sampling was taken consistently by cheek bleed using a lancet at similar times of the day. Blood was collected with a blood glass capillary and centrifuged at 13,000G for 10 min. at 4°C. Supernatant was kept at -20°C and send for serum analysis.

5.2.2. Large scale plasmid production

Glycerol stock for each plasmid was prepared and kept at -80°C. Plasmids were cultured and purified according to manufacter instructions Endofree Plasmid Giga Kit (Qiagen) with certain modifications. Plasmids were first recovered in 5 mL of autoclaved LB medium containing glucose, and 0.1mg/mL of ampicillin for plasmid selection; and incubated overnight at 37°C with vigorous shaking. Initial culture was diluted 1/125 and transfer into 250 mL of fresh LB medium supplemented with glucose and ampicillin as before, and incubated for 10-12h in the same conditions. Subsequently, it was transferred to 3 to 5 liters of the same medium in a 1/100 dilution and incubated for at least 12-16h in the above-mentioned conditions. Bacteria was harvest by several rounds of centrifugation at 5525G for 17 minutes at 4°C. Pellet was resuspended and collected in 250 mL of provided Buffer P1 (containing RNase A and Lyse Blue reagent). Equal volume of Buffer P2 was mixed by vigorously inverting until whole solution turned blue, and incubated at RT for 5 min. Afterwards, same volume of 4°C-temperature Buffer P3 was added and mixed until blue traces were gone. Resulting solution was centrifuged at 5525G for 30 min at 4°C and the mid-layer solution was transferred to the QIAfilter Mega-Giga Cartridge provided, filtered through by vacuum force and collected. Consequently, 50mL of buffer FWB2 were added to the filter and the obtained lysate was incubated with 30mL of buffer ER on ice for 30 minutes. The solution was applied onto a pre-equilibrated QIAGEN-tip 1000 (by loading 75 mL of buffer QBT) and let it empty by gravity flow. The column was washed with 600 mL of buffer QC and DNA was eluted with 100 mL of buffer QN. DNA was precipitated by mixing lysate with 0.7 volume of RT isopropanol and centrifuging at 15,000G for 30 min at 4°C and further washed with 10 mL of provided 70% ethanol. After centrifugation in the same

conditions for 10 minutes, the pellet was air-dried until there were no traces of alcohol. DNA was finally resuspended in the desired volume of buffer TE and concentration was quantified with Nanodrop at 260 nm. DNA was stored at -20°C at the adequate concentration for i*n vivo* application.

5.2.3. Isolation of liver (tumor) endothelial cells

Mice were euthanized by cervical dislocation and livers were extracted. Whole liver or tumor tissue (i.e. from the left lobe in electroporated mice or from the nodules in the iAST mice) were finely chopped with curved scissors and digested in RPMI-1640 (Life Technologies) supplemented with 20μg/mL Liberase (Roche) and 2% DNase I (Roche) for 20 mins. at 37°C with agitation. After resuspension with a 18G syringe, solutions were incubated for further 10 minutes in the same conditions. Digestion was resuspended with a 19G syringe and filtered through 100μM cell strainer into a 50 mL tube filled up with FACS buffer. Centrifugation at 50G for 3 minutes led to the separation of hepatocytes in the pellet and NPCs in the supernatant. Supernatant was resuspended at 300G for 10 minutes and the derived pellet incubated in ACK Lysis buffer for 2 minutes at RT to lysis red blood cells. Reaction was stopped adding 10mL of FACS buffer (PBS with 5% FCS) and centrifuging at 480G for 5 minutes. Pellet was resuspended in Fc-block (BD Bioscience), diluted 1:100 in FACS buffer and incubated on ice for 20 minutes. If CD146 preselection was performed, solution included 20μL of CD146-MicroBeads (Miltenyi Biotec) and incubated with rotation. In this case, after washing with 1mL of FACS buffer and centrifugation at 300G for 5 minutes at 4°C, the pellet was resuspended in 1mL of buffer and load through a filter into LS columns (Miltenyi Biotec), pre-equilibrated with 4mL FACS buffer. Following 3 washes of the columns with 3 mL FACS buffer, the magnetically attached cells were eluted by separation of the column from the magnetic rack (Miltenyi Biotec) and elution in 2mL of FACS buffer with the plug provided. The pellet obtained after centrifugation at 400G for 5 minutes, after Fc block incubation or LS columns, was incubated with flow cytometry antibodies in FACS buffer: CD31-APC/PE, CD146-PECy7 and CD45.2-FITC at a dilution 1:200 for 20 minutes on ice in the dark. After washing, cell suspensions were resuspended in 1mL FACS buffer and filtered into FACS tubes. Before FACS sorting, samples were resuspended with Fxcycle Violet Stained (Invitrogen) 1:1000.

5.2.4. Isolation of tumor-derived organoids

Tumor dissection was performed under sterile conditions in a tissue culture hood. Tumor tissue was isolated from tumor bearing mice of either one of the models described in the above “Tumor models” section. Tissue of approximately 0.5cm^3 was chopped with curved scissors and diluted in “wash buffer” (i.e. DMEM supplemented with 1% FCS (Gibco) and 1% penicillin/streptomycin (Sigma)) in a 15 mL tube.

Suspension was let to pellet by gravity, supernatant was removed and filled it up again with wash solution. This procedure was repeated up to 4 times until the supernatant was cleared. Pellet was resuspended in 5 mL of wash buffer containing 2.5mg/mL of Collagenase D (Sigma) and 0.1 mg/mL DNase I (Roche) for digestion at 37°C with vigorous shaking for 1 hour. To ensure efficient digestion, tube was vortex in between digestion, and later on resuspended with 18G and 19G syringe. Solution was filtered through a 100 μM cell strainer and collected in a 50mL tube, and top up with wash solution. After centrifugation at 300G for 5 minutes at 4°C, pellet was resuspended in 5 mL wash solution, transferred to a 15mL tube and further diluted up to 15 mL in wash solution. This wash was repeated for up to 3 times and one additional time to be resupended in 15 mL of basal organoids media: AdDMEM (Gibco) supplemented with 1% HEPES (Gibco), 1% Glutamax (Gibco) and 1% penicillin/streptomycin (Sigma). Pellet obtained after additional centrifugation was resuspended in Cultrex Reduced Growth Factor Basement Membrane Extract, Type 2, Pathclear (R&D Systems), hereafter designated as BME. This was plated into a pre-warm 24-well plate in 20μL drops and incubated at 37°C for 30 minutes to solidify the BME. Finally, to each well it was added complete organoids media. This included basal organoids media supplemented with B-27™ Supplement (Thermo Scientific), N-2 Supplement (Thermo Scientific), 500mM n-Acetyl-cysteine (Sigma), 50 μg/mL murine EGF (Gibco), 62.5 μM human Gastrin (Sigma), 50 μg/mL human FGF10 (Peprotech), 50 μg/mL murine HGF (Peprotech), 1 M Nicotinamide (Sigma), 1 mM Forskolin (HelloBio), 5mM TGFβ inhibitor (Biozol), 1mM Rock inhibitor (Y27632) (ATCC) and 100 μg/mL murine Noggin (Peprotech). Additionally, recombinant murine 25 ng/mL Rspo1 (R&D Systems) and 10μg/mL Wnt3a (Peprotech) were supplemented for testing purposes. Medium was changed every 3 days into fresh complete organoids media.

5.2.5. Isolation of primary liver sinusoidal endothelial cells for *in vitro* culture

Mice were euthanized by cervical dislocation and subsequent steps were performed in sterile conditions in a tissue culture hood. An incision all along the linea alba up to the xiphoid process was made to expose the visceral organs in the abdominal cavity and the vena cava. It was perfused with a needle connected to a peristaltic pump (Ismatec). Once the liver infusion was successful, portal vein was cut. The livers were initially perfused with pre-warm Liver Perfusion Medium (Life Technologies) for 2 minutes at a flow rate of 5mL/min and later on, digested with pre-warm Liver Digestion Medium (Life Technologies) containing 40μg/mL of Liberase TM (Roche). Digested livers were explanted into Petri dishes with pre-warm RPMI (Gibco). After gallbladder removal, the cell suspension encapsulated in the liver capsule was dissolved in the media and transferred to a 50 mL tube through a 100μM filter. The solution was filled up to 50mL and

centrifuged twice at 50G for 5 minutes at 4°C to pellet hepatocytes. Supernatant was transferred again into a 50mL tube and centrifuge at 300G for 10 minutes at 4°C to precipitate NPCs. Isolation of LSECs from NPCs pellet was performed as previously described for flow cytometry including CD146 microbeads enrichment. After elution from the column, cells were centrifuged at 300G for 5 minutes at 4°C and resuspended in Endothelial Cell Medium (Cell Biologics) with all the supplements provided (i.e. 0.5 mL VEGF, 0.5 mL ECGS, 0.5 mL heparin, 0.5 mL EGF, 0.5 mL hydrocortisone, 5mL antibiotic-antimycotic and 25 mL FBS). Cells were seeded into 6-well plates based on cell pellet after final centrifugation. LSECs were allowed to seed for 2 days and identity was confirmed based on fenestrated morphology under the microscope. The cells were then ready to use for the corresponding experiment.

5.2.6. Flow cytometry and cell sorting

NPCs from healthy and tumor livers were digested as previously described in the section 5.2.3. Cell suspension stained was sorted using a BD FACS Aria cell sorter platform (BD Bioscience). Firstly, FSC-A and SSC-A were used to exclude cell debris, either SSC-A and SSC-B or FSC-A and FSC-W to select for single cells, FxCycle Violet stained to exclude for dead cells and eventually CD45 negative and CD31 and CD146 for EC (i.e. CD45-CD31+CD146+) and tumor cells (i.e. CD45-CD31-CD146-), respectively.

5.2.7. Immunofluorescence staining

5.2.7.1. Preparation of paraffin blocks and sections

Extracted tumors were fixed overnight in 4%PFA at 4°C in slight agitation. After two washes in VE-water, sections were processed in a spin tissue processor STP120. This included serial incubations with agitation in increasing concentrations of ethanol (70-85-96%), isopropanol, xylol and paraffin. Afterwards, samples were embedded in paraffin blocks and cut 5μM thick using a rotary microtome HM355S.

5.2.7.2. Preparation of cryoblocks and cryosections

Excised livers and tumors were fixed in 4% PFA overnight, and afterwards transferred to 30% sucrose solution for dehydration. The day after, samples were embedded in TissueTek O.C.T compound (Sakura) and let it solidify on dry ice. Sections were stored at -80°C and cut using cryomicrotome Hyrax C50 (Zeiss) at 5μM thickness.

5.2.7.3. Immunofluorescence staining of tissue sections

Paraffin or cryosections were used for immunofluorescence staining. Paraffin sections were dewaxed by incubating twice in Histo-clear for 5 minutes and graded ethanol solutions (99-99-80-70%) for 2 minutes

each. Cryosections were incubated for 20 minutes at RT and wash with PBS to remove OCT. Antigen retrieval was performed with Citrate Buffer pH6.0 (DAKO) incubated at 99°C for 20 minutes in a water bath and after cooling down for 15 minutes at RT, sections were washed twice in PBS for 2 minutes. Alternatively, Protein K was incubated 1:20 in buffer TE at 37°C for 10 minutes followed by wash in PBS/0.1% Tween for 5 mins. Subsequently, sections were incubated in blocking buffer for 1 hour at RT. Choice of antigen retrieval methods and blocking buffer was based on primary antibody and embedding method as indicated in Table 20. Antigen retrieval method. Primary antibodies were incubated for 2 hours at RT or overnight at 4°C in blocking buffer [CD31 anti-goat (R&D Systems), Desmin anti-rabbit (Abcam), Collagen IV anti-rabbit (Abcam), Glutamine Synthetase anti-rabbit (Abcam), E-cadherin anti-mouse (BD Bioscience), CD3 anti-rabbit (Agilent)]. After three washes on TBST for 5 minutes with agitation, samples were incubated for 45 minutes at RT in Hoechst33342 (Sigma Aldrich) staining (1:2000) plus the respective secondary antibodies [anti-goat Alexa 488, anti-rabbit Alexa 488, anti-rabbit Alexa 546, anti-rabbit Alexa 647, anti-goat Alexa 647, anti-mouse Alexa 647, (LifeTechnologies), anti-mouse αSMA-Cy3 (Sigma)]. Lastly, samples were washed three times and mounted with DAKO mounting medium (Agilent). Images were acquired with Zeiss Axio Scan and images analyzed with Fiji.

Table 20. Antigen retrieval method

Staining	Embedding	Antigen Retrieval	Blocking Buffer
CD31/Desmin/αSMA	Paraffin	Protein K	10% FCS 3%BSA in PBS
Glutamine Synthetase/E-cadherin	Paraffin	Protein K	10% NGS ready to use (Agilent)
CD31/Collagen IV	Paraffin	Citrate Buffer	10% FCS 3%BSA in PBS
CD31/Desmin/αSMA	OCT	Citrate Buffer	10% FCS 3%BSA in PBS
CD3	OCT	Citrate Buffer	10% NGS 3%BSA in PBS

5.2.7.4. Histological evaluation

Paraffin blocks were cut into 5 μM thick sections using a rotary microtome HM355S. Sections were deparaffinized as previously described and incubated in freshly filtered Hematoxylin solution for 4 minutes. After washed sections for 10 minutes with tap water, slides were incubated with 1% ethanoic eosin solution for 2 minutes. Following three washes with VE-water, sections were incubated in increased graded ethanol solutions (70-80-99-99%), isopropanol and xylol. Sections were eventually mounted with Histomount.

5.2.7.5. Immunofluorescence staining of tumor-derived organoids

Tumor-derived organoids were detached by removing the medium and washing with PBS. BME was disrupted mechanically in PBS supplemented with 1% FCS. Tips and tubes were coated in cold PBS-1%BSA and the plate was also rinsed afterwards several times with this solution. Following centrifugation at 300G for 5 minutes, pellet was resuspended in 10mL cold PBS and centrifuge at 70G for 3 minutes. Pellet containing organoids was fixed in 1mL 4%PFA for 1 hour at 4°C shaking, and 10 more minutes with 10mL of PBS/1%FCS. Samples were washed twice with PBS/1%BSA and centrifuged at 200G for 3 minutes. Blocking and permeabilization was performed by incubation with blocking buffer (10% NGS supplemented with 0.3% Triton X-100) for 1 hour at RT shaking. Incubation with primary antibodies [anti-mouse EpCAM-FITC (eBioscience), anti-mouse Phalloidin-Alexa 546 (Thermo Fischer Scientific) and Hoechst33342; diluted 1:200, 1:100 and 1:1000, respectively] was performed at 4°C overnight on an orbital shaker. After washing twice, pellets were resuspended in fructose-glycerol solution (60% vol./vol. Glycerol in 2.5M fructose) for imaging. Images were taken with a confocal microscope LSM710.

5.2.8. Human patient samples

Paraffin-embedded liver sections from HCC and non-liver tumor patients were kindly provided by Prof. Carolin Mogler at the Institute for Pathology, Technich University Munich, Germany.

5.2.8.1. View RNA ISH plus fluorescence staining

Expression of Rspo3 in endothelial cells was detected by RNA *in situ* hybridization of *RSPO3* and *CD34* performed with ViewRNA™ Tissue Assay (Thermo Scientific), according to the manufacturer instruction. In short, paraffin sections were baked at 60°C for 1 hour in HybEZ oven, and deparaffinized washing the slides 3 times in xylene with frequent agitation for 5 minutes and twice with ethanol 100%. After air-drying, samples were incubated in pretreatment solution at 95°C for 20 minutes, and wash 3 times in VE-water and once in PBS for 2 minutes with frequent agitation. Following protease digestion at 40°C for 20 minutes, samples were washed twice in PBS with frequent agitation for 2 minutes, fixed in 4%PFA for 5 minutes at RT and washed twice again in PBS. Probe hybridization (*RSPO3* Type 1 Tissue Probe and *CD34* Type 6 Tissue Probe) was performed incubating the probes (1:40) in pre-warm Probe Set Diluent for 2 hours at 40°C. Subsequent of 3 washes for 3 minutes in constant and vigorous agitation in Wash buffer, samples were incubated for 25 minutes at 40°C in pre-warm Pre-Amplifier Mix. Later, sections were incubated with Amplifier Mix for 15 minutes and washed, in the same conditions. Samples were incubated at 40°C for 15 minutes with Label Probe 6-AP, diluted 1:1000 in pre-warm Label Probe, and washed 4 times in Wash buffer in constant and vigorous agitation. Afterwards sections were incubated with freshly

prepared Fast Blue Substrate for 30 minutes in the dark at RT. Reaction was stopped with subsequent washes, incubation with Reaction Stop Solution for 30 minutes at RT in the dark and washing twice for 2 minutes in PBS. Treatment with Label Probe1-AP for 15 minutes at 40°C, followed by incubation with AP Enhancer Solution for 5 minutes, and Fast Red Substrate for 1 hour, were performed as previously indicated. After wash twice with PBS for 2 minutes, immunofluorescence staining for GS and DAPI, was executed as previously described. Images were taken with confocal microscope Leica TCS SP8.

5.2.9. Cell culture

All *in vitro* procedures here described were performed under sterile conditions in a tissue culture hood.

5.2.9.1. Cell maintenance

Hepa1-6 cell line was cultured in high glucose DMEM (Gibco) supplemented with 10% FCS and 1% penicillin/streptomycin. Cells were maintained in culture by passing at above 80% confluence. After medium removal, cells were washed with PBS and detached by incubating with Trypsin-EDTA (Life Technologies) at 37°C for 3 min. Reaction was stopped by adding culture medium, and centrifuging at 200G for 3 min. Pellet was resuspended in culture medium and plate at 1/10-1/15 split ratio. Cells were maintained at 37°C under 5% CO_2.

5.2.9.2. Cryopreservation of cells

Murine HCC cell line was cryopreserved following a similar procedure as for cell maintenance. After centrifugation, pellet was resuspended in the adequate split ratio in culture medium supplemented with 10% FCS and 10% DMSO (Applichem). Cell suspension was aliquoted in cryovials (1 mL each) and kept in isopropanol containing freezing box (Mr. Frosty Freezing Container, Thermo Scientific), to be 24 h later transferred into liquid nitrogen tank for long-term storage. On the contrary, cell thawing was performed by incubating cryovials at 37°C in a water bath and resuspending cell suspension in culture media. After, centrifugation at 200G for 3 min, pellet was resuspended in culture media and plated as usual.

5.2.9.3. Tumor-derived organoids maintenance

Tumor-derived organoids were maintained in culture by passaging when they reached confluence, normally every 2-3 days. Medium was removed and cold basal media was added to resuspend BME drops containing organoids using mechanical disruption and scratching. Pull of up to 3 wells was collected in a 15 mL tube, top up to 15 mL basal media and centrifuge at 300G for 5 minutes at 4°C. Supernatant was discarded and pellet resuspended multiple times to break tumor organoids into aggregates of few cells

and single cells. Subsequently, pellet was resuspended in 5 mL pre-warm basal organoids media, top up to 10 mL and centrifugate at 150G for 5 minutes. Pellet was resuspended in BME, plated in 20μL drop onto a pre-warm plate and incubated for 30 minutes at 37°C to solidify. Afterwards, complete media was added on top in the same way as described after first isolation but without mNoggin. After 2-3 days, tumor-derived organoids were split, if confluence was reached, otherwise, media was changed into complete media.

5.2.9.4. Cryoperservation of tumor de organoids

Cryopreservation of tumor derived organoids was performed following a similar as for the HCC cell line. After resuspending tumor-derived organoids in cold media and centrifuged twice, the final pellet was resuspended in organoids freezing media consisting of 40% basal organoid media, 50% FCS and 10% DMSO. Approximately, 50 μL of confluent BME was resuspended in 1mL organoids freezing media and aliquoted in one cryovial. Cryovials were frozen and stored in the same way as for the cell line. Likewise, in order to thaw tumor organoids, cryovials were incubate at 37°C and cell suspension was transferred into a 15mL tube containing basal organoids media. Cell suspension was centrifuged at 150G for 5 minutes, and the pellet was resuspended in BME, plated on a pre-warm plate in 20μL drops and incubated at 37°C for 30 minutes. Complete media, including mNoggin, was added afterwards.

5.2.10. Cellular assays culture

5.2.10.1. In vitro treatment with hydroxytamoxifen

Primary isolated LSECs were treated with hydroxytamoxifen 48 hours after isolation in order to induce endothelial KO. Hydroxytamoxifen was prepared in a stock solution of 10 mM and further diluted in fresh culture media up to 2μM. Treatment lasted two consecutive days changing the media every 24 hours.

5.2.10.2. Production of conditioned medium

Two types of condition medium were produced: from the secretome of the murine HCC cell line and from freshly isolated LSECs in which ECKO was induced *in vitro* as previously described. In both cases after seeding, and hydroxytamoxifen treatment in the second case, cells were washed with PBS and starvation Endothelial Cell Medium was added to both cells. To ensure maximum concentration of secreted factors, half of the volume respective to the cell culture dish area was added and incubated for 48 hours at 37°C. Lastly, all medium was collected and centrifuged at 200G for 3 minutes. Conditioned medium corresponded to supernatant that was combined with 40% of complete Endothelial Cell Medium for treatment. For treatment of freshly isolated LSECs with tumor-derived conditioned medium, control

media corresponded to 60% starvation media. For liver endothelial cell conditioned media, media from LSECs isolated from Cre- and Cre+ mice were used as control and treatment, respectively, and further corroborated by qPCR. Both treatments lasted 48 hours.

5.2.10.3. Treatment with recombinant mRspo3

Hepa1.6 and tumor-derived organoids were treated with murine recombinant Rspo3 protein (R&D Systems). Lyophilized protein was dissolved in PBS at 200μg/mL. Stock was further diluted at different treatment concentrations (0, 5ng/mL, 25ng/mL, 1μg/mL, 10μg/mL) in cell line culture media, 24h after seeding, and in organoids culture media, after BME solidification. Treatment was terminated when confluence was reached, 48h and 72h after recombinant protein was added, respectively.

5.2.10.4. EdU cell proliferation assay

Proliferation assays of HCC cell line in different conditions and tumor-derived organoids were assessed using Click-iT® EdU Alexa Fluor® 647 Flow Cytometry Assay Kit (Life Technologies). Proliferation was determined in HCC cell line after treatment with LSECs conditioned media, and after recombinant Rspo3 treatment, in both the cell line and tumor derived organoids, as previously described. Hepa1.6 was incubated with EdU (10μM) for 3 and 4.5 hours after mRspo3 and conditioned media treatment, respectively, and tumor derived organoids for 6 hours. HCC cell line was harvest as usual. Tumor-derived organoids were detached as described for its immunostaining, then they incubated in 500μL of TrypLE (Life Technologies) at 37°C in a water bath for 5-8 minutes to be digested into a single cell solution. Reaction was stopped adding 1mL of basal organoids media and further diluting it up to 10mL. After centrifugation at 150G for 5 minutes, the pellet was washed once with 1mL PBS-1% BSA solution. For both cell line and tumor-derived organoids, medium and PBS from harvesting were collected. Furthermore, after harvest, plates were washed twice with FACS buffer and collected solution was centrifuged at 300G for 5 minutes. Pellet was resuspended in Cytofix/Cytoperm and incubated in the dark at 4°C for 20 minutes. Subsequently, it was resuspended in 1mL 1x Click-iT saponin-based permeabilization reagent (diluted in PBS) and centrifuged at 300G for 5 minutes. After 2 washes, samples were resuspended in 100mL of Click-iT master mix ($CuSO_4$ 1:50, Alexa Fluor 647 azide 1:200, 1x Click-iT EdU buffer additive in PBS) and incubated for 30 minutes at RT in the dark. After one wash in PBS, samples were diluted in PBS, and 1:1000 FxCycle Violet Stained (Invitrogen) when cell cycle distribution was examined. EdU and FxCycle Violet Stained incorporation was analyzed BD FACSCanto II flow cytometer and FlowJoTM software.

5.2.11. Molecular biology

5.2.11.1. Genotyping PCR

Ear punches were digested in 100µL of Direct PCR Lysis Reagent (Viagen) supplemented with 10mg Proteinase K at 55°C overnight. Reaction was stopped by heating at 95°C for 20 minutes. Debris was removed by centrifugation and lysate was kept at 4°C or -20°C, for short- or long-term storage. Genotyping was carried out using a REDTaq polymerase kit (Merck) as indicated in *Tables 20-23* for each gene in an Applied Biosystems thermocycler. Results were analyzed with a QIaxcel Advanced System according to the manufacter´s instructions.

Table 21. Cdh5 Cre-ERT2 Genotyping

PCR mix (REDTaq ReadyMix)		qPCR Programme		
		Step	**Temperature**	**Time**
ddH_2O	7 µL	1	95°C	2 min
REDTaq ReadyMix	10 µL	2	95°C	30 sec
Cre-Fwd	1 µL	3	58°C	45 sec
Cre-Rev	1 µL	4	72°C	2 min
Actb-Fwd	1 µL	Go to step 2: x 35		
Actb -Rev	1 µL	5	72°C	2 min
DNA	1 µL	6	4°C	∞
Transgene: 400 bp; internal control: 300 bp				

Table 22. Evi/Wls-floxed genotyping

PCR mix (REDTaq ReadyMix)		qPCR Program		
		Step	**Temperature**	**Time**
ddH_2O	9 µL	1	95°C	5 min
REDTaq ReadyMix	10 µL	2	95°C	30 sec
Evi/Wls-Fwd	1 µL	3	50°C	30 sec
Evi/Wls -Rev	1 µL	4	72°C	1 min
DNA	1 µL	Go to step 2: x 44		
		5	72°C	10 min
		6	4°C	∞
Floxed allele: 210 bp; wildtype allele: 340 bp				

Table 23. Rspo3-floxed genotyping

PCR mix (REDTaq ReadyMix)		qPCR Program		
		Step	**Temperature**	**Time**
ddH_2O	9 µL	1	95°C	2 min
REDTaq ReadyMix	10 µL	2	95°C	15 sec
Rspo3-Fwd	1 µL	3	55°C	30 sec
Rspo3 -Rev	1 µL	4	72°C	30 sec
DNA	1 µL	Go to step 2: x 34		
		5	72°C	10 min
		6	4°C	∞
Floxed allele: 410 bp; wildtype allele: 340 bp				

Table 24. AST genotyping

PCR mix		qPCR Program		
		Step	**Temperature**	**Time**
ddH_2O	7.72 µL	1	95°C	5 min
10x buffer (+KCl, -$MgCl_2$)	1 µL	2	95°C	40 sec
$MgCl_2$ (25 mM)	0.4 µL	3	60°C	30 sec
dNTPs (2.5 mM each)	0.2 µL	4	72°C	1 min
AST-Fwd (10 µM)	0.2 µL	Go to step 2: x 32		
AST-Rev (10 µM)	0.2 µL	5	72°C	10 min
DNA	1 µL	6	4°C	∞
Taq-polymerase LC (1U/µL)	0.08 µL			
Transgene: 500 bp; internal control: 300 bp				

5.2.11.2. Mycoplasma PCR

Mycoplasma was detected by removing 1 mL of cell culture and centrifuging to remove cell debris. 2 µL of supernatant were used for PCR according to *Table 24* using the Taq polymerase kit (Qiagen) in an Applied Biosystems thermocycler. Results were analyzed with the QIAxcel Advanced System according to the manufacter´s instructions.

Table 25.Mycoplasma detection

PCR mix (Qiagen)		qPCR Program		
		Step	**Temperature**	**Time**
ddH_2O	6.8 µL	1	95°C	5 min
Q-solution	2.6 µL	2	95°C	40 sec
Buffer 10x	1.25 µL	3	60°C	30 sec
$MgCl_2$	0.5 µL	4	72°C	1 min

dNTPs (2.5 mM)	0.25 μL	Go to step 2: x 32		
MGSO (10 μM)	0.25 μL	5	72°C	10 min
GPO (10 μM)	0.25 μL	6	4°C	∞
Taq (5 U/μL)	0.1 μL			
DNA	2 μL			
Mycoplasma contamination: 270 bp				

5.2.11.3. RNA extraction

RNA extraction from cell culture lysates was performed with the GenElute Mammalian Total RNA Purification kit (Sigma). At the end of the treatment, culture medium was removed, cells were washed with PBS and resuspended in 350μL of RNA Lysis Buffer. After proceeding according to the manufacter´s instructions, RNA was eluted in 30μL of nuclease free water.

RNA Extraction from cell populations from *in vivo* cell isolation was carried out with Arcturus™ PicoPure™ RNA Isolation kit according to the manufacturer's instructions. Cell pellets after centrifugation at 3000G for 10 minutes were resuspended in 50-100μL of Extraction buffer, according to cell number, and kept at -80°C prior to RNA extraction. RNA was eluted in 15-30μL of Elution Buffer according as well to cell number. In both cases, RNA was quantified using the NanoPhotometer N60 and stored at -80°C.

5.2.11.4. cDNA synthesis

RNA was used for retrotranscription into cDNA using the QuantiTect Reverse Transcription kit (Qiagen) according to the manufacturer´s instructions. Up to 1μg of RNA or maximum available normalized to the less concentrated samples was used. Resulting cDNA was further diluted in nuclease free water based on initial concentration and storage at -20°C.

5.2.11.5. Quantitative PCR

Gene expression analysis was performed by qPCR using the synthetized cDNA and the TaqMan system consisting of TaqMan Fast Advance Mastermix (Life Technologies), TaqMan probes (Applied Biosciences) and a StepOnePlus Real-Time PCR System (Thermo Fischer Scientific). Reaction was performed in duplicates or triplicates as indicated in Table 26. Reaction set up for qPCR. Gene expression was determined using the Ct values, averaged, normalized to the house keeping gene β-actin (ΔCt) and calculating the relative fold change ($2^{-\Delta Ct}$).

Table 26. Reaction set up for qPCR

qPCR reaction mix		qPCR Program		
	1 reaction	Step	Temperature	Time
cDNA	4 μL	1. Pre-denaturalization	95°C	30 sec
TaqMan Fast Advance Master Mix	5 μL	2. Denaturalization	95°C	2 sec
TaqMan Gene expression assay	0.5 μL	3. Amplification	60°C	20 sec
Nuclease-free H_2O	0.5 μL	Go to step 2: x40		

5.2.12. Statistical analysis

GraphPad Prism v6/v8 was used for statistical analysis and plotting. Data are represented as mean with error bars indicating standard deviation or standard error of the mean. Each point corresponds to one replicate for *in vitro* experiments and one mouse in the case of *in vivo*, unless otherwise indicated. Paired and unpaired two-tailed Student´s t-tests, and Log-rank Mantel Cox test were used for statistical analysis of two groups' comparison and survival analysis of a Kaplan-Meier representation, respectively. A p-value of less than 0.05 was considered significant as follows: *p<0.05, **p<0.01, ***p<0.001. Further details on statistical analysis can be found in each figure legend.

ABBREVIATIONS

2-AAF	2-acetylaminofluorene
ACK	Ammonium–chloride–potassium
AdDMEM	Advance Dulbecco's Modified Eagle Medium
AdSC	Adult derived stem/progenitor cells
AFP	α-fetoprotein
AIL	Air-liquid interface
AKT/PKB	RAC(Rho family)-alpha serine/threonine-protein kinase
Ang	Angiopoietin
APAP	Acetaminophen
APC	Adenomatosis polyposis coli
AST	Aspartate aminotransferase
Bax	BCL2 Associated X 2
BBB	Blood brain barriere
BCLC	Barcelona Clinic Liver Cancer
BME	Basement membrane extract
BMP	Bone morphogenetic protein
BSA	Bovine Serum Albumin
C/EBPα	CCAAT/enhancer binding protein-α
CAF	Cancer-associated fibroblasts
CaHSCs	Central vein-associated HSCs
CAMKII	Calmodulin-dependent kinase II
CCl_4	Carbon tetrachloride
CD13	Cluster differentiation 13
CD133	Cluster differentiation 133
CD24	Cluster differentiation 24
CD34	Cluster of Differentiation 34
CD44	Cluster differentiation 44
CD47	Cluster differentiation 47
CD90	Cluster differentiation 90
CDAAD	Choline-deficient l-amino acid-defined diet
CDC42	Cell division cycle 42
Cdh5	Cadherin-5
CDHFD	Choline-deficient high-fat diet
CDKN1A	Cyclin-dependent kinase inhibitor 1A
CK19	Cytokeratin 19
c-Kit	Tyrosine-protein kinase KIT/ CD117 (cluster of differentiation 117)
CKIα	Casein kinase Iα
CNS	Central nervous system
CO	Carbon monoxide
CO_2	Carbon dioxide
CRA	Cryoablation

CRC	Colorectal cancer
CRISPR	Clustered Regularly Interspaced Short Palindromic Repeats
CSC	Cancer stem cells
CTLA4	Cytotoxic T-lymphocyte associated protein 4
DAG	Diacylglycerol
DEN	Diethylnitrosamine
DKK1	Dickopf-related protein 1
DMEM	Dulbecco's Modified Eagle Medium
DMSO	Dimethyl sulfoxide
DNA	Deoxyribonucleic acid
Dvl	Disheveled
ECGS	Endothelial cell growth supplement
ECKO	Endothelial knockout
ECM	Extracellular matrix
ECs	Endothelial cells
EDTA	Ethylenediaminetetraacetic acid
EGF	Epidermal growth factor
EGFR	Epidermal Growth Factor Receptor
EPC	Endothelial progenitor cells
EpCAM	Epithelial cell adhesion molecule
ERG	ETS-related gene
ERK	Extracellular signal-regulated kinase
ERT2	Estrogen Receptor T2
Evi/Wls	Wnt Ligand Secretion Mediator
FACS	Fluorescence-activated cell sorting
FCS/FBS	Fetal calf/bovine serum
FGF	Fibroblasts growth factor
fl.	Floxed
FLC	Fibrolamelar carcinoma
FLT	Fms Related Receptor Tyrosine Kinase
G	Gauge
G (=RCF)	Relative centrifugal force
GEM(M)	Genetically engineered mouse models
Gpr124	G- protein couple receptor 124
GSK3	glycogen synthase kinase 3
h	hours
HBV	Hepatitis B virus
HCC	Hepatocellular carcinoma
HCV	Hepatitis C virus
HEPES	4-(2-hydroxyethyl)-1-piperazineethanesulfonic acid
HFD	High-fat diet
HFHCD	High-fat high-cholesterol diet
HFHFD	High-fat high-fructose diet
HGDNs	High-grade dysplastic nodules
HGF	Hepatocyte growth factor

HHEX	Hepatic specification factor haematopoietically expressed homeobox
HNF-1β	Hepatocyte nuclear factor 1 β
HNF4α	Hepatocyte nuclear factor 4 α
HNF-6	Hepatocyte nuclear factor 6
HSCs	Hepatic stellate cells
HSPGs	Heparan sulfate proteoglycans
HTVI	Hydrodynamic tail vein injection
HUVEC	Human umbilical vein endothelial cells
i.p.	Intraperitoneal
iAST	Inducible albumin SV40 T-antigen transgenic mice
ICAM1	Intercellular Adhesion Molecule 1
ICC	Intrahepatic cholangiocarcinoma
ICIs	Immune checkpoint inhibitors
iECKO	Inducible endothelial knockout
IELs	Intraepithelial lymphocytes
InsP3	Inositol-1,4,5-trisphosphate
iPSC	Induced pluripotent stem cells
ISH	*In situ* hybridization
IVIS	*In vivo* imaging system
JNK	JUN-N-terminal kinase
JUN	Jun proto-oncogene
kDa	Kilo daltons
KLF2	Transcription factor Kruppel-like factor 2
KO	knockout
LEF	Lymphoid enhancer factor
LGDNs	Low-grade dysplastic nodules
LGRs	Leu-rich repeat-containing G protein-coupled receptors
LRP5-6	Low density lipoprotein receptor-related protein 5-6
LSECs	Liver sinusoidal endothelial cells
MCD	Methionine and choline-deficient diet
MEK	Mitogen-activated protein kinase kinase
MET	Mesenchymal-epithelial transition factor
min	minutes
mM	Milimolar
MRI	Magnetic resonance imaging
MSCs	Mesenchymal stem cells
msec	Miliseconds
mTORC1	mechanistic/mammalian target of rapamycin complex 1
MUSK	Muscle skeletal receptor Tyr kinase
MWA	Microwave ablation
myc	Myelocytomatosis oncogene
NAFLD	Non-alcoholic fatty liver diseases
NASH	Nonalcoholic steatohepatitis
NFAT	Nuclear factor of activated T cells
ng	Nanogram

NGS	Normal Goat Serum
NK	Natural killer
NO	Nitric oxide
NPC	Non-parenchymal cells
ns	Non-significant
NSCLC	Non-small cell lung cancer
O.C.T./OCT	Optimal Cutting Temperature
Olig2	Oligodendrocyte transcription factor 2
OV6	Oval Cell marker
PaHSCs	Portal vein-associated HSCs
PB	Phenobarbital
PBS	Phosphate-buffered saline
PCP	Planar cell polarity
PCR	Polymerase Chain Reaction
PD1	Program cell death protein 1
PDGFR	Platelet Derived Growth Factor Receptor
PD-L1	Programmed death-ligand 1
PDO	Patient derived organoids
PDX	Patient derived xenografts
PFA	Paraformaldehyde
PIP2	Phosphatidylinositol-4,5-bisphosphate
PKC	Protein kinase C
PLC	Phospholipase C
PLV	Primary liver cancer
pTen	Phosphatase and tensin homolog
PTK2	Protein tyrosine kinase 2
PTK7	Protein Tyr kinase 7
qPCR	Quantitative olymerase Chain Reaction
RAC1	Ras-related C3 botulinum toxin substrate 1
Raf	Rapidly accelerated fibrosarcoma
Ras	Rat sarcoma virus
RBMY	RNA Binding Motif Protein Y-Linked
RBMY	RNA-binding motif gene on Y
RET	Ret Proto-Oncogene
RFA	Radiofrequency ablation
RHOA	Ras Homolog Family Member A
RNA	Ribonucleic acid
RNF43	Ring finger protein 43
ROCK	RHO kinase
ROR	Receptor Tyr kinase-like orphan receptor
Rspo	R-spondin
RT	Reverse transcription
RT	Room temperature
RYK	Receptor Tyr kinase
s.d.	Standard deviation

s.e.m.	Standard error of the mean
SB	Sleeping beauty
sec	seconds
sFRP	secreted Frizzled-related protein
Stat2	Signal Transducer And Activator Of Transcription
STZ	Streptozotocin
T	Tesla
TAA	Thioacetamide
TACE	Transarterial chemoembolization
TANs	Tumor associated neutrophils
TC	Tumor cells
TCF	T-cell factor
TEC	Tumor endothelial cells
TGFβ	Transforming growth factor beta
Tie2/TEK	Endothelial Tyrosine Kinase
TLR-2	Toll-like receptor 2
TME	Tumor microenvironment
V	Voltage
VEGF	Vascular endothelial growth factor
vWF	von Willebrand factor
WD	Western diet
WIF	WNT inhibitory factor
Wnt	Wingless-related integration site
Wt	Wild type
YAP/TAZ	Yes-associated protein/ transcriptional coactivator with PDZ-binding motif
ZNRF3	Zinc and ring finger 3
α2δ1	Voltage-dependent calcium channel subunit alpha-2/delta-1
β-TrCP	β transducin repeats-containing proteins
μg	Microgram
μL	microliters
μm	Micrometer
μM	Micromolar

REFERENCES

1. Ben-Moshe S, Itzkovitz S. Spatial heterogeneity in the mammalian liver. Nat Rev Gastroenterol Hepatol. 2019;16(7):395-410.

2. Trefts E, Gannon M, Wasserman DH. The liver. Curr Biol. 2017;27(21):R1147-R51.

3. Rhyu J, Yu R. Newly discovered endocrine functions of the liver. World J Hepatol. 2021;13(11):1611-1628.

4. Weiler-Normann C, Rehermann B. The liver as an immunological organ. J. Gastroenterol. Hepatol. 2004;19(7):279-83.

5. Gebhardt R. Metabolic zonation of the liver: regulation and implications for liver function. Pharmacol Ther. 1992;53(3):275-354.

6. Augustin HG, Koh GY. Organotypic vasculature: From descriptive heterogeneity to functional pathophysiology. Science. 2017;357(6353).

7. Kawada N, Tran-Thi TA, Klein H, Decker K. The contraction of hepatic stellate (Ito) cells stimulated with vasoactive substances. Possible involvement of endothelin 1 and nitric oxide in the regulation of the sinusoidal tonus. Eur J Biochem. 1993;213(2):815-23.

8. Koch PS, Lee KH, Goerdt S, Augustin HG. Angiodiversity and organotypic functions of sinusoidal endothelial cells. Angiogenesis. 2021;24(2):289-310.

9. Poisson J, Lemoinne S, Boulanger C, Durand F, Moreau R, Valla D, et al. Liver sinusoidal endothelial cells: Physiology and role in liver diseases. J Hepatol. 2017;66(1):212-27.

10. Lorenz L, Axnick J, Buschmann T, Henning C, Urner S, Fang S, et al. Mechanosensing by beta1 integrin induces angiocrine signals for liver growth and survival. Nature. 2018;562(7725):128-32.

11. Jackel S, Kiouptsi K, Lillich M, Hendrikx T, Khandagale A, Kollar B, et al. Gut microbiota regulate hepatic von Willebrand factor synthesis and arterial thrombus formation via Toll-like receptor-2. Blood. 2017;130(4):542-53.

12. Guidotti LG, Inverso D, Sironi L, Di Lucia P, Fioravanti J, Ganzer L, et al. Immunosurveillance of the liver by intravascular effector CD8(+) T cells. Cell. 2015;161(3):486-500.

13. Hu J, Srivastava K, Wieland M, et al. Endothelial cell-derived angiopoietin-2 controls liver regeneration as a spatiotemporal rheostat. Science. 2014;343(6169):416-419.

14. Kater JM. Comparative and experimental studies on the cytology of the liver.1933;15:217-246.

15. Hildebrandt F, Andersson A, Saarenpaa S, Larsson L, Van Hul N, Kanatani S, et al. Spatial transcriptomics to define transcriptional patterns of zonation and structural components in the mouse liver. Nat Commun. 2021;12(1):7046.

16. Halpern KB, Shenhav R, Matcovitch-Natan O, Toth B, Lemze D, Golan M, et al. Single-cell spatial reconstruction reveals global division of labour in the mammalian liver. Nature. 2017;542(7641):352-6.

17. Ben-Moshe S, Shapira Y, Moor AE, Manco R, Veg T, Bahar Halpern K, et al. Spatial sorting enables comprehensive characterization of liver zonation. Nat Metab. 2019;1(9):899-911.

18. Xie G, Wang L, Wang X, Wang L, DeLeve LD. Isolation of periportal, midlobular, and centrilobular rat liver sinusoidal endothelial cells enables study of zonated drug toxicity. Am J Physiol Gastrointest Liver Physiol. 2010;299(5):1204-10.

19. Halpern KB, Shenhav R, Massalha H, Toth B, Egozi A, Massasa EE, et al. Paired-cell sequencing enables spatial gene expression mapping of liver endothelial cells. Nat Biotechnol. 2018;36(10):962-70.

20. Ma R, Martinez-Ramirez AS, Borders TL, Gao F, Sosa-Pineda B. Metabolic and non-metabolic liver zonation is established non-synchronously and requires sinusoidal Wnts. Elife. 2020;9: 46026-29.

21. Preziosi M, Okabe H, Poddar M, Singh S, Monga SP. Endothelial Wnts regulate beta-catenin signaling in murine liver zonation and regeneration: A sequel to the Wnt-Wnt situation. Hepatol Commun. 2018;2(7):845-60.

22. Rocha AS, Vidal V, Mertz M, Kendall TJ, Charlet A, Okamoto H, et al. The angiocrine factor Rspondin3 is a key determinant of liver zonation. Cell Rep. 2015;13(9):1757-64.

23. Gola A, Dorrington MG, Speranza E, Sala C, Shih RM, Radtke AJ, et al. Commensal-driven immune zonation of the liver promotes host defence. Nature. 2021;589(7840):131-6.

24. Wang B, Zhao L, Fish M, Logan CY, Nusse R. Self-renewing diploid Axin2(+) cells fuel homeostatic renewal of the liver. Nature. 2015;524(7564):180-5.

25. He L, Pu W, Liu X, Zhang Z, Han M, Li Y, et al. Proliferation tracing reveals regional hepatocyte generation in liver homeostasis and repair. Science. 2021;371(6532).

26. Wei Y, Wang YG, Jia Y, Li L, Yoon J, Zhang S, et al. Liver homeostasis is maintained by midlobular zone 2 hepatocytes. Science. 2021;371(6532).

27. Ben-Moshe S, Veg T, Manco R, Dan S, Papinutti D, Lifshitz A, et al. The spatiotemporal program of zonal liver regeneration following acute injury. Cell Stem Cell. 2022;29(6):973-89.

28. Dobie R, Wilson-Kanamori JR, Henderson BEP, Smith JR, Matchett KP, Portman JR, et al. Single-cell transcriptomics uncovers zonation of function in the mesenchyme during liver fibrosis. Cell Rep. 2019;29(7):1832-47.

29. Yang W, He H, Wang T, Su N, Zhang F, Jiang K, et al. Single-cell transcriptomic analysis reveals a hepatic stellate cell-activation roadmap and myofibroblast origin during liver fibrosis in mice. Hepatology. 2021;74(5):2774-90.

30. Aizarani N, Saviano A, Sagar, Mailly L, Durand S, Herman JS, et al. A human liver cell atlas reveals heterogeneity and epithelial progenitors. Nature. 2019;572(7768):199-204.

31. Llovet JM, Kelley RK, Villanueva A, Singal AG, Pikarsky E, Roayaie S, et al. Hepatocellular carcinoma. Nat Rev Dis Primers. 2021;7(1):6.

32. Llovet JM, Zucman-Rossi J, Pikarsky E, Sangro B, Schwartz M, Sherman M, et al. Hepatocellular carcinoma. Nat Rev Dis Primers. 2016;2:16018.

33. Villanueva A. Hepatocellular Carcinoma. N Engl J Med. 2019;380(15):1450-62.

34. Wang G, Wang Q, Liang N, Xue H, Yang T, Chen X, et al. Oncogenic driver genes and tumor microenvironment determine the type of liver cancer. Cell Death Dis. 2020;11(5):313.

35. Anstee QM, Reeves HL, Kotsiliti E, Govaere O, Heikenwalder M. From NASH to HCC: current concepts and future challenges. Nat Rev Gastroenterol Hepatol. 2019;16(7):411-28.

36. Barthet VJA, Brucoli M, Ladds MJGW, et al. Autophagy suppresses the formation of hepatocyte-derived cancer-initiating ductular progenitor cells in the liver. Sci Adv. 2021;7(23): 9141-57.

37. Adebayo Michael AO, Ko S, Tao J, Moghe A, Yang H, Xu M, et al. Inhibiting glutamine-dependent mTORC1 activation ameliorates liver cancers driven by beta-catenin mutations. Cell Metab. 2019;29(5):1135-50.

38. Fan Z, Duan J, Wang L, Xiao S, Li L, Yan X, et al. PTK2 promotes cancer stem cell traits in hepatocellular carcinoma by activating Wnt/beta-catenin signaling. Cancer Lett. 2019;450:132-43.

39. Becker AK, Tso DK, Harris AC, Malfair D, Chang SD. Extrahepatic metastases of hepatocellular carcinoma: A spectrum of imaging findings. Can Assoc Radiol J. 2014;65(1):60-6.

40. Wolf MJ, Adili A, Piotrowitz K, Abdullah Z, Boege Y, Stemmer K, et al. Metabolic activation of intrahepatic CD8+ T cells and NKT cells causes nonalcoholic steatohepatitis and liver cancer via cross-talk with hepatocytes. Cancer Cell. 2014;26(4):549-64.

41. Liu Q, Li J, Zhang W, Xiao C, Zhang S, Nian C, et al. Glycogen accumulation and phase separation drives liver tumor initiation. Cell. 2021;184(22):5559-76.

42. Lee TK-W, Guan X-Y, Ma S. Cancer stem cells in hepatocellular carcinoma — from origin to clinical implications. Nat Rev Gastroenterol Hepatol. 2021;19(1):26-44.

43. Franco CA, Liebner S, Gerhardt H. Vascular morphogenesis: a Wnt for every vessel? Curr Opin Genet Dev. 2009;19(5):476-83.

44. Potente M, Gerhardt H, Carmeliet P. Basic and therapeutic aspects of angiogenesis. Cell. 2011;146(6):873-87.

45. Semela D, Dufour JF. Angiogenesis and hepatocellular carcinoma. J Hepatol. 2004;41(5):864-80.

46. Butler JM, Kobayashi H, Rafii S. Instructive role of the vascular niche in promoting tumour growth and tissue repair by angiocrine factors. Nat Rev Cancer. 2010;10(2):138-46.

47. Augustin HG, Koh GY. Antiangiogenesis: Vessel Regression, vessel Normalization, or both? Cancer Res. 2022;82(1):15-7.

48. Zhu YJ, Zheng B, Wang HY, Chen L. New knowledge of the mechanisms of sorafenib resistance in liver cancer. Acta Pharmacol Sin. 2017;38(5):614-22.

49. Llovet JM, Pinyol R, Kelley RK, El-Khoueiry A, Reeves HL, Wang XW, et al. Molecular pathogenesis and systemic therapies for hepatocellular carcinoma. Nat Cancer. 2022;3(4):386-401.

50. Jain RK. Normalization of tumor vasculature: an emerging concept in antiangiogenic therapy. Science. 2005;307(5706):58-62.

51. Yang C, Zhang H, Zhang L, Zhu AX, Bernards R, Qin W, et al. Evolving therapeutic landscape of advanced hepatocellular carcinoma. Nat Rev Gastroenterol Hepatol. 2023;20(4):203-22.

52. Finn RS, Qin S, Ikeda M, Galle PR, Ducreux M, Kim TY, et al. Atezolizumab plus Bevacizumab in unresectable Hepatocellular Carcinoma. N Engl J Med. 2020;382(20):1894-905.

53. Salem R, Li D, Sommer N, Hernandez S, Verret W, Ding B, et al. Characterization of response to Atezolizumab + Bevacizumab versus Sorafenib for Hepatocellular Carcinoma: Results from the IMbrave150 trial. Cancer Medicine. 2021;10(16):5437-47.

54. Zhu AX, Abbas AR, de Galarreta MR, Guan Y, Lu S, Koeppen H, et al. Molecular correlates of clinical response and resistance to Atezolizumab in combination with Bevacizumab in advanced Hepatocellular Carcinoma. Nat Med. 2022;28(8):1599-611.

55. Qin S, Chen M, Cheng AL, Kaseb AO, Kudo M, Lee HC, et al. Atezolizumab plus Bevacizumab versus active surveillance in patients with resected or ablated high-risk Hepatocellular Carcinoma (IMbrave050): a randomised, open-label, multicentre, phase 3 trial. Lancet. 2023;402(10415):1835-47.

56. Torrens L, Montironi C, Puigvehí M, Mesropian A, Leslie J, Haber PK, et al. Immunomodulatory effects of Lenvatinib plus anti–Programmed Cell Death Protein 1 in mice and rationale for patient enrichment in Hepatocellular Carcinoma. Hepatology. 2021;74(5):2652-69.

57. Yi C, Chen L, Lin Z, Liu L, Shao W, Zhang R, et al. Lenvatinib targets FGF Receptor 4 to enhance antitumor immune response of anti-programmed cell death-1 in HCC. Hepatology. 2021;74(5):2544-60.

58. Ho WJ, Zhu Q, Durham J, Popovic A, Xavier S, Leatherman J, et al. Neoadjuvant Cabozantinib and Nivolumab converts locally advanced HCC into resectable disease with enhanced antitumor immunity. Nat Cancer. 2021;2(9):891-903.

59. Jin H, Shi Y, Lv Y, Yuan S, Ramirez CFA, Lieftink C, et al. EGFR activation limits the response of liver cancer to Lenvatinib. Nature. 2021;595(7869):730-4.

60. Sachs N, Clevers H. Organoid cultures for the analysis of cancer phenotypes. Curr Opin Genet Dev. 2014;24:68-73.

61. Darlington GJ, Bernhard HP, Miller RA, Ruddle FH. Expression of liver phenotypes in cultured mouse hepatoma cells. J Natl Cancer Inst. 1980;64(4):809-819.

62. Yu K, Chen B, Aran D, Charalel J, Yau C, Wolf DM, et al. Comprehensive transcriptomic analysis of cell lines as models of primary tumors across 22 tumor types. Nat Commun. 2019;10(1):3574.

63. Huch M, Koo BK. Modeling mouse and human development using organoid cultures. Development. 2015;142(18):3113-25.

64. Hindley CJ, Cordero-Espinoza L, Huch M. Organoids from adult liver and pancreas: Stem cell biology and biomedical utility. Dev Biol. 2016;420(2):251-61.

65. Sato T, Vries RG, Snippert HJ, van de Wetering M, Barker N, Stange DE, et al. Single Lgr5 stem cells build crypt-villus structures in vitro without a mesenchymal niche. Nature. 2009;459(7244):262-5.

66. Kretzschmar K, Clevers H. Organoids: Modeling development and the stem cell niche in a dish. Dev Cell. 2016;38(6):590-600.

67. Wimmer RA, Leopoldi A, Aichinger M, Wick N, Hantusch B, Novatchkova M, et al. Human blood vessel organoids as a model of diabetic vasculopathy. Nature. 2019;565(7740):505-10.

68. Huch M, Dorrell C, Boj SF, van Es JH, Li VS, van de Wetering M, et al. In vitro expansion of single Lgr5+ liver stem cells induced by Wnt-driven regeneration. Nature. 2013;494(7436):247-50.

69. Broutier L, Andersson-Rolf A, Hindley CJ, Boj SF, Clevers H, Koo BK, et al. Culture and establishment of self-renewing human and mouse adult liver and pancreas 3D organoids and their genetic manipulation. Nat Protoc. 2016;11(9):1724-43.

70. Hu H, Gehart H, Artegiani B, C LO-I, Dekkers F, Basak O, et al. Long-term expansion of functional mouse and human hepatocytes as 3D organoids. Cell. 2018;175(6):1591-606.

71. Tang XY, Wu S, Wang D, Chu C, Hong Y, Tao M, et al. Human organoids in basic research and clinical applications. Signal Transduct Target Ther. 2022;7(1):168.

72. van de Wetering M, Francies HE, Francis JM, Bounova G, Iorio F, Pronk A, et al. Prospective derivation of a living organoid biobank of colorectal cancer patients. Cell. 2015;161(4):933-45.

73. Vlachogiannis G, Hedayat S, Vatsiou A, et al. Patient-derived organoids model treatment response of metastatic gastrointestinal cancers. Science. 2018;359(6378):920-926.

74. Jalan-Sakrikar N, Brevini T, Huebert RC, Sampaziotis F. Organoids and regenerative hepatology. Hepatology. 2023;77(1):305-22.

75. Nuciforo S, Fofana I, Matter MS, Blumer T, Calabrese D, Boldanova T, et al. Organoid models of human liver cancers derived from tumor needle biopsies. Cell Rep. 2018;24(5):1363-76.

76. Cao W, Liu J, Wang L, Li M, Verstegen MMA, Yin Y, et al. Modeling liver cancer and therapy responsiveness using organoids derived from primary mouse liver tumors. Carcinogenesis. 2019;40(1):145-54.

77. Broutier L, Mastrogiovanni G, Verstegen MM, Francies HE, Gavarro LM, Bradshaw CR, et al. Human primary liver cancer-derived organoid cultures for disease modeling and drug screening. Nat Med. 2017;23(12):1424-35.

78. Cordero-Espinoza L, Dowbaj AM, Kohler TN, Strauss B, Sarlidou O, Belenguer G, et al. Dynamic cell contacts between periportal mesenchyme and ductal epithelium act as a rheostat for liver cell proliferation. Cell Stem Cell. 2021;28(11):1907-21.

79. Wang Y, Takeishi K, Li Z, Cervantes-Alvarez E, Collin de l'Hortet A, Guzman-Lepe J, et al. Microenvironment of a tumor-organoid system enhances hepatocellular carcinoma malignancy-related hallmarks. Organogenesis. 2017;13(3):83-94.

80. Nozaki K, Mochizuki W, Matsumoto Y, Matsumoto T, Fukuda M, Mizutani T, et al. Co-culture with intestinal epithelial organoids allows efficient expansion and motility analysis of intraepithelial lymphocytes. J Gastroenterol. 2016;51(3):206-13.

81. Dijkstra KK, Cattaneo CM, Weeber F, Chalabi M, van de Haar J, Fanchi LF, et al. Generation of tumor-reactive T Cells by co-culture of peripheral blood lymphocytes and tumor organoids. Cell. 2018;174(6):1586-98.

82. Takebe T, Enomura M, Yoshizawa E, Kimura M, Koike H, Ueno Y, et al. Vascularized and complex organ buds from diverse tissues via mesenchymal cell-driven condensation. Cell Stem Cell. 2015;16(5):556-65.

83. Takebe T, Sekine K, Enomura M, Koike H, Kimura M, Ogaeri T, et al. Vascularized and functional human liver from an iPSC-derived organ bud transplant. Nature. 2013;499(7459):481-4.

84. Neal JT, Li X, Zhu J, Giangarra V, Grzeskowiak CL, Ju J, et al. Organoid modeling of the tumor immune microenvironment. Cell. 2018;175(7):1972-88.

85. Gu CY, Lee TKW. Preclinical mouse models of hepatocellular carcinoma: An overview and update. Exp Cell Res. 2022;412(2):113042.

86. Liu S, Huang F, Ru G, Wang Y, Zhang B, Chen X, et al. Mouse models of Hepatocellular Carcinoma: Classification, advancement, and application. Front Oncol. 2022;12:902820.

87. Zheng HC, Xue H, Yun WJ. An overview of mouse models of hepatocellular carcinoma. Infect Agent Cancer. 2023;18(1):49.

88. Runge A, Hu J, Wieland M, Bergeest JP, Mogler C, Neumann A, et al. An inducible hepatocellular carcinoma model for preclinical evaluation of antiangiogenic therapy in adult mice. Cancer Res. 2014;74(15):4157-69.

89. Vilchez V, Turcios L, Marti F, Gedaly R. Targeting Wnt/beta-catenin pathway in hepatocellular carcinoma treatment. World J Gastroenterol. 2016;22(2):823-32.

90. Niehrs C. The complex world of WNT receptor signalling. Nat Rev Mol Cell Biol. 2012;13(12):767-79.

91. Nusse R, Clevers H. Wnt/beta-catenin signaling, disease, and emerging therapeutic modalities. Cell. 2017;169(6):985-99.

92. Eubelen M, Bostaille N, Cabochette P, Gauquier A, Tebabi P, Dumitru AC, et al. A molecular mechanism for Wnt ligand-specific signaling. Science. 2018;361(6403).

93. Lebensohn AM, Rohatgi R. R-spondins can potentiate WNT signaling without LGRs. Elife. 2018;7.

94. Dejana E. The role of wnt signaling in physiological and pathological angiogenesis. Circ Res. 2010;107(8):943-52.

95. Perugorria MJ, Olaizola P, Labiano I, Esparza-Baquer A, Marzioni M, Marin JJG, et al. Wnt-beta-catenin signalling in liver development, health and disease. Nat Rev Gastroenterol Hepatol. 2019;16(2):121-36.

96. Ferguson JE, 3rd, Kelley RW, Patterson C. Mechanisms of endothelial differentiation in embryonic vasculogenesis. Arterioscler Thromb Vasc Biol. 2005;25(11):2246-54.

97. Yang DH, Yoon JY, Lee SH, Bryja V, Andersson ER, Arenas E, et al. Wnt5a is required for endothelial differentiation of embryonic stem cells and vascularization via pathways involving both Wnt/beta-catenin and protein kinase Calpha. Circ Res. 2009;104(3):372-9.

98. Wang H, Charles PC, Wu Y, Ren R, Pi X, Moser M, et al. Gene expression profile signatures indicate a role for Wnt signaling in endothelial commitment from embryonic stem cells. Circ Res. 2006;98(10):1331-9.

99. Wang H, Gilner JB, Bautch VL, Wang D-Z, Wainwright BJ, Kirby SL, et al. Wnt2 coordinates the commitment of mesoderm to hematopoietic, endothelial, and cardiac lineages in embryoid bodies. J Biol Chem. 2007;282(1):782-91.

100. Kazanskaya O, Ohkawara B, Heroult M, Wu W, Maltry N, Augustin HG, et al. The Wnt signaling regulator R-spondin 3 promotes angioblast and vascular development. Development. 2008;135(22):3655-64.

101. Kim KA, Zhao J, Andarmani S, Kakitani M, Oshima T, Binnerts ME, et al. R-Spondin proteins: a novel link to beta-catenin activation. Cell Cycle. 2006;5(1):23-6.

102. Scholz B, Korn C, Wojtarowicz J, Mogler C, Augustin I, Boutros M, et al. Endothelial RSPO3 controls vascular stability and pruning through non-canonical WNT/Ca(2+)/NFAT signaling. Dev Cell. 2016;36(1):79-93.

103. Masckauchan TN, Agalliu D, Vorontchikhina M, Ahn A, Parmalee NL, Li CM, et al. Wnt5a signaling induces proliferation and survival of endothelial cells in vitro and expression of MMP-1 and Tie-2. Mol Biol Cell. 2006;17(12):5163-72.

104. Cheng CW, Yeh JC, Fan TP, Smith SK, Charnock-Jones DS. Wnt5a-mediated non-canonical Wnt signalling regulates human endothelial cell proliferation and migration. Biochem Biophys Res Commun. 2008;365(2):285-90.

105. Nayak G, Odaka Y, Prasad V, Solano AF, Yeo EJ, Vemaraju S, et al. Developmental vascular regression is regulated by a Wnt/beta-catenin, MYC and CDKN1A pathway that controls cell proliferation and cell death. Development. 2018;145(12).

106. Birdsey GM, Shah AV, Dufton N, Reynolds LE, Osuna Almagro L, Yang Y, et al. The endothelial transcription factor ERG promotes vascular stability and growth through Wnt/beta-catenin signaling. Dev Cell. 2015;32(1):82-96.

107. Descamps B, Sewduth R, Ferreira Tojais N, Jaspard B, Reynaud A, Sohet F, et al. Frizzled 4 regulates arterial network organization through noncanonical Wnt/planar cell polarity signaling. Circ Res. 2012;110(1):47-58.

108. Franco CA, Jones ML, Bernabeu MO, Vion AC, Barbacena P, Fan J, et al. Non-canonical Wnt signalling modulates the endothelial shear stress flow sensor in vascular remodelling. Elife. 2016;5:e07727.

109. Hanahan D, Weinberg RA. The hallmarks of cancer. Cell. 2000;100(1):57-70.

110. Hanahan D. Hallmarks of Cancer: New Dimensions. Cancer Discov. 2022;12(1):31-46.

111. Hanahan D, Weinberg RA. Hallmarks of cancer: the next generation. Cell. 2011;144(5):646-74.

112. Zhong Z, Yu J, Virshup DM, Madan B. Wnts and the hallmarks of cancer. Cancer Metastasis Rev. 2020;39(3):625-45.

113. Korn C, Scholz B, Hu J, Srivastava K, Wojtarowicz J, Arnsperger T, et al. Endothelial cell-derived non-canonical Wnt ligands control vascular pruning in angiogenesis. Development. 2014;141(8):1757-66.

114. Martin M, Vermeiren S, Bostaille N, Eubelen M, Spitzer D, Vermeersch M, et al. Engineered Wnt ligands enable blood-brain barrier repair in neurological disorders. Science. 2022;375(6582):737-49.

115. Griveau A, Seano G, Shelton SJ, Kupp R, Jahangiri A, Obernier K, et al. A glial signature and Wnt7 signaling regulate glioma-vascular interactions and tumor microenvironment. Cancer Cell. 2018;33(5):874-89.

116. Yue Z, Niu X, Yuan Z, Qin Q, Jiang W, He L, et al. RSPO2 and RANKL signal through LGR4 to regulate osteoclastic premetastatic niche formation and bone metastasis. J Clin Invest. 2022;132(2).

117. Takeuchi Y, Tanegashima T, Sato E, et al. Highly immunogenic cancer cells require activation of the WNT pathway for immunological escape. Sci Immunol. 2021;6(65):eabc6424.

118. Tang Y, Xu Q, Hu L, Yan X, Feng X, Yokota A, et al. Tumor microenvironment-derived R-spondins enhance antitumor immunity to suppress tumor growth and sensitize for immune checkpoint blockade therapy. Cancer Discov. 2021;11(12):3142-57.

119. Zimmerli D, Cecconi V, Valenta T, Hausmann G, Cantu C, Restivo G, et al. WNT ligands control initiation and progression of human papillomavirus-driven squamous cell carcinoma. Oncogene. 2018;37(27):3753-62.

120. Chen Z, Zhang J, Yuan A, Han J, Tan L, Zhou Z, et al. R-spondin3 promotes the tumor growth of choriocarcinoma JEG-3 cells. Am J Physiol Cell Physiol. 2020;318(3):664-74.

121. Tammela T, Sanchez-Rivera FJ, Cetinbas NM, Wu K, Joshi NS, Helenius K, et al. A Wnt-producing niche drives proliferative potential and progression in lung adenocarcinoma. Nature. 2017;545(7654):355-9.

122. Vermeulen L, De Sousa EMF, van der Heijden M, Cameron K, de Jong JH, Borovski T, et al. Wnt activity defines colon cancer stem cells and is regulated by the microenvironment. Nat Cell Biol. 2010;12(5):468-76.

123. Huels DJ, Bruens L, Hodder MC, Cammareri P, Campbell AD, Ridgway RA, et al. Wnt ligands influence tumour initiation by controlling the number of intestinal stem cells. Nat Commun. 2018;9(1):1132.

124. Lähde M, Heino S, Högström J, et al. Expression of R-Spondin 1 in ApcMin/+ mice suppresses growth of intestinal adenomas by altering Wnt and transforming growth factor beta signaling. Gastroenterology. 2021;160(1):245-259.

125. Xu C, Xu Z, Zhang Y, Evert M, Calvisi DF, Chen X. Beta-catenin signaling in Hepatocellular Carcinoma. J Clin Invest. 2022;132(4).

126. Zhao H, Ming T, Tang S, Ren S, Yang H, Liu M, et al. Wnt signaling in Colorectal Cancer: pathogenic role and therapeutic target. Mol Cancer. 2022;21(1):144.

127. Schneider MR, Hiltwein F, Grill J, Blum H, Krebs S, Klanner A, et al. Evidence for a role of E-cadherin in suppressing liver carcinogenesis in mice and men. Carcinogenesis. 2014;35(8):1855-62.

128. Yang, M., & Zhang, C. (2021). The role of liver sinusoidal endothelial cells in cancer liver metastasis. Am J Cancer Res, *11*(5), 1845–1860.

129. Gengenbacher N, Singhal M, Augustin HG. Preclinical mouse solid tumour models: status quo, challenges and perspectives. Nat Rev Cancer. 2017;17(12):751-65.

130. Makino Y, Hikita H, Fukumoto K, Sung JH, Sakano Y, Murai K, et al. Constitutive activation of the tumor suppressor p53 in hepatocytes paradoxically promotes non-cell autonomous liver carcinogenesis. Cancer Res. 2022;82(16):2860-73.

131. Zhu Y, Gu L, Lin X, Zhou X, Lu B, Liu C, et al. P53 deficiency affects cholesterol esterification to exacerbate hepatocarcinogenesis. Hepatology. 2023;77(5):1499-511.

132. Tsai JH, Jeng YM, Lee CH, Liau JY. Molecular features of primary hepatic undifferentiated carcinoma. Mod Pathol. 2022;35(5):680-7.

133. Inverso D, Shi J, Lee KH, Jakab M, Ben-Moshe S, Kulkarni SR, et al. A spatial vascular transcriptomic, proteomic, and phosphoproteomic atlas unveils an angiocrine Tie-Wnt signaling axis in the liver. Dev Cell. 2021;56(11):1677-93.

134. Kabiri Z, Greicius G, Madan B, Biechele S, Zhong Z, Zaribafzadeh H, et al. Stroma provides an intestinal stem cell niche in the absence of epithelial Wnts. Development. 2014;141(11):2206-15.

135. Fane ME, Chhabra Y, Alicea GM, Maranto DA, Douglass SM, Webster MR, et al. Stromal changes in the aged lung induce an emergence from melanoma dormancy. Nature. 2022;606(7913):396-405.

136. Jakab M, Lee KH, Uvarovskii A, Ovchinnikova S, Kulkarni SR, Jakab S, et al. Lung endothelium exploits susceptible tumor cell states to instruct metastatic latency. Nat Cancer. 2024.

137. Ilmer M, Boiles AR, Regel I, Yokoi K, Michalski CW, Wistuba, II, et al. RSPO2 enhances canonical Wnt signaling to confer stemness-associated traits to susceptible pancreatic cancer cells. Cancer Res. 2015;75(9):1883-96.

138. Belenguer G, Mastrogiovanni G, Pacini C, Hall Z, Dowbaj AM, Arnes-Benito R, et al. RNF43/ZNRF3 loss predisposes to Hepatocellular-Carcinoma by impairing liver regeneration and altering the liver lipid metabolic ground-state. Nat Commun. 2022;13(1):334.

139. Sun T, Annunziato S, Bergling S, Sheng C, Orsini V, Forcella P, et al. ZNRF3 and RNF43 cooperate to safeguard metabolic liver zonation and hepatocyte proliferation. Cell Stem Cell. 2021;28(10):1822-37.

140. Kim A, Wu X, Allende DS, Nagy LE. Gene deconvolution reveals aberrant liver regeneration and immune cell infiltration in alcohol-associated hepatitis. Hepatology. 2021;74(2):987-1002.

141. Chen F, Jimenez RJ, Sharma K, Luu HY, Hsu BY, Ravindranathan A, et al. Broad distribution of hepatocyte proliferation in liver homeostasis and regeneration. Cell Stem Cell. 2020;26(1):27-33.

142. Lin H, Huang Y-S, Fustin J-M, Doi M, Chen H, Lai H-H, et al. Hyperpolyploidization of hepatocyte initiates preneoplastic lesion formation in the liver. Nature Communications. 2021;12(1).

143. Dai W, Shen J, Yan J, Bott AJ, Maimouni S, Daguplo HQ, et al. Glutamine synthetase limits beta-catenin-mutated liver cancer growth by maintaining nitrogen homeostasis and suppressing mTORC1. J Clin Invest. 2022;132(24).

144. Zhao JS, Shi S, Qu HY, Keckesova Z, Cao ZJ, Yang LX, et al. Glutamine synthetase licenses APC/C-mediated mitotic progression to drive cell growth. Nat Metab. 2022;4(2):239-53.

145. Sharma A, Seow JJW, Dutertre CA, Pai R, Bleriot C, Mishra A, et al. Onco-fetal reprogramming of endothelial cells drives immunosuppressive macrophages in Hepatocellular Carcinoma. Cell. 2020;183(2):377-94.

146. Wohlfeil SA, Hafele V, Dietsch B, Schledzewski K, Winkler M, Zierow J, et al. Hepatic endothelial Notch activation protects against liver metastasis by regulating endothelial-tumor cell adhesion independent of angiocrine signaling. Cancer Res. 2019;79(3):598-610.

147. Filliol A, Saito Y, Nair A, Dapito DH, Yu LX, Ravichandra A, et al. Opposing roles of hepatic stellate cell subpopulations in hepatocarcinogenesis. Nature. 2022;610(7931):356-65.

148. Zhou SL, Yin D, Hu ZQ, Luo CB, Zhou ZJ, Xin HY, et al. A positive feedback loop between cancer stem-like cells and tumor-associated neutrophils controls Hepatocellular Carcinoma progression. Hepatology. 2019;70(4):1214-30.

149. Mah AT, Yan KS, Kuo CJ. Wnt pathway regulation of intestinal stem cells. J Physiol. 2016;594(17):4837-47.